



HAL
open science

Études des variations décennales de la température de la moyenne atmosphère

Robin Wing

► **To cite this version:**

Robin Wing. Études des variations décennales de la température de la moyenne atmosphère. Milieux et Changements globaux. Université Paris Saclay (COmUE), 2019. Français. NNT : 2019SACLV007 . tel-02111985

HAL Id: tel-02111985

<https://theses.hal.science/tel-02111985>

Submitted on 26 Apr 2019

HAL is a multi-disciplinary open access archive for the deposit and dissemination of scientific research documents, whether they are published or not. The documents may come from teaching and research institutions in France or abroad, or from public or private research centers.

L'archive ouverte pluridisciplinaire **HAL**, est destinée au dépôt et à la diffusion de documents scientifiques de niveau recherche, publiés ou non, émanant des établissements d'enseignement et de recherche français ou étrangers, des laboratoires publics ou privés.

Études des variations décennales de la température de la moyenne atmosphère

Thèse de doctorat de l'Université Paris-Saclay
préparée à l'Université de Versailles-Saint-Quentin-en-Yvelines

Ecole doctorale n°579 Sciences mécaniques et énergétiques, matériaux et géosciences (SMEMaG)
Spécialité de doctorat : météorologie, océanographie, physique de l'environnement

Thèse présentée et soutenue à Guyancourt, le 21 Février 2019, par

ROBIN WING

Composition du Jury :

Chantal Claud Directrice de recherche, Laboratoire de Météorologie Dynamique	Président
Nathalie Huret Professeur, OPGC / Université de Clermont-Ferrand	Rapporteur
Alexis Le Pichon Directeur de recherche, CEA-DAM, DASE	Rapporteur
Wolfgang Steinbrecht Professeur, Deutscher Wetterdienst	Examineur
Alain Hauchecorne Directeur de recherche, CNRS	Directeur de thèse
Philippe Keckhut Professeur, Université de Versailles Saint-Quentin-en-Yvelines	Co-directeur de thèse
Albert Hertzog Maître de conférences, Laboratoire de Météorologie Dynamique	Invité

Declaration of Authorship

I, Robin WING, declare that this thesis titled, “Études des variations décennales de la température de la moyenne atmosphère” and the work presented in it are my own. Where co-authorship exists I have specified my contributions to the article.

Signed:

Date:

Titre : Étude des variations décennales de la température de la moyenne atmosphère

Mots clés : température / lidar / télédétection / validation

Résumé :

L'atmosphère moyenne de la Terre est un laboratoire naturel pour les études de la dynamique géophysique des fluides et de l'optique pour la mesure des gaz. Les recherches dans cette région ont longtemps été limitées par le manque d'observations à long terme susceptibles de couvrir l'ensemble de la région, de la troposphère à la haute mésosphère et à la thermosphère inférieure. Les dernières décennies ont vu la construction de nombreux observatoires au sol et le lancement d'instruments par satellite dans le but de fournir les mesures nécessaires pour comprendre la chimie, la dynamique et les changements climatiques à long terme de l'atmosphère moyenne. La télédétection atmosphérique, tant au sol que dans l'espace, présente des avantages et des inconvénients évidents. Les premiers étant capables de fournir des mesures bien calibrées et à haute résolution sur un seul site et les derniers permettant une couverture globale au prix de la résolution et d'un certain degré de certitude lors de l'étalonnage. Pour ce travail, nous utilisons des mesures de température obtenues à l'aide d'une technique de télédétection au sol basée sur le lidar à diffusion de Rayleigh et nous effectuons des comparaisons systématiques avec les profils de température générés à l'aide de trois instruments de télédétection passif basés sur des satellites : Sondeur Micro-onde sur satellite Aura (MLS). Sondage de l'atmosphère par radiométrie des émissions à large bande (SABER) et surveillance mondiale de l'ozone par occultation d'étoiles (GOMOS).

Ce manuscrit a trois résultats principaux : 1a) Présentation de plusieurs améliorations de l'algorithme de la température lidar qui corrigent un biais chaud connu dans les températures lidar

mésosphériques. Nous réduisons ce biais jusqu'à 20 K à 90 km. 1b) Meilleur accord entre les températures du lidar et les profils de température SABER et MLS entre 70 km et 90 km. 1c) Une validation croisée entre les températures d'un lidar de température de Rayleigh et d'un lidar d'ozone co-localisés, qui donne confiance en la stabilité de la technique du lidar et justifie l'utilisation de la température par lidar comme base de données de référence pour la validation par satellite. 2a) Présentation d'une comparaison décennale entre les températures lidar validées et les températures produites par SABER et MLS. 2b) Nous montrons un biais froid dans les mesures satellitaires par rapport au lidar (-6 K pour SABER et -17 K pour MLS) dans la région de stratopause, un biais chaud (6 K près de 60 km) dans la mésosphère d'été, et un biais structuré verticalement pour MLS (-4 à 4 K) qui couvre la moyenne atmosphère. 2c) Nous réduisons l'ampleur du biais en décallant verticalement la hauteur de la stratopause satellite et constatons une amélioration de la comparaison de température lidar-satellite qui en résulte. Ce résultat a des implications importantes pour la notification des températures des satellites en fonction de la hauteur géopotentielle. 3a) La comparaison des profils de température lidar avec la nouvelle base de données de température GOMOS montre que les altitudes géométriques des satellites peuvent être mieux estimées par les techniques d'occultation que par l'inférence des niveaux de pression à partir des données radiométriques 3b) de l'effet des marées sur les comparaisons de température entre lidar et satellite lorsque le passage supérieur du satellite est décalé dans le temps par rapport à la mesure lidar et peut être de l'ordre de 2 à 4 K en fonction de la phase de l'heure solaire.

Title : Study of decadal variations in the temperature of the middle atmosphere

Keywords : temperature / lidar / remote sensing / validation

Abstract :

The Earth's middle atmosphere is a pristine natural laboratory for the study of geophysical fluid dynamics and optics in neutral gasses. Research in this region has long been limited by a lack of long-term observations which are capable of covering the entire region from the troposphere to the upper mesosphere and lower thermosphere. Past decades have seen the construction of many ground based observatories and launches of satellite based instruments in an effort to provide the measurements needed to understand the chemistry, dynamics, and long-term climatic changes in the middle atmosphere. Both ground-based and space-based atmospheric remote sensing have clear strengths as well as limitations; the former being able to provide high resolution, well calibrated measurements at a single site and the latter allowing for global coverage at the cost of resolution and some degree of certainty in calibration. For this work we are using temperature measurements produced from a Rayleigh-scatter lidar ground-based remote sensing technique and making systematic comparisons to temperature profiles produced from three passive scanning satellite-based remote sensing instruments: Microwave Limb Sounder on the Aura satellite (MLS), Sounding of the Atmosphere using Broadband Emission Radiometry (SABER), and Global Ozone Monitoring by Occultation of Stars (GOMOS).

This manuscript has three main results: 1a) Presentation of several improvements to the lidar temperature algorithm which address a known warm bias in mesospheric lidar temperatures. We reduce this bias

by up to 20 K at 90 km. 1b) Better agreement between the cooled lidar temperatures and temperature profiles from SABER and MLS between 70 km and 90 km. 1c) A cross-validation between temperatures from a co-located Rayleigh temperature lidar and ozone lidar which provides confidence in the stability of the lidar technique and justification for the use of lidar temperatures as a reference database for satellite validation. 2a) Presentation of a decadal comparison between the validated lidar temperatures and the temperatures produced by SABER and MLS. 2b) We show a cold bias in the satellite measurements with respect to the lidar (-6 K for SABER and -17 K for MLS) in the stratopause region, a warm bias (6 K near 60 km) in the summer mesosphere, and a vertically structured bias for MLS (-4 to 4 K) which spans the middle atmosphere. 2c) We reduce the magnitude of the bias by vertically shifting the height of the satellite stratopause and see an improvement in the resulting lidar-satellite temperature comparison. This result has important implications for the reporting of satellite temperatures as a function of geopotential height. 3a) Comparison of lidar temperature profiles with the newly created GOMOS temperature data base shows that satellite geometric altitudes can be better estimated by occultation techniques than by inference of pressure levels from radiometric data 3b) The effect of tides on lidar to satellite temperature comparisons when the satellite overpass is temporally offset from the lidar measurement can be on the order of 2 to 4 K depending on the phase of the solar hour.



For Frances Poleschuk, my first
and most influential teacher

Acknowledgements

I would like to thank my thesis co-directors for their support, encouragement, and patience. They have allowed me the time and freedom to pursue difficult scientific questions and develop my skills as both a programmer and as a physicist and have encouraged my independence. In particular, I would like to thank Alain Hauchecorne for sharing his scientific expertise on a number of topics and for encouraging me to track down inconsistencies and to be meticulous in the details. I would like to thank Philippe Keckhut for his continued advice in framing my work as part of a larger scientific narrative and for reminding me of the bigger picture.

Many thanks to my “unofficial thesis advisor” Sergey Khaykin for his advice during thesis meetings, for introducing me to wind lidars, giving me advice regarding aerosols, and for being a sympathetic ear when I just needed to chat in English for a while.

Thanks as well to Sophie Godin-Beekman for her support and interest throughout my time here in France. Being a part of the LAVANDE ozone validation campaign at OHP and being invited to attend the 30th anniversary conference for the Montreal Protocol has sparked my interest in ozone science and DIAL systems.

To my thesis advisory committee members Chantal Claud and Albert Hertzog thank you for being there to help guide my thesis to completion and for listening and understanding when I needed it.

To my office neighbour Andrea Pazmino thank you for always saying “Bonjour” and stopping by to chat.

And a very special thanks to my friend and colleague Emily McCullough for helping me refine my ideas and writing and always offering encouragement. Your help as both a co-author and in navigating the peer review process was invaluable so thank you.

Contents

Declaration of Authorship	iii
Abstract	v
Acknowledgements	ix
Contents	xi
List of Figures	xv
List of Tables	xxv
Glossary	xxv
Physical Constants	xxxii
List of Symbols	xxxiii
1 Introduction	1
1.1 The Middle Atmosphere	1
1.1.1 The Stratosphere	3
1.1.2 History	4
1.1.3 Properties	5
1.1.4 The Mesosphere and Lower Thermosphere	6
History	7
1.1.5 Phenomena and Properties	7
1.2 Rayleigh Lidar	10
1.2.1 Limitations on the Rayleigh Lidar Technique	10
1.3 Scope of this Dissertation	11

2	Lidar temperature series in the middle atmosphere as a reference data set. Part A: Improved retrievals and a 20-year cross validation of two co-located French lidars	13
2.1	Author Contribution	13
2.2	Abstract	14
2.3	Introduction	14
2.4	Instrumentation Description	17
2.4.1	Rayleigh Lidar	17
2.4.2	DIAL Ozone System (LiO3S)	18
2.5	Methods	20
2.5.1	Rayleigh Lidar Equation	21
2.5.2	The Raw Counts Lidar Signal	23
2.5.3	Identifying Outliers, Signal Spikes, Signal Induced Noise, and Transient Electronic Interference	24
	Spikes	24
	Transient Electronic Signals	26
	Bad Profiles	27
	Good Profiles	31
2.5.4	Noise Reduction	32
2.5.5	Corrections Applied Before Temperature Calculation	33
	Deadtime Correction	33
	Atmospheric Transmission Correction	35
	Defining the Background	35
2.5.6	Temperature Inversion Equation	38
	Where to start the inversion	41
2.6	Net result of temperature algorithm modifications	42
2.7	20 Year Comparison of OHP Lidar Temperatures	44
2.8	Conclusions	50
2.8.1	Changes to Lidar Temperature Algorithm	50
2.8.2	OHP Lidar 20 Year Comparison	51
3	Lidar temperature series in the middle atmosphere as a reference data set. Part B: Assessment of temperature observations from MLS/Aura and SABER/TIMED satellites	53
3.1	Author Contribution	53
3.2	Abstract	54

3.3	Introduction	54
3.3.1	Lidar as a Validation Tool	55
3.3.2	Previous Lidar-Satellite Temperature Studies	56
3.3.3	Alternative Measurement Techniques	58
3.3.4	Outline of this Work	59
3.4	Instrumentation	59
3.5	Comparison Parameters	60
3.6	Temperature comparisons without considering vertical offset	62
3.6.1	Comparison OHP Lidar and SABER	62
3.6.2	Comparison OHP lidar and MLS	65
3.7	Minimising Temperature Difference Between Lidar and Satellites with a Vertical Offset	67
3.7.1	Method to determine the vertical offset between measurements	68
3.7.2	Trends in Vertical Offset between Lidar and Satellites	72
3.8	Recalculated Lidar-Satellite Temperature Differences	75
3.9	Discussion	79
3.9.1	The need for vertical altitude correction of satellite data	79
3.9.2	Temperature biases between OHP lidar and SABER	79
3.9.3	Temperature biases between OHP lidar and MLS	81
3.9.4	Seasonality of Temperature biases between OHP lidar and satellites	82
3.10	Conclusions	82
4	A new MesosphEO dataset of temperature profiles from 35 to 85 km using Rayleigh scattering at limb from GOMOS/ENVISAT daytime observations	85
4.1	Author Contribution	85
4.2	Relation to Thesis Questions	86
4.2.1	Addressing Uncertainties in A Priori and Sampling	86
4.2.2	Addressing Uncertainty in Geopotential Height	87
4.2.3	Addressing Uncertainty from Tides	89
4.3	Abstract	90
4.4	Introduction	91
4.5	Principle and data processing	93
4.5.1	Method	93
	Data processing	95

Processing one occultation	96
4.6 Validation using Rayleigh lidar observations	97
4.7 First scientific results	101
4.8 Conclusions	106
5 General Conclusions and Future Work	109
5.1 Conclusions	109
5.2 Future Work	112
A Résumé Français	115
Bibliography	129

List of Figures

- | | | |
|-----|--|----|
| 1.1 | Comparison of the 1962 US standard atmosphere graph of geometric altitude against density, pressure, the speed of sound and temperature with approximate altitudes of various objects. Source: NOAA, 1962 | 2 |
| 2.1 | Mirrors A1, A2, A3, A4 (50 cm) are combined for the high gain Rayleigh channel. B (20 cm) is low gain Rayleigh channel. Mirror C&D (80 cm) is the Raman channel for water vapour and molecular nitrogen. E (20 cm) is the Mie channel. The beam expander for the transmitted laser source is between mirrors E and B. | 18 |
| 2.2 | LiO ₃ S DIAL system. 1 355 nm laser source, 2 308 nm laser source, 3 four 530 mm mirrors, 4 four actuator mounted fibre optic cables, 5 mechanical chopper, 6 Horiba Jobin Yvon holographic grating, 7 308 nm high and low gain photomultipliers, 8 331.8 nm photomultiplier, 9 355 nm high and low gain photomultipliers, 10 386.7 nm photomultiplier, 11 Licel transient signal recorder, 12 Signal processing and analysis computer. | 20 |
| 2.3 | Nightly integrated profiles for high and low gain Rayleigh signals for LTA and LiO ₃ S. The background for LTA extends to 246.23 km and for LiO ₃ S extends to 154.13 km. A single lidar profile for both LTA and LiO ₃ S has a temporal resolution of roughly 2 minutes and 45 seconds and a vertical resolution of 75 m. | 23 |
| 2.4 | Tukey Quartile spike identification based on the signal difference between consecutive lidar time bins for short integration lidar returns. An entire night of lidar profiles is over-plotted in the stack plot. The black line is the 2 sigma limit and points above this line are removed. | 25 |

2.5	Upper panel is a surface plot of lidar returns as a function of time bin and profile number. For clarity, only the first 100 bins are shown in this plot. The test is carried out using all bins of each profile. Two instances of TES can be seen as anomalous peaks in the photon count rate. Lower panel is a summation of the fourth statistical moment (kurtosis/skew) for each scan. The red line indicates a 2σ limit on the skew of the population. Points above the limit are excluded.	27
2.6	Example of lidar signal and noise during a night of measurements. Top panel shows the total background counts summed from 120 km to 153 km and the bottom panel shows the total signal summed between 35 km and 40 km. Green bounds are calculated based on a smoothed 2σ error estimation of the summed photon counts. . . .	29
2.7	Rank sum plots for a night of lidar data. Top panel is the cumulative background count and the bottom panel is the cumulative signal count. The signal to noise ratio of the rank summed photon counts in each profile is evaluated using a Mann-Whitney-Wilcoxon rank-sum test to determine if an individual lidar profile belongs to the nightly population of lidar profiles.	30
2.8	This figure shows the improvements in the background count rate due to photomultiplier cooling, new photomultipliers, and new optical filters. Note the logarithmic y-axis and the total reduction of background counts by more than 2 orders of magnitude.	33
2.9	An example of non-linear signal induced noise in the low gain Rayleigh channel best estimated by a quadratic background. Also shown is the high gain Rayleigh channel (red) with a background best fit by a negative linear function and the nitrogen Raman channel (green) with no apparent signal induced noise and a constant background.	38
2.10	An example of a nightly average melded temperature profile from two Rayleigh channels and one Raman channel. The profile is calculated at 300 m vertical resolution from a single combined photon count profile and has a maximum relative error near 80 km of 30%. Black line is the MSIS-90 temperature profile which corresponds to the MSIS-90 pressure and density information we used as an a priori.	41

2.11	Ensemble temperature differences from NDACC standard LTA Rayleigh temperatures (black). MLS (red), SABER (blue with shaded ensemble variance), MSIS-90 (magenta), LiO ₃ S (orange), and LTA Rayleigh temperatures with corrections given in this work (green).	44
2.12	Average number of OHP lidar temperature measurements per month during the period of 1993-2013.	45
2.13	Temperature differences between LTA and LiO ₃ S OHP lidars for a 20 year period between 1993 and 2013. There are 1496 nights of comparison in this plot. Red indicates that LiO ₃ S was warmer than LTA and blue that it was colder. The black boxes highlight periods where the two lidars were out of alignment with respect to each other.	47
2.14	Average temperature differences between LTA and LiO ₃ S OHP lidars for a 20 year period between 1993 and 2013 at four altitude levels: 65-75 km (red), 55-65 km (green), 45-55 km (blue), and 35-45 km (magenta). Shaded uncertainties are shown at 1 sigma for clarity and the black lines are zero temperature difference displaced to 40, 50, 60 and 70 km. All measurements, including periods of lidar misalignment, are included in this plot. The apparent anomalies (blue arrows) occur only during times where the lidars were often misaligned, as indicated in Fig. 2.13.	48
2.15	Ensemble of median temperature differences between LTA and LiO ₃ S based on temperature measurements between 1993 and 2013. Shaded error is the two sigma distribution about the ensemble.	50
3.1	Area defined for coincident measurements (40° N, 9° E) to (48° N, 21° E). L'Observatoire de Havte Provence in blue at (43.93° N, 5.71° E). (Google, 2017)	61
3.2	Example co-located temperature profiles from the OHP lidar (green), SABER (blue), MLS (red), and MSIS (black).	62

3.3	Sixteen year systematic comparison of OHP lidars and SABER temperatures. The monthly median temperature differences between the lidar and SABER are shown in the upper panel. Red indicates that the lidar is warmer than SABER and blue that the lidar is colder. There are 1100 nights of coincident measurements in the colour plot. The lower panel is a seasonal ensemble of lidar minus SABER temperature differences. The summer (May, June, July, August) ensemble in red includes 306 nights of coincident measurements and the winter (November, December, January, February) ensemble in blue includes 397 nights of coincident measurements. Shaded errors represent 1 and 2 standard deviations.	63
3.4	Monthly median temperature difference between lidar and SABER temperature measurements. Red indicates regions where the lidar measures warmer temperatures than SABER and blue regions where the lidar measures colder temperatures than SABER.	65
3.5	Fourteen year systematic comparison of OHP lidar and MLS temperatures. The monthly median temperature differences between the lidars and MLS are shown in the upper panel. There are 1741 nights of coincident measurements. The lower panel is a seasonal ensemble of lidar minus MLS temperature differences. The summer (May, June, July, August) ensemble in red includes 554 nights of coincident measurements and the winter (November, December, January, February) ensemble in blue includes 653 nights of coincident measurements. Shaded errors represent 1 and 2 standard deviations.	66
3.6	Monthly median temperature difference between lidar and MLS temperature measurements. Red indicates regions where the lidar measures warmer temperatures than MLS and blue regions where the lidar measures colder temperatures than MLS.	67
3.7	The upper panel shows a case where the lidar and SABER were well aligned in altitude. The lower panel shows a case where a vertical displacement of the SABER profile ameliorated the agreement with the lidar measurement.	69

3.8	The upper panel shows a case where the lidar and MLS were well aligned in altitude. The lower panel shows a case where a vertical displacement of the MLS profile ameliorated the agreement with the lidar measurement.	70
3.9	Two examples of poor matches between lidar and satellite temperature profiles (MLS upper panel, SABER lower panel). These mismatches mainly occur between late November and early April on nights where the stratosphere was disturbed and experiencing a warming.	71
3.10	The upper panel features the monthly average displacement of SABER measurements with respect to the OHP lidars (green for LTA and blue for LiO ₃ S). The standard deviation is given as the shaded area. The mean offset (magenta) is 1446 m with a standard error of 49 m. The lower panel shows the same analysis with the monthly average MLS displacement. The mean value is 911 m with a standard error of 90 m.	73
3.11	The upper panel features the monthly median temperature differences between the lidar and MLS seen in 3.5 with the estimated vertical displacement of the stratopause height over-plotted. The lower panel features the monthly median temperature differences between the lidar and SABER seen in 3.3 with the estimated vertical displacement of the stratopause height over-plotted. The black line represents comparisons between LTA and the satellite and the grey line represents comparisons between LiO ₃ S and the satellite.	74
3.12	Corrected seasonal temperature differences between the lidar and the vertically displaced SABER temperatures. The magnitude of the temperature differences is reduced in both the stratosphere and mesosphere over the majority of the altitude range when compared to a similar uncorrected temperature difference contour seen in Fig. 3.4.	75
3.13	Corrected seasonal temperature differences between the lidar and the vertically displaced MLS temperatures. The structured nature of the temperature bias seen in Fig. 3.6 remains unchanged by the vertical correction.	76

3.14	Ensemble for lidar minus MLS temperature differences (left) and lidar minus SABER (right). Ensembles for all profiles are on the top row, summer (MJJA) profiles in the middle row, and winter (NDJF) in the bottom row.	78
4.1	Spectrometer signal integrated in the three 20-nm spectral ranges for one occultation on 1st January 2011 (star ID =3, orbit number = 46209), lower background spectrum.	95
4.2	Temperature profiles processed for the same occultation as in Fig. 4.1. The horizontal bar indicates the dispersion (1 standard deviation) between the 6 individual profiles.	97
4.3	Example of comparison between a Rayleigh lidar profile at OHP on 21st October 2003 (in red) and two collocated GOMOS profiles selected using the co-location criteria (in blue and green). When two or more GOMOS profiles are selected, the median profile is used for the statistical comparison. For the lidar profile (red), each individual GOMOS profile (blue) and the median GOMOS profile (green), the standard deviation of its uncertainty is represented by the shaded area.	98
4.4	Statistical median temperature difference between OHP lidar and GOMOS temperature profiles (lidar minus GOMOS temperature). The shaded area represents the dispersion of the differences (one standard deviation).	99
4.5	Amplitude (left panel) and phase (time of the maximum temperature; right panel) of the diurnal tides extracted from the GSWM above 45°N for August. Temperature differences (lidar minus GOMOS; right panel) expected from diurnal atmospheric tides as simulated by the GSWM-00 model.	101
4.6	Monthly climatology of GOMOS Rayleigh temperature. Data are averaged over 10° latitude bins.	102
4.7	Monthly climatology of the temperature difference between GOMOS and the external (ECMWF+MSIS). Data are averaged over 10° latitude bins.	103
4.8	Mean difference between GOMOS Rayleigh temperature and external model temperature as a function of altitude. The standard deviation of the difference is shaded.	104

4.9	Left) Evolution of the weekly averaged temperature profile at Equator obtained using all occultations of the polar star with a tangent point latitude always situated in the interval 0.8°S-0.8°N. Right) Vertical weekly mean profile beginning of May compared to the GOMOS external model.	105
4.10	Seasonal evolution of the equatorial temperature derived from temperature data presented in Fig. 4.2 The altitude of the stratopause is indicated by the white dotted line.	106
A.1	Différences des température moyennes obtenues avec les lidars de OHP, LTA et LiO ₃ S, pendant une période de 20 ans entre 1993 et 2013 à quatre niveaux d'altitude: 65-75 km (rouge), 55-65 km (vert), 45-55 km (bleu) et 35-45 km (magenta). Les incertitudes ombrées sont indiquées en 1 sigma pour plus de clarté et les lignes noires représentent une différence de température nulle décalée à 40, 50, 60 et 70 km. Toutes les mesures, y compris les périodes de mauvais alignement de lidar, sont incluses dans ce graphique. Les anomalies apparentes (flèches bleues) ne se produisent que pendant les périodes où les lidars étaient souvent mal alignés.	116
A.2	Ensemble des différences de température médianes entre LTA et LiO ₃ S basé sur les mesures de température effectuées entre 1993 et 2013. L'erreur ombrée correspond à la distribution en deux sigma de l'ensemble.	117
A.3	Différences de température d'ensemble par rapport aux températures standard NDACC LTA de Rayleigh (noir). MLS (rouge), SABER (bleu avec variance d'ensemble ombrée), MSIS-90 (magenta), LiO ₃ S (orange) et LTA Rayleigh températures corrigées dans cet ouvrage (vert).	118
A.4	Exemple de profils de température co-localisés du lidar OHP (vert), SABER (bleu), MLS (rouge) et MSIS (noir).	119

- A.5 Comparaison systématique sur 16 ans des lidars OHP et des températures SABER. Les différences de température mensuelles médianes entre le lidar et SABER sont indiquées dans le panneau supérieur. Le rouge indique que le lidar est plus chaud que SABER et le bleu que le lidar est plus froid. Il y a 1100 nuits de mesures coïncidentes dans le diagramme de couleurs. Le panneau inférieur est un ensemble saisonnier des différences de température lidar moins SABER. L'ensemble d'été (mai, juin, juillet et août) en rouge comprend 306 nuits de mesures coïncidentes et l'ensemble d'hiver (novembre, décembre, janvier, février) en bleu comprend 397 nuits de mesures coïncidentes. Les erreurs ombrées représentent 1 et 2 écarts types. 120
- A.6 Comparaison systématique sur 14 ans des températures de OHP lidar et de MLS. Les différences de température mensuelles médianes entre les lidars et MLS sont indiquées dans le panneau supérieur. Il y a 1741 nuits de mesures coïncidentes. Le panneau inférieur est un ensemble saisonnier des différences de température lidar moins MLS. L'ensemble d'été (mai, juin, juillet et août) en rouge comprend 554 nuits de mesures coïncidentes et l'ensemble d'hiver (novembre, décembre, janvier, février) en bleu comprend 653 nuits de mesures coïncidentes. Les erreurs ombrées représentent 1 et 2 écarts types. 122
- A.7 Ensemble pour lidar moins MLS différences de température (à gauche) et lidar moins SABER (à droite). Les ensembles de tous les profils sont situés dans la rangée supérieure, les profils d'été (MJJA) dans la rangée centrale et d'hiver (NDJF) dans la rangée inférieure. 125
- A.8 Exemple de comparaison entre un profil lidar de Rayleigh à OHP le 21 octobre 2003 (en rouge) et deux profils GOMOS colocalisés sélectionnés à l'aide des critères de co-localisation (en bleu et vert). Lorsque deux ou plusieurs profils GOMOS sont sélectionnés, le profil médian est utilisé pour la comparaison statistique. Pour le profil lidar (rouge), chaque profil individuel GOMOS (bleu) et le profil médian GOMOS (vert), l'écart type de son incertitude est représenté par la zone ombrée. 126

A.9	Différence de température médiane statistique entre les profils de température lidar OHP et GOMOS (température lidar moins GOMOS). La zone ombrée représente la dispersion des différences (un écart type).	127
-----	---	-----

List of Tables

2.1 Specifications for the LTA receiver assembly. 17

Glossary

- AMSU** Advanced Microwave Sounding Unit. 91
- AO** Annual Oscillation. 57, 82
- CHAMP** Challenging Minisatellite Payload. 15, 57
- CIRA-72** COSPAR International Reference Atmosphere 1972. 38
- CIRA-86** COSPAR International Reference Atmosphere 1986. 57
- COSMIC** Constellation Observing System for Meteorology, Ionosphere and Climate. 15, 57
- DIAL** Differential Absorption Lidar. xv, 14, 16, 18–20, 51, 64, 109
- ECMWF** European Centre for Medium-Range Weather Forecasts. xx, 90, 102, 103, 107
- ENVISAT** ENVironmental SATellite. 93, 104
- ERA-interim** ECMWF meteorological reanalysis. 112
- ESA** European Space Agency. 92, 106
- GHG** Greenhouse Gas. 91
- GNSS** Global Navigation Satellite System. 91
- GOMOS** Global Ozone Monitoring by Occultation of Stars. v, vi, xx, xxi, 12, 85, 87–90, 93, 95, 96, 98–105, 107, 112
- GSWM** Global Scale Wave Model. xx, 99–101
- HALOE** Halogen Occultation Experiment. 15, 57

- LAVANDE** LidAr VALidation NDacc Experiment. 52
- LiO₃S** Lidar Ozone Stratosphère. xv, xvii, xix, 18, 20, 23, 42, 44–50, 64, 72–74
- LTA** Lidar Température et Aérosols. xv, xvii, xix, xxv, 16, 17, 23, 42–50, 64, 72–74
- LTE** Local Thermodynamic Equilibrium. 22
- MA** Middle Atmosphere. 9, 91
- MesosphEO** Exploitation of the Mesosphere, European Space Agency Project. 92, 107
- MIL** Mesospheric Inversion Layer. 105, 107
- MIPAS** Michelson Interferometer for Passive Atmospheric Sounding. 15
- MLS** Microwave Limb Sounder (on the Aura satellite). v, vi, xvii–xx, 9, 12, 43, 44, 50, 54–60, 62, 65–68, 70–74, 76–79, 81–83, 85–90, 92, 98, 110–113
- MSIS** Mass Spectrometer and Incoherent Scatter Radar, (a model derived from). xvi, xvii, xx, 34, 35, 38–41, 43, 44, 57, 62, 90, 103
- NASA** National Aeronautics and Space Administration. 52, 59, 83
- NDACC** Network for the Detection of Atmospheric Composition Change. xvii, 10, 14–16, 38, 42–44, 51, 52, 57, 86, 92, 97, 109, 112
- NRLMSISE-00** US Naval Research Laboratory Mass Spectrometer and Incoherent Scatter Radar including Exosphere - 2000, (a model derived from). 96, 102, 104, 107
- NWP** Numerical Weather Prediction. 92
- OHP** Observatoire de Haute Provence. xvii–xx, 9, 12, 14–19, 24, 33, 34, 44–48, 52, 54, 55, 59–66, 73, 79, 80, 85, 89, 97–100, 107, 109–113
- OSIRIS** Optical Spectrograph and InfraRed Imager System. 92
- PMCs** Polar Mesospheric Clouds. 96

PMT Photomultiplier Tube. 34

RF Radio Frequency. 26

SABER Sounding of the Atmosphere using Broadband Emission Radiometry (on the TIMED satellite). v, vi, xvii–xx, 9, 12, 15, 43, 44, 50, 54, 56–65, 68, 69, 71–83, 85–87, 89, 92, 98, 99, 110, 111, 113

SNR Signal to Noise Ratio. 31, 36, 37

SPARC Stratosphere-troposphere Processes And their Role in Climate. 38

SSU Stratospheric Sounder Unit. 91

SSW Sudden Stratospheric Warming. 6

TES Transient Electronic Signals. xvi, 26, 27, 42

TIMED Thermosphere Ionosphere Mesosphere Energetics Dynamics (satellite). 59, 60, 92, 98, 99

UARS Upper Atmosphere Research Satellite. 57, 92, 97

UMLT Upper Mesospheric and Lower Thermosphere. 14, 16, 22, 24, 32, 33, 35, 36, 41, 42, 50, 60, 86, 109

UTC Temps Universel Coordonné (Coordinated Universal Time). 60

UV Ultraviolet light. 92

WINDII WIND Imaging Interferometer. 92

Physical Constants

Gravitational acceleration	$g = 9.81 \text{ m s}^{-2}$ (approx.)
Ideal gas constant	$R = 8.314 \text{ J mol}^{-1} \text{ K}$ (approx.)
Molar mass of dry air	$M = 0.028964 \text{ kg mol}^{-1}$ (approx.)
Speed of Light	$c_0 = 2.99792458 \times 10^8 \text{ m s}^{-1}$ (exact)

List of Symbols

P	pressure	Pa
T	temperature	K
ρ	density	kg m^{-3}
h	fluid column height	m
N	photon count rate	MHz
z	height above lidar detector	m
ξ	lidar system efficiency	unitless fraction
τ_x	atmospheric transmittance (direction)	unitless fraction
λ	photon wavelength	nm
O	lidar overlap function	unitless fraction
P_{laser}	laser power	W
σ_{cross}	backscattering cross section	m^{-2}
n	number density of scatterers	m^{-3}
A	telescope area	m^2
t	time	s
B	background count rate	MHz
σ	standard deviation/error	unitless
S	signal in SNR	photon counts
N	noise in SNR	photon counts
τ	deadtime correction coefficient	unitless
Φ	geopotential height	$\text{m}^2 \text{s}^{-2}$
ϕ	latitude	degrees

1 Introduction

1.1 The Middle Atmosphere

The middle atmosphere is the portion of Earth's atmosphere which extends from the tropopause (~ 8 - 16 km depending on season and latitude) to the turbopause (~ 100 km) and is comprised of the stratosphere, mesosphere, and lower thermosphere.

Interest in this region is driven primarily by studies of upper tropospheric and lower stratospheric composition. In particular, studies of water vapour trends (Forster and Shine, 2002) and studies of the dynamics and chemistry of stratospheric ozone (Dobson, Harrison, and Lawrence, 1929), (Bourassa et al., 2014) have been crucial for the formation of public policy with respect to the larger context of global atmospheric and climate change (IPCC, 2013). In addition, studies of wave driven dynamics and mean atmospheric circulation (Brewer, 1949), (Dobson, Harrison, and Lawrence, 1929) as well as studies of winds and turbulence (McIntyre and Palmer, 1983) ask fundamental geophysical questions of atmospheric fluid dynamics and the non-linear behaviour of waves. Of particular interest for this work are studies of temperature profiles and the reported trends occurring in the middle atmosphere (Ramaswamy et al., 2001), (W. J. Randel, 2009). Given that temperature is one of the fundamental atmospheric parameters, intrinsically coupled to pressure and density, the assessment of the accuracy and stability of these measurements cannot be over stated.

In contrast to the lower atmosphere the layers of the middle atmosphere can generally be characterised as cold, dry, tenuous, and relatively clean of complex optical scatterers like aerosols and clouds. The key physical parameters of the middle atmosphere which are relevant for this work are shown in figure 1.1.

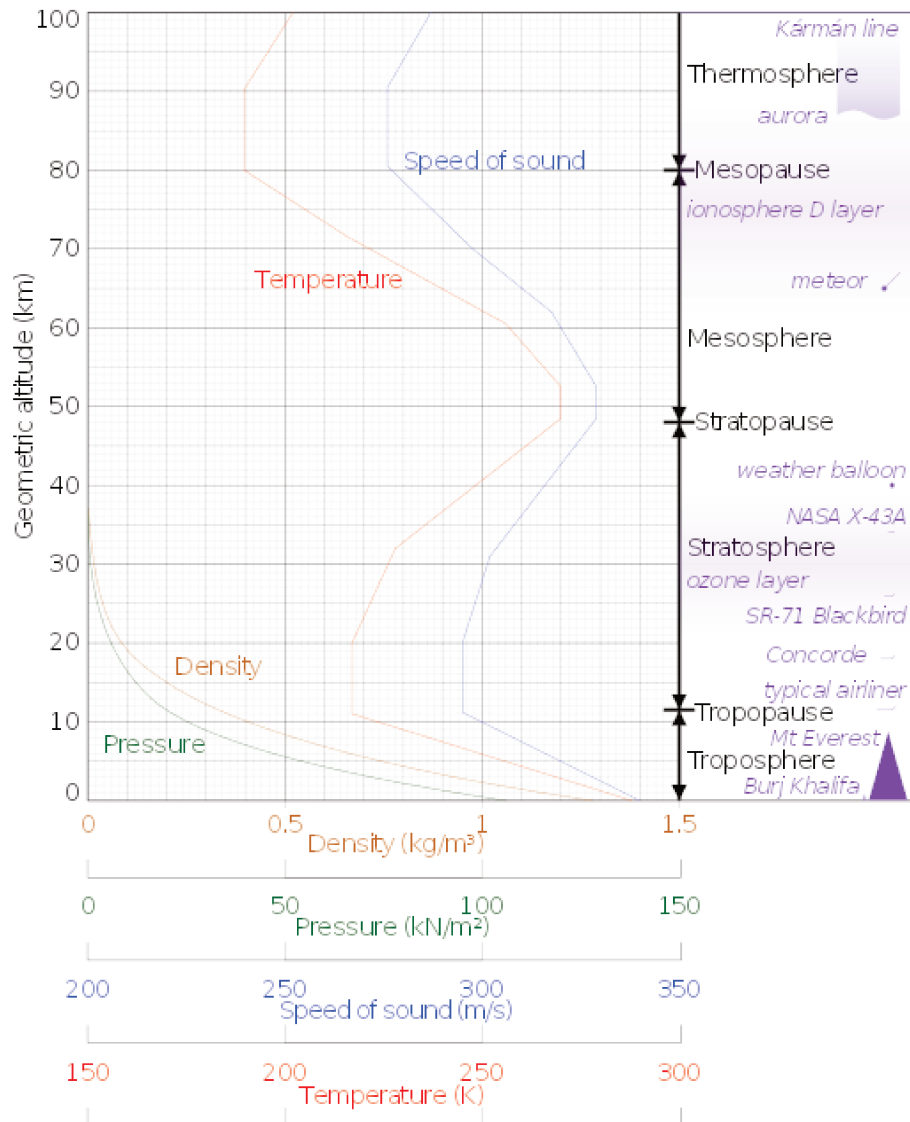


FIGURE 1.1: Comparison of the 1962 US standard atmosphere graph of geometric altitude against density, pressure, the speed of sound and temperature with approximate altitudes of various objects. Source: NOAA, 1962

The middle atmosphere is dynamically coupled to the troposphere by way of atmospheric waves (T. G. Shepherd, 2002) and is forced by radiation from the Sun (Keating and Chen, 1991), (Haigh, 1996). As a result, it offers us a unique natural laboratory for the study of atmospheric processes and the monitoring of climatic change. Observational and modelling studies of physical variables (e.g. temperature, pressure, and density) and chemical composition in the middle atmosphere are of great use for monitoring the rate of climactic change as the increasing burden of CO₂ will provide a positive radiative forcing on the lower atmosphere. Additionally, the magnitude of the observed temperature trends in the stratosphere and mesosphere are expected to be of a much larger magnitude than the near surface tropospheric trends as total gas density is lower and the radiative cooling to space is more direct. Stratospheric cooling since the 1980s has been measured to be near 0.5 K per decade in the lower stratosphere, around 2 K per decade near the stratopause (Ramaswamy et al., 2001), and nearly 3 K per decade in the mesosphere (Beig et al., 2003). The measurement of lower stratospheric temperature is an important research topic as it answers fundamental questions about the nature of ozone recovery, aerosol loading, physical wave-driven processes like the Quasi-biennial oscillation, and variations in solar forcing (Steinbrecht et al., 2003). In order to fully separate these processes and understand the component drivers of our atmospheric environment we require precise, accurate and well calibrated measurements on both a global and local scale.

1.1.1 The Stratosphere

Most studies of the stratosphere focus on the important and life preserving ozone layer as well as the measurements and tracking of pollutants which degrade ozone. The ozone layer absorbs solar UV radiation which is hazardous to terrestrial life. The introduction of assorted ozone depleting halocarbon compounds into many manufacturing processes led to the ozone layer depletion crisis of the 1970s. The resulting Antarctic ozone hole precipitated a rush of studies and scientific interest in the stratosphere and culminated in the successful implementation of the Montreal Protocol which placed restrictions on several key ozone depleting substances. In addition to ozone studies, the stratosphere is also home to several synoptic and global scale wind patterns which greatly influence the tropospheric meteorology

and the seasonal weather that we experience on the surface. Outside of geophysical research, the stratosphere is proving to be of interest to both professional and amateur astronomers and photographers as complex government funded telescopes and iPhones alike are launched on balloons to take pictures of our planet and the cosmos which surrounds it.

1.1.2 History

Early studies of atmospheric temperature and pressure conducted in 1647 by French mathematician Blaise Pascal established the relationship shown in Eq. 1.1 which would later be referred to as Pascal's Law. This relation holds that the change in hydrostatic pressure, ΔP , is related to the difference in elevation within a fluid column, δh , times the gravitational acceleration, g , and the density of the fluid, ρ (Pascal, 1664). Based on this simple relationship we are left with the somewhat simplistic idea of an atmosphere limited in vertical extent, lacking internal structure, and surrounded by vacuum.

$$\Delta P = \rho g \delta h \tag{1.1}$$

Prior to the invention of modern atmospheric measurement techniques like radiosondes, lidars, or satellites, vertical profiles of atmospheric temperature and pressure were determined by carrying a thermometer and a barometer up a mountain and taking regular measurements. In 1787 Swiss physicist Horace-Bénédict de Saussure climbed Mont Blanc in the Alps and made measurements of temperature and pressure up to nearly 5 km. From Saussure's data a vertical temperature gradient (also known as a temperature/environmental lapse rate) of ~ 0.7 K per 100 m was estimated. Modern measurements have the average environmental lapse rate as 0.65 K per 100 m (Wallace and Hobbs, 1977). Extrapolating from these data Hermann von Helmholtz estimated that the atmosphere would reach an equivalent temperature of -300 °C above 40 km, a temperature which was beyond comprehension at the time. The understanding of Earth's atmosphere until the end of the 19th century was of a layer of gas which had an exponential decrease in pressure with altitude and a constant decrease in temperature with altitude. The whole atmosphere was assumed to be only a few kilometres in vertical extent

and the problem of the extremely cold temperatures at high altitude remained unsolved. Lord Kelvin would establish the idea of $-273\text{ }^{\circ}\text{C}$ as an “absolute zero” in 1848 almost 60 years later in part driven by the questions raised from atmospheric temperature studies.

In 1902 Teisserenc de Bort published 10 years of balloon measurements made near Trappes, France and showed that between 8 km and 13 km the temperature did not drop with altitude as was previously assumed (Teisserenc de Bort, 1902). Based on these measurements, De Bort decided to divide the atmosphere into two spheres. The troposphere, below 8 km, was characterised as having a negative environmental lapse rate and the isotherm region between 8 and 13 km was shown to have an average lapse rate of zero. Coincident with the publication of de Bort, Richard Aßmann published balloon measurements which showed that the atmosphere began to warm above 10 km and exhibit a mean wind above the isothermal region (Aßmann, 1902).

1.1.3 Properties

In general, the stratosphere can be characterised by a positive lapse rate and an increase in the concentration of ozone with altitude. The increase in temperature with height is driven by the absorption of UV light by the ozone molecule and was first shown by Sydney Chapman (Chapman, 1930). As a result of this positive lapse rate the stratosphere is rather dynamically stable to convection and has limited amounts of vertical mixing of air parcels. The clear vertical stratification of the stratosphere with respect to the troposphere has the consequence of producing an atmospheric layer that is dry, largely free of aerosol contaminants, and relatively unaffected by the tumultuous convection which dominated the layer below. Exceptions to this dry, clean and clear state can occur in the lower stratosphere when large thunder storms force moist air into the stratosphere by overshooting the tropopause and when aerosol loading occurs due to volcanic eruptions (Haywood, A. Jones, and G. S. Jones, 2013). Dust (Weinzierl et al., 2017), and forest fire smoke (S. M. Khaykin, Godin-Beekmann, A. Hauchecorne, et al., 2018) can also enter the lower stratosphere during periods of intense biomass burning. The other major source of mixing between the troposphere and stratosphere is the Brewer-Dobson cycle (Brewer, 1949), (Dobson, Harrison, and Lawrence, 1929).

When warm, moist air rises in the tropics it creates a simple wave-driven circulation from the equator to the poles and transports ozone, water vapour, and energy towards the mid-latitudes (Holton et al., 1995). The relative abundance of these two chemicals can directly affect the temperature of the lower stratosphere and the wave driven transport of energy can modify short to medium term synoptic flows causing local changes to the vertical temperature profile.

Of particular interest when discussing stratospheric temperature profiles are Sudden Stratospheric Warming events (SSW). A SSW generally occurs in the winter and can be seen by a rapid rise in temperature on the order of dozens of Kelvins over the course of a few days. These unique phenomena occur when the dominant zonal winds weaken or reverse direction. Typically, the winds that form the polar jet blow west to east and act to isolate Arctic air in the so-called polar vortex. However, large low pressure systems in the troposphere and vertically propagating waves can perturb this zonal jet and cause an unbalanced state in the mean flow (Triplett et al., 2017). To conserve energy and momentum the stratosphere collapses downwards adiabatically and undergoes rapid warming due to compression of the air. These events are often precede the appearance of easterly circumpolar winds and increases meridional flow in the troposphere (Matsuno, 1971). Since these events are important in meteorological weather forecasting, the best possible measurements are required from our space based remote sensing instruments.

1.1.4 The Mesosphere and Lower Thermosphere

The mesosphere is the least studied portion of Earth's atmosphere primarily due to its location above the range of in situ measurements by typical balloon borne sondes and aircraft. Measurements of this layer are only possible by use of rocket-sonde or by remote sensing techniques like radar, lidar, and satellites. The extreme difficulty in making measurements in this region has led many scientists to jokingly refer to the mesosphere as the "ignorosphere". In spite of this unfortunate nickname, the mesosphere is a complex and scientifically interesting part of the middle atmosphere which exists near the edge of space and is subject to wave-driven perturbations from below as well as radiative and electrical perturbations from above.

Recently, “space tourism” has become fashionable for the ultra-wealthy necessitating the need for measurements and models to extend higher into the atmosphere to offer so-called “space weather prediction”.

History

Tracing the history of the mesosphere is an inexact exercise as this region of the middle atmosphere has historically never had the focused scientific interest boasted by the stratosphere below it or by the ionosphere at its upper reaches and above it. The presence of the mesosphere can be inferred from the 1839 work of Carl Friedrich Gauss - *General Theory of Terrestrial Magnetism* (English translation (H. Glassmeier and T. Tsurutani, 2014)) in which Gauss predicts the existence of an electrically charged layer high above the stratosphere. This electrically charged layer, later named the ionosphere, was exploited by Guglielmo Marconi in 1901 to send a trans-atlantic radio frequency telegraph from Poldhu, Cornwall to St. John's, Newfoundland. The existence of a layer of gas between the stratosphere and this electrically conducting layer was assumed but not measured.

Scientific measurements of the middle atmosphere were first proposed in a 1919 paper by Robert H. Goddard entitled “A Method of Reaching Extreme Altitudes” (Goddard, 1919). Routine rocket measurements of the mesosphere were started in the aftermath of the second world war and were well established as a branch of atmospheric research by the 1950s (Boyd, 1954). Several of the atmospheric models used in this manuscript like the US Standard Atmosphere, have their origins in this early rocket work.

1.1.5 Phenomena and Properties

The mesosphere and lower thermosphere are home to some of the most spectacular optical and dynamic phenomena in Earth's atmosphere. Chief among them are the aurorae which occur in the high-latitude regions of the planet and are the result of high energy solar particles colliding with the atmosphere. These beautiful spectacles are understood only by combining our understanding from otherwise unrelated disciplines of molecular spectroscopy, atmospheric physics, geomagnetics,

solar fluxes, and the fluid dynamics of charged flows. Similarly, transient luminous events are another class of interesting mesospheric phenomena. Colloquially referred to as “upper-atmospheric lightning” these events include so-called “red sprites” (Stratospheric/mesospheric Perturbations Resulting from Intense Thunderstorm Electrification), “elves” (Emission of Light and Very Low Frequency perturbations due to Electromagnetic Pulse Sources) and “blue jets” (Williams, 2001). All three of these phenomena occur in the upper middle atmosphere as a result of large thunder storms in the troposphere. The mathematics behind these electrical phenomena is elegant, complex, and as yet incomplete (Pasko, 2006).

In contrast to the stratosphere, the mesosphere has a negative temperature lapse rate and is primarily cooled by radiative emission from carbon dioxide. As was alluded to earlier, investigations of long-term temperature trends in the mesosphere are of particular interest for climate change studies as the measured changes are an order of magnitude larger than they are at the surface. Modelling studies suggest that a doubling of CO_2 and CH_4 in the atmosphere would yield a net cooling in the mesosphere between 10 and 50 K (Roble and Dickinson, 1989). The cooling around the stratopause, central to our work in validating middle atmospheric temperatures, is expected to be about 10 to 12 K given a similar doubling of greenhouse gasses.

It is probable that noctilucent clouds (Lubken, Berger, and Baumgarten, 2018) are another mesospheric telltale of climate change as their observed frequency corresponds closely with the recent increases in greenhouse gas concentration. Noctilucent clouds are ice clouds which appear during the summer months near the mesopause region at high latitudes. The clouds can form in the cold summer mesosphere in the presence of dust and water vapour. The dust is generally thought to be of volcanic origin or to come from the ablation of meteors in the upper atmosphere. The water vapour primarily enters the mesosphere from two sources, the first being advection and mixing of water vapour from lower altitudes and the second being the photo-dissociation of methane (Thomas and Olivero, 2001). Recent modelling studies have correlated increasing concentrations of carbon dioxide, methane and water vapour, with cooling mesospheric temperatures and increased observational frequency of noctilucent clouds (Lubken, Berger, and Baumgarten, 2018). The study also made use of lidar data sets to confirm that as the mesosphere cools in response to increased emissions from carbon dioxide, the total atmospheric column shrinks and the average altitude of the noctilucent clouds descends. The

largest constraint for further study remains a lack of observations - a niche which the unified lidar database presented in this thesis is well suited to fill.

The general circulation of the mesosphere varies seasonally. In the summer the zonal mean flow is westward and in the absence of significant wave driving the region is dominated by rising air parcels and relatively warm temperatures. However, this is not the case in the winter where wave breaking has a profound effect on the middle atmosphere. As previously mentioned, wave breaking in the stratosphere leads to a breakdown of the zonal mean flow and a residual circulation is forced from the equator to the winter pole. In the mesosphere, these same wave breaking phenomena reverses the direction of the pole to pole flow and air moves towards the winter pole. By moving air to the winter pole the atmospheric column is forced to rise adiabatically and experience a rapid cooling at mesospheric altitudes. As a result of these wave-driven circulations the summer mesopause is the coldest part of the atmosphere and can have temperatures below 130 K (Vincent, 2015). Accurately measuring the temperature of the summer mesopause is a difficult task as it is often beyond the operational scope of many satellite missions and is too high for smaller lidar systems. We present a comparison of lidar to SABER (a satellite focused on the middle atmosphere) in figures 3.3, 3.4, and of lidar to MLS (a satellite focused on the troposphere and lower stratosphere) in figures 3.5, 3.6. We can clearly see the seasonal variation in SABER near 80 km but MLS temperatures appear insensitive to season.

Sampling is the key limitation to understanding and quantifying the trends and dynamics in the mesosphere. A lack of measurements, inconsistency between measurements from different satellite missions, large uncertainties in upper mesospheric and thermospheric densities, and disagreements between models and measurements (Lastovicka, 2017) all serve as confounding variables to MA studies. Our unified OHP (Observatoire de Haute-Provence) lidar temperature database can provide a useful validation source for groups attempting to reconcile different satellite databases as well as provide density measurements over the time period of 1978 to 2018.

1.2 Rayleigh Lidar

Rayleigh lidar is a remote atmospheric sounding technique which relies on the elastic back-scatter of transmitted laser light from target molecules in the atmosphere. The pulsed laser light allows for a high degree of precision in determining the origin altitude of the target molecule with respect to the lidar station. A relative density profile is then inferred based on the number of returned photons from a particular range of altitudes. Following the iterative technique developed by (Alain Hauchecorne and M.-L. Chanin, 1980a) an a priori pressure is assumed at the top of the atmosphere and an absolute pressure and temperatures profile can be calculated. Pure Rayleigh temperature profiles are generally calculated in an iterative manner from above 100 km down to 30 km and are limited primarily by laser power, telescope size and optical efficiency in the transmission and receiver assemblies. However, when supported by other lidar techniques like Raman or metallic resonance lidar, the temperature profiles can be extended to cover ranges from 1 km to over 110 km (Alpers et al., 2004).

1.2.1 Limitations on the Rayleigh Lidar Technique

Given that the raw data of a Rayleigh lidar profile are photon counts, the base uncertainty for the lidar profiles follows the Poisson error statistics for discrete counting (Bevington and Robinson, 1992). Two statistical errors are immediately evident at the low signal to noise ratio end of the lidar measurement: the fundamental noise floor presented by the Poisson uncertainty and the error introduced by integration and smoothing. The two problems are connected as the solution for low signal to noise ratio is a larger window for either temporal or vertical integration. It then becomes a balance between tolerating uncertainty in the absolute temperature profile versus losing information in time or altitude. We fully explore this uncertainty analysis in Chapter 2 and the formal NDACC definitions for temperature and vertical resolution are given by LeBlanc et al. (T. Leblanc, R. J. Sica, et al., 2016), (T. Leblanc et al., 2016).

The third major limitation of the Rayleigh lidar technique comes from the error associated with the assumption of an a priori pressure at the top of the atmosphere.

As previously stated the iterative technique for generating a lidar temperature profile from a measured relative density profile involves the assumption of a starting pressure. Unfortunately, pressures in the mesosphere and lower thermosphere are not well measured as a function of altitude and many of the models are based on density measurements from old rocket programmes or low resolution climatological averages from radar data. It is notoriously difficult to estimate the pressure at these altitudes with both accuracy and precision. The uncertainty (and possible inaccuracies) in our pressure a priori affect the top 10 to 15 km of the lidar temperature profile (T. Leblanc and Alain Hauchecorne, 1997) and it is standard practice to discard this data. (J. Khanna, R. J. Sica, and McElroy, 2011) and (J. Khanna et al., 2012) have estimated the contribution of a poor a priori choice on the resulting lidar temperature profile. They found that a small 10 percent variation in the a priori pressure can result in a 25 K difference in the lidar temperature and that the full effects of a priori choice are not fully eliminated until below 75 km.

Recently, (R. Sica and Haefele, 2015) have proposed an Optimal Estimation Method for the retrieval of lidar temperature profiles which relies on Bayesian statistics and allows for the quantification of the complete lidar error budget. This method is extremely promising and after extensive validation of multiple lidar datasets may be considered a viable candidate to replace or supplement the iterative approach.

A final limitation to the Rayleigh lidar technique is that it can only be employed on clear or partly clear nights. Mie scattering from optically thick clouds reduces the signal amplitude of the lidar. Daytime measurements are possible but are rarely conducted as the lidar requires expensive optical filters to exclude the light from the sun.

1.3 Scope of this Dissertation

The objectives of this dissertation are to:

1. Show that ground based lidar temperatures are a stable, accurate and precise dataset which can be relied upon for satellite validations as well as climatological studies. We will do this by developing data processing tools and

algorithms which minimise known temperature errors which occur due to the initialisation of the lidar algorithm and by comparing two co-located, independent lidars operating at two different laser wavelengths over a 20 year period. This is the first such multi-decadal temperature comparison between two lidars. The results of this work are published (R. Wing, A. Hauchecorne, P. Keckhut, Godin-Beekmann, S. Khaykin, McCullough, et al., 2018).

2. Show that the cross-validated lidar temperature database, described above, is useful for comparing with satellite data from SABER and MLS and may be useful in identifying possible biases in the space borne instruments. This will be the first time that the entire lifetime satellite temperature database, for these two space borne radiometers, will be compared to a continuous lidar data record. The results of this work are under review (R. Wing, A. Hauchecorne, P. Keckhut, Godin-Beekmann, S. Khaykin, and McCullough, 2018a).
3. Address concerns raised during the discussion of (R. Wing, A. Hauchecorne, P. Keckhut, Godin-Beekmann, S. Khaykin, and McCullough, 2018a) regarding the direct comparison of lidar temperature profiles which are a function of geometric altitude and temperature profiles from space borne radiometers which estimate geopotential co-ordinates from inferred pressure levels. The comparison of the lidar temperature profiles to the temperature profiles from GOMOS, which are also presented as a function of geometric altitude, provides some degree of certainty for the previous work done with comparisons to temperature profiles from SABER and MLS. In addition, we investigate the potential tidal contribution to the temperature differences reported between the lidar and GOMOS. Given that both MLS and GOMOS are on sun synchronous orbits there is a temporal offset between the satellite overpasses of OHP and the night time measurements made by the lidar. The results of this work are under review (A. Hauchecorne, Blanot, et al., 2018).

2 Lidar temperature series in the middle atmosphere as a reference data set. Part A: Improved retrievals and a 20-year cross validation of two co-located French lidars

¹

2.1 Author Contribution

Robin Wing conceived the idea to minimise lidar initialisation bias at the top of the lidar temperature profile. He wrote and tested the codes for a data selection and temperature retrieval which produced a new OHP lidar temperature database. He ran the comparison between the LiO₃S and LTA temperature profiles and calculated the statistics and comparison parameters. He collected the most recent system specifications for both lidar systems and detailed the changes to the temperature algorithm, and wrote the manuscript.

¹Wing, R., Hauchecorne, A., Keckhut, P., Godin-Beekmann, S., Khaykin, S., McCullough, E. M., Mariscal, J. F., and d'Almeida, É. (2018). *Lidar temperature series in the middle atmosphere as a reference data set. Part A: Improved retrievals and a 20-year cross-validation of two co-located French lidars*. Atmospheric Measurement Techniques, European Geosciences Union, 11(10), pp.5531-5547.

2.2 Abstract

The objective of this paper and its companion (R. Wing, A. Hauchecorne, P. Keckhut, Godin-Beekmann, S. Khaykin, and McCullough, 2018b) is to show that ground based lidar temperatures are a stable, accurate and precise dataset for use in validating satellite temperatures at high vertical resolution. Long term lidar observations of the middle atmosphere have been conducted at the Observatoire de Haute-Provence (OHP), located in southern France (43.93° N, 5.71° E), since 1978. Making use of 20 years of high-quality co-located lidar measurements we have shown that lidar temperatures calculated using the Rayleigh technique at 532 nm are statistically identical to lidar temperatures calculated from the non-absorbing 355 nm channel of a Differential Absorption Lidar (DIAL) system. This result is of interest to members of the Network for the Detection of Atmospheric Composition Change (NDACC) ozone lidar community seeking to produce validated temperature products. Additionally, we have addressed previously published concerns of lidar-satellite relative warm bias in comparisons of Upper Mesospheric and Lower Thermospheric (UMLT) temperature profiles. We detail a data treatment algorithm which minimises known errors due to data selection procedures, a priori choices, and initialisation parameters inherent in the lidar retrieval. Our algorithm results in a median cooling of the lidar calculated absolute temperature profile by 20 K at 90 km altitude with respect to the standard OHP NDACC lidar temperature algorithm. The confidence engendered by the long term cross-validation of two independent lidars and the improved lidar temperature dataset is exploited in (R. Wing, A. Hauchecorne, P. Keckhut, Godin-Beekmann, S. Khaykin, and McCullough, 2018b) for use in multi-year satellite validations.

2.3 Introduction

Rayleigh lidar remote sounding of atmospheric density is an important tool for obtaining accurate, high resolution measurements of the atmosphere in regions which are notoriously difficult to measure routinely or precisely. A key strength of this technique is the ability to retrieve an absolute temperature profile from a measured relative density profile with high spatio-temporal resolution, accuracy and precision. This kind of measurement is exactly what is required to detect

long-term middle atmospheric temperature trends associated with global climate change and is of great value for routine satellite and model validation (Philippe Keckhut et al., 2004a).

Comparisons of middle atmospheric temperatures measured from satellites to those measured from lidars have all noted a relative warm bias in lidar temperatures above 70 km. Several recent examples of lidar-satellite relative warm bias in the upper mesosphere can be found in the work of: (Kumar, Rao, and Krishnaiah, 2003) [5-10 K relative to HALOE]; (Venkataraman Sivakumar et al., 2011) [5-10 K relative to HALOE, 6-10 K relative to COSMIC/CHAMP, 10-16 K relative to SABER]; (Yue et al., 2014) [13 K at 75 km relative to SABER]; (García-Comas et al., 2014a) [3-4 K at 60 km relative to SABER and MIPAS]; (Yue et al., 2014) [13 K at 75 km relative to SABER]; (Dou et al., 2009) [4 K at 60 km relative to SABER]; (Remsburg et al., 2008) [5-10 K at 80 km relative to SABER]; and (Taori, Kamalakar, et al., 2012; Taori, Jayaraman, et al., 2012) [25 K near 90 km relative to SABER]. The bias is generally attributed to lidar ‘initialisation uncertainty’ and model a priori contributions to the temperature retrieval but, no systematic attempts are made to fully establish this conclusion. These authors also explore the possible influences of tides, lidar-satellite co-incidence criteria, satellite vertical averaging kernels, and satellite temperature accuracy as possible contributing factors.

The work of this paper is to evaluate the suitability of lidars as a reference dataset and to address the problem of systematic errors due to initialisation of the lidar algorithm. The subsequent comparison of the improved lidar temperatures to satellite measurements is conducted in the companion paper (R. Wing, A. Hauchecorne, P. Keckhut, Godin-Beekmann, S. Khaykin, and McCullough, 2018b).

This work follows three main goals: i) the introduction of the long term data set and the instrumental changes, ii) treatment of this heterogeneous data set for use in the accompanying paper, and iii) improvement of the temperature algorithm and reduction of the warm bias compared to satellite soundings. These goals cannot be completely separated from each other, but goal i) is broadly addressed in sections 2.4.1 to 2.5.2 and 2.5.4; goal ii) is addressed in sections 2.5.3 to 2.5.4 and again in sections 2.5.5 - 2.6, and goal iii) is addressed in section 2.7.

Section 2.4 of this paper describes the current experimental setup, the specifications of two OHP lidars, and the measurement cadence of two key NDACC

(Network for the Detection of Atmospheric Composition Change) lidar systems.

Section 2.5 of this paper outlines techniques to minimise the magnitude of the aforementioned lidar-satellite temperature bias by systematically detailing a rigorous procedure for the treatment and selection of raw lidar data and will propose improvements to the standard NDACC lidar temperature algorithm for the UMLT (Upper Mesosphere and Lower Thermosphere) region.

Section 2.6 of this paper gives the net results of the temperature modifications and system improvements in the LTA lidar at OHP.

Section 2.7 of this paper compares the lidar temperatures produced by an NDACC certified temperature lidar at 532 nm with temperatures produced by the non-absorbing 355 nm line of a co-located NDACC certified ozone DIAL (Differential Absorption Lidar) system. This comparison is conducted using a large database of two co-located lidar systems with the goal of providing confidence in the long-term stability of the lidar technique at both wavelengths. There are currently 10 certified temperature lidars, 6 of which are current in their data submission and have temperature profiles freely accessible online. Similarly, there are 12 certified stratospheric ozone DIAL systems of which 5 systems are current with data submission and are available through the NDACC website. We hope that this work will encourage sites with outstanding data obligations to submit their measurements and for DIAL ozone sites to seek validation for their temperature data products for inclusion in the NDACC database (*NDACC Lidar n.d.*). As an ancillary goal we will show that temperatures produced by the Rayleigh lidar technique are accurate, precise and stable over multiple decades and as such are the ideal type of measurement for use in future ground based validation of satellite temperatures. The result of this demonstration will be used in the companion paper (R. Wing, A. Hauchecorne, P. Keckhut, Godin-Beekmann, S. Khaykin, and McCullough, 2018b) as justification for validating satellite data with lidar temperatures.

2.4 Instrumentation Description

2.4.1 Rayleigh Lidar

The OHP Rayleigh-Mie-Raman lidar, LTA (Lidar Température et Aérosols), uses a seeded Nd:YAG to produce a 532 nm laser source with a maximum power of 24 W. The transmitted beam is passed through a 13X beam expander and has a 30 Hz repetition rate, a 7 ns pulse width, and a beam divergence of less than 0.1 mrad.

The receiver assembly consists of a high and low gain elastic channel for 532 nm, a Mie scatter channel at 532 nm for aerosols, a Raman channel at 607 nm for molecular nitrogen, and a Raman channel at 660 nm for water vapour. A schematic of the telescope array is shown in Fig. 2.1. The high gain Rayleigh channel consists of four telescopes. At the focal point of each telescope is an actuator-mounted 400 μm diameter fibre optic. The four fibre optics are bundled to project a single signal onto a Hamamatsu R9880U-110 photomultiplier. The low gain Rayleigh, nitrogen Raman, water vapour Raman and Mie channels all use a single telescope setup and actuator mounted fibre optic. The two Raman channels rely on the largest telescope and the signals are separated by a dichroic mirror. Specifications for each telescope are found in Table 2.1.

LTA	Mirror Diameter (cm)	Focal Length (mm)	Field of View (mrad)	Parallax (mm)	Optical Filter Width (nm)	Filter Maximum Transmission (%)
High Gain Rayleigh	4X 50	1500	0.27	800	0.3	84
Low Gain Rayleigh	20	600-800	1.7	257	0.3	84
Nitrogen Raman	80	2400	0.6	600	1	~ 50
Water Raman	80	2400	0.6	600	1	~ 50
Aerosol Mie	20	600-800	1.7	257	0.3	84

TABLE 2.1: Specifications for the LTA receiver assembly.

All channels are sampled using a Licel digital transient recorder with a record time of 0.1 μs which corresponds to a vertical resolution of 15 m. The high and low gain Rayleigh channels are electronically gated at 22 km and 12 km, respectively, to avoid damaging the photomultipliers with large signal returns. Further details can be found in (P. Keckhut, A. Hauchecorne, and M. Chanin, 1993) and (S. M. Khaykin, Godin-Beekmann, P. Keckhut, et al., 2017).

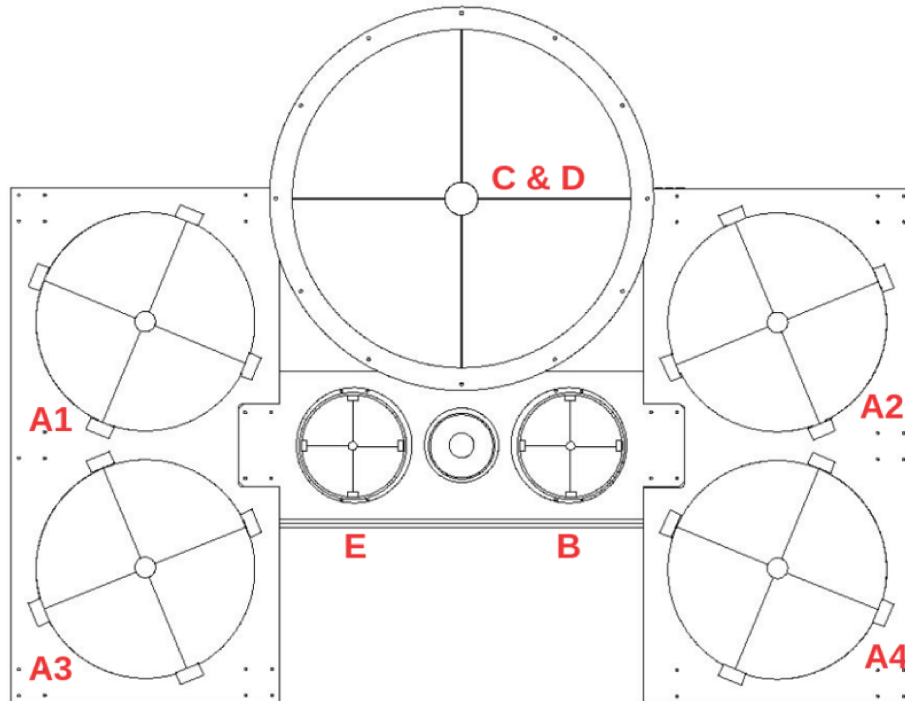


FIGURE 2.1: Mirrors A1, A2, A3, A4 (50 cm) are combined for the high gain Rayleigh channel. B (20 cm) is low gain Rayleigh channel. Mirror C&D (80 cm) is the Raman channel for water vapour and molecular nitrogen. E (20 cm) is the Mie channel. The beam expander for the transmitted laser source is between mirrors E and B.

2.4.2 DIAL Ozone System (LiO3S)

The OHP Differential Absorption Lidar (DIAL), also referred to as Lidar Ozone Stratosphère (LiO₃S), uses two lasers to make a measurement of the vertical ozone profile using the differential absorption by ozone at two different wavelengths. The first laser is an XeCl excimer laser used to produce a 308 nm laser source with a maximum power of 10 W. The beam is passed through a 3X beam expander and has a final divergence of less than 0.1 mrad. The second laser is a tripled Nd:YAG which is used to produce a 355 nm laser source with a maximum power of 2.5 W.

The beam is passed through a 2.5X beam expander and has a final divergence of less than 0.2 mrad. Both transmitted beams have a repetition rate of 50 Hz, and a 7 ns pulse width.

The receiver assembly consists of four 53 cm mirrors each having a focal length of 1500 mm, a field of view of 0.67 mrad, and an average parallax of 310 mm. Each of these four telescopes are focused onto an actuator-mounted 1 mm diameter fibre optic. The outgoing signals are bundled before being passed through a mechanical signal chopper to block low altitude returns below 8 km which would saturate the photon counting electronics. The combined signal is split using a Horiba Jobin Yvon holographic grating with 3600 grooves/mm and a dispersion of 0.3 mm/nm. The light from the grating is projected directly onto the photomultipliers for a high (92%) and low gain (8%) Rayleigh channel at 308 nm, a high gain (92%) and low gain (8%) Rayleigh channel at 355 nm, and two Raman channels at 331.8 nm and 386.7 nm for molecular nitrogen. The spectral resolution of the light incident on the photo cathode is on the order of 1 nm. Figure 2.2 shows a schematic of the OHP DIAL system.

All channels are sampled using a Licel digital transient recorder with a record time of 0.25 μ s which corresponds to a vertical resolution of 75 m. Further details can be found in (Godin-Beekmann, Porteneuve, and Garnier, 2003).

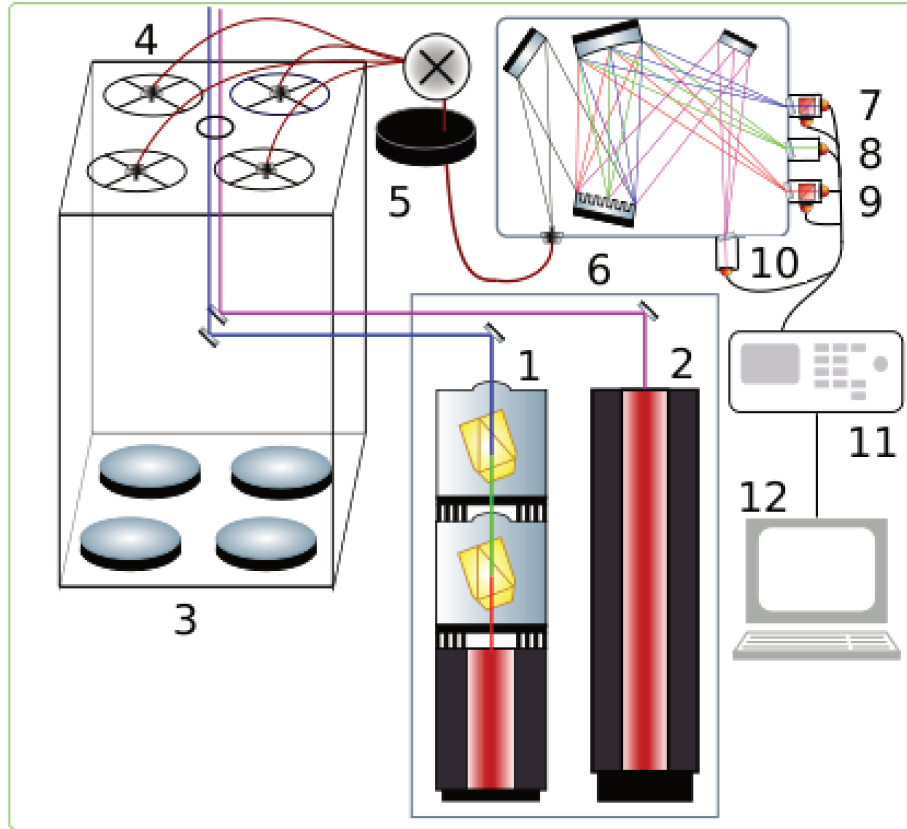


FIGURE 2.2: LiO₃S DIAL system. **1** 355 nm laser source, **2** 308 nm laser source, **3** four 530 mm mirrors, **4** four actuator mounted fibre optic cables, **5** mechanical chopper, **6** Horiba Jobin Yvon holographic grating, **7** 308 nm high and low gain photomultipliers, **8** 331.8 nm photomultiplier, **9** 355 nm high and low gain photomultipliers, **10** 386.7 nm photomultiplier, **11** Licel transient signal recorder, **12** Signal processing and analysis computer.

2.5 Methods

In this section we will set forth rigorous and well defined procedures for the retrieval of lidar temperatures in the middle atmosphere which will minimise the

uncertainties at the upper limit of the lidar altitude range.

2.5.1 Rayleigh Lidar Equation

To calculate absolute temperature profiles from relative density profiles we exploit the gradient of the measured profile of back-scattered photons collected by the receiver. From classical lidar theory (Alain Hauchecorne and M.-L. Chanin, 1980b), we know that the number of photons received is a simple product of transmitted laser power, atmospheric transmission, telescope geometry, and receiver efficiencies. This quantity can be expressed numerically in Eq. (2.1):

$$N(z) = \xi_{sys} \cdot \tau_{emitted}(z, \lambda) \cdot \tau_{return}(z, \lambda) \cdot O(z) \cdot P_{laser} \cdot \frac{\lambda_{laser}}{h \cdot c} \cdot \sigma_{cross} \cdot n(z) \cdot \frac{A}{4\pi z^2} \cdot \Delta t \cdot \Delta z + B \quad (2.1)$$

N is the count rate of returned photons per time integration per altitude bin

z is the altitude above the detector

ξ_{sys} is the system specific receiver efficiency

$\tau_{emitted}(z, \lambda)$ is the transmittance of the photons through the atmosphere

$\tau_{return}(z, \lambda)$ is the return transmittance of the photons through the atmosphere

$O(z)$ is the overlap function of the receiver field of view

P_{laser} is the laser power at a given wavelength

σ_{cross} is the backscattering cross section of the target molecule

$n(z)$ is the number density of scatterers in the atmosphere

$\frac{A}{4\pi z^2}$ is the effective area of the primary telescope

Δt is the temporal integration for data collection

Δz is the spatial range over which photons in a bin are integrated

B is the background count rate.

There are four simple assumptions we make when Eq. (2.1) is used. First, we assume that each photon we count only scatters once. While this is almost certainly not the case, we can say that it is approximately true. Visual wavelength photons have a very low probability of scattering in the atmosphere and with a multiple-scatter process we must square that very small probability. Of these multiply scattered photons, only those with a scatter angle towards the lidar receiver assembly will be seen, with the vast majority scattering outside of the field of view. Further, the tenuous nature of the UMLT means that the small probability of detecting a photon which has scattered more than once becomes exponentially negligible with increasing altitude.

Second, we assume that the atmospheric density is directly proportional to the number of returned photons incident on the receiver assembly. In the case of high signal returns from the lower atmosphere, when the number of returned photons can saturate the photon counting electronics, the measured photon count rate will diverge from the received photon count rate. Multiple detection channels, at different sensitivities, are used to compensate for this effect. In this work we are primarily concerned with the UMLT, a region where lidars operate at very low count rates, so for the purposes of this work we can safely make this assumption. A correction for saturation in the lower stratosphere is described in Sect. 2.5.5.

Third, we assume that the atmosphere is in local hydrostatic equilibrium as well as local thermodynamic equilibrium (LTE) and obeys the ideal gas law. This assumption is potentially problematic at high altitudes where non-LTE processes can affect gravity wave dynamics and temperature profiles (Apruzese, Strobel, and Schoeberl, 1984). However, given that a single lidar profile is acquired every 2.8 minutes and a nightly average temperature is generated every 4 hours, we can have some confidence in this assumption.

Fourth, we assume that the atmosphere at mid-latitudes is generally free of aerosols above 30 km when there are no active volcanic or fire events (Alain Hauchecorne and M.-L. Chanin, 1980b). During less severe background aerosol conditions (aerosol scattering ratio < 1.02), (Gross et al., 1997) suggests lidar temperature cold biases due to Mie scattering are less than 0.5 K at 20 km.

In the UMLT the signal to noise ratio and the model derived a priori assumptions for pressure and density are the main sources of error for the lidar temperature retrieval method. This paper lays out a rigorous method for reducing the noise in

this region of the lidar signal with the goal of producing more robust mesospheric temperatures.

2.5.2 The Raw Counts Lidar Signal

When back-scattered photons are incident on the lidar receiver they are integrated for a set period of time in the counting electronics. This ensures that the recorded signals are based on a similar number of transmitted photons. In the case of LTA a photon count profile, as a function of arrival time, is generated for every 5000 laser shots. Similarly for LiO₃S a photon counts profile is produced for every 8000 laser shots. These measurements can be further integrated for the entire night to increase the signal to noise ratio at the upper limit of the measurement range. We use the speed of light to convert our profiles of photon count rate per second as a function of arrival time at the detector to total photon count rate per second as a function of altitude.

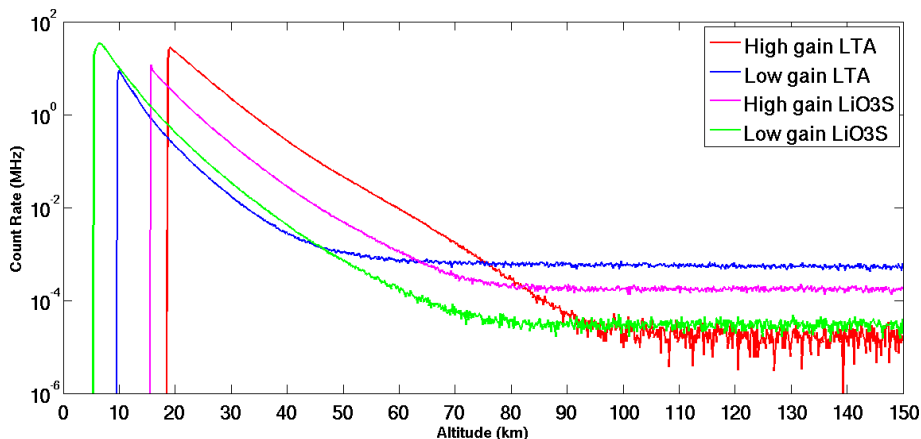


FIGURE 2.3: Nightly integrated profiles for high and low gain Rayleigh signals for LTA and LiO₃S. The background for LTA extends to 246.23 km and for LiO₃S extends to 154.13 km. A single lidar profile for both LTA and LiO₃S has a temporal resolution of roughly 2 minutes and 45 seconds and a vertical resolution of 75 m.

Figure 2.3 shows four nightly integrated OHP lidar count rate profiles as a function of altitude. Both lidar systems employ a high gain and a low gain channel to extend the measurements over a greater altitude range. The lower altitudes (corresponding to the fastest signal return times) of each channel are either blocked by a mechanical chopper or electronically blanked. This is done to avoid saturation of the receiver assembly from very large signals in the lower atmosphere. Additionally, each channel has a set of optics designed to minimise the noise, with greater care being given to the high gain channels. These optics are fully described in the instruments Sect. 2.4.1.

2.5.3 Identifying Outliers, Signal Spikes, Signal Induced Noise, and Transient Electronic Interference

When retrieving lidar temperature profiles in the UMLT it is necessary to take extra precautions to carefully remove outliers, spikes, and electronic contamination from each profile in both the background region and the signal regions. Any contamination of the signal in the background region will be of the same order of magnitude as the true signal and thus, have a disproportionate effect on the temperature. An overestimation of the background due to localised signal contamination will result in the removal of true photons, a lower estimated density, and by the ideal gas law, a higher temperature. The shape of the temperature profile itself will be distorted if there is a non-constant background. If it is not possible to fully correct the issue it is highly recommended to exclude the entire profile from the nightly analysis.

Spikes

Spikes in fast integration photon counting data are not always easy to spot but can be defined as anomalously large, isolated, signal rates which occur in only one altitude bin without affecting adjacent data. If not properly identified and extracted from the data they can contribute to false temperature features and inaccurate background estimations. The spikes can have many potential origins (thermal or electronic imperfection in the photomultiplier, small charges in the Licel digital recorder, interaction of the photocathode substrate with a cosmic ray,

or dozens of different kinds of electronic ‘cross-talk’ between all the instruments at the observatory station) and are therefore impossible, in practical terms, to completely prevent in the lidar data set, and completely impossible to prevent in measurements which have already been made. Therefore, it is necessary to address this problem using software during the analysis. It is particularly challenging to separate small amplitude spikes when the signal to noise ratio approaches 1. It is therefore necessary to establish a consistent criterion to determine which data points belong to the the population of real lidar returns and which points are likely contamination spikes. We have chosen to employ a straight forward Tukey Quartile test (Tukey, 1949) on the difference between consecutively binned lidar returns as this statistic is relatively insensitive to signal drift during the course of the night. The quartile technique is equally useful in both regions of high signal returns as well as the background regions and shows stability and consistency in identifying outliers. Figure 2.4 is a plot of photon count rate as a function of binned arrival time and shows an example of several photon count acquisitions plotted as a stack plot with the black line representing the 2σ limit on the population of lidar returns. Data points above the black line are considered as signal contamination and are removed from the analysis.

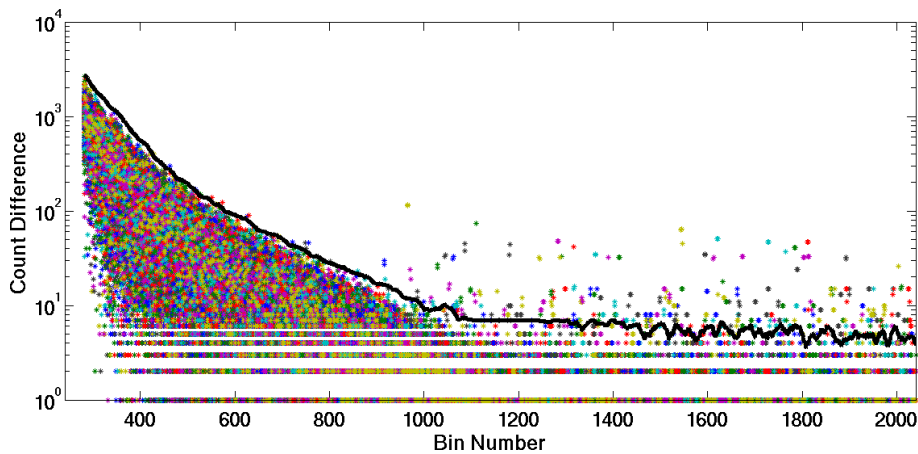


FIGURE 2.4: Tukey Quartile spike identification based on the signal difference between consecutive lidar time bins for short integration lidar returns. An entire night of lidar profiles is over-plotted in the stack plot. The black line is the 2 sigma limit and points above this line are removed.

Transient Electronic Signals

Transient Electronic Signals (TES) are short lived bursts in the lidar acquisition chain and may be internal to the system or related to nearby electronic interference. Possible sources for these transients include photomultiplier ringing from signal saturation, voltage fluctuations in the power supply, ambient RF signals, and ground loops between lidar electronics and Ethernet switches with metal sheathed cables. While these events are rare they can drastically alter the background and resulting temperature profile by inducing wavelike structures into the data.

Unlike simple spikes these features have an amplitude, a duration, and an effect on the counting rate in bins subsequent to the TES burst. In the example shown in Fig. 2.5 is a surface plot of counts differences between consecutive altitude bins for the first 100 altitude bins of lidar data. Each bin is $0.1 \mu\text{s}$ wide. This plot shows profiles for a night of lidar data with each profile accounting for roughly 1.6 minutes of lidar data. We can see that the 22nd and 46th profiles are contaminated by a TES with a duration of about $0.5 \mu\text{s}$. These signals cannot be detected using the Tukey Quartile test as the time derivative of the photon return signal may not be sufficiently far from the nightly population median. However, a 2-D kurtosis test will consistently detect this type of signal contamination as a TES will induce a large skew in the photon count rate population distribution. The kurtosis test is done in the time dimension as well as with altitude to exclude false positives in the photon count rate skew which may be due to clouds or aerosols. Figure 2.5 (bottom) shows a plot of the kurtosis in the population of photon counts in each lidar profile and the red line shows the 2σ estimation of total lidar profile skew. Isolated profiles with a total kurtosis above this limit are excluded.

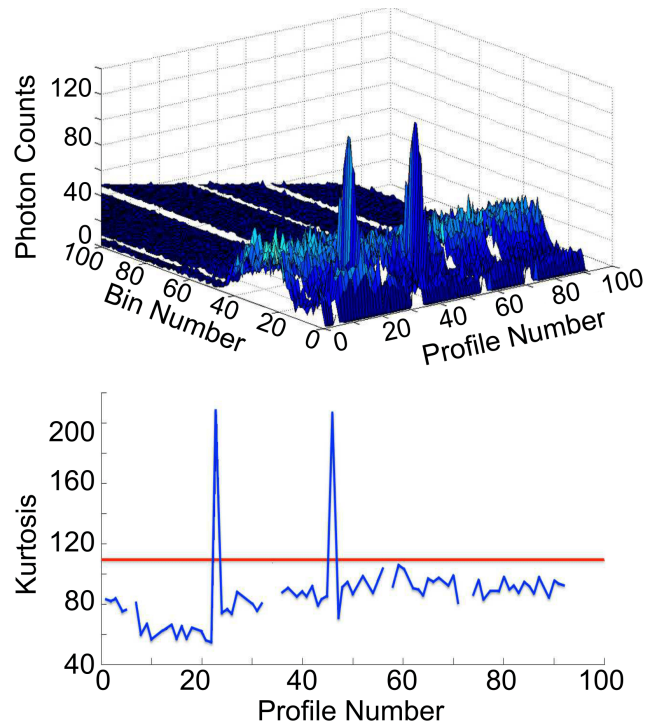


FIGURE 2.5: Upper panel is a surface plot of lidar returns as a function of time bin and profile number. For clarity, only the first 100 bins are shown in this plot. The test is carried out using all bins of each profile. Two instances of TES can be seen as anomalous peaks in the photon count rate. Lower panel is a summation of the fourth statistical moment (kurtosis/skew) for each scan. The red line indicates a 2σ limit on the skew of the population. Points above the limit are excluded.

Bad Profiles

After the removal of lidar profiles which suffer from clear signal contamination, there may still be profiles which ought not be included in a lidar temperature analysis because they are outliers of poor quality compared to other profiles within the same night. Conceptually, ‘bad profiles’ are lidar profiles with a high background and/or a low signal strength as compared to profiles measured shortly before or

after the profile in question. These profiles need to be positively identified as not belonging to the general population of nightly lidar profiles. Quantitatively, identifying a ‘bad profile’ is a challenge as both the background and the signal can change abruptly over the night as the laser power drops or sky conditions change (see Fig. 2.6 for an example). In the top panel of the figure we see the evolution of the background for a night of lidar data. We might suggest that profiles 1 through 23 and profiles 36 through 46 might belong to one population and the rest (excluding profile 69) belong to a second population. However, when we look at the panel representing the signal, it is equally reasonable to, instead, interpret the plot as containing four groups. Each of these groups has similar signals which match fairly well with the changes in the backgrounds shown in the panels above (profiles 1-23, profiles 24-35, profiles 36 - 48 and profiles 49 - 92) . However, whether these four groups of signals should be treated in analysis as two, three, or four distinct populations is open to interpretation. Therefore, we seek an objective programmatic solution for identifying bad profiles. We now show two approaches for attempting to address the issue of changing signal quality.

In Fig. 2.6 the green margin is an attempt to identify ‘bad profiles’ based on a moving average approach however, this method cannot accommodate quick transitions in signal strength and results in false positives when signal quality changes abruptly.

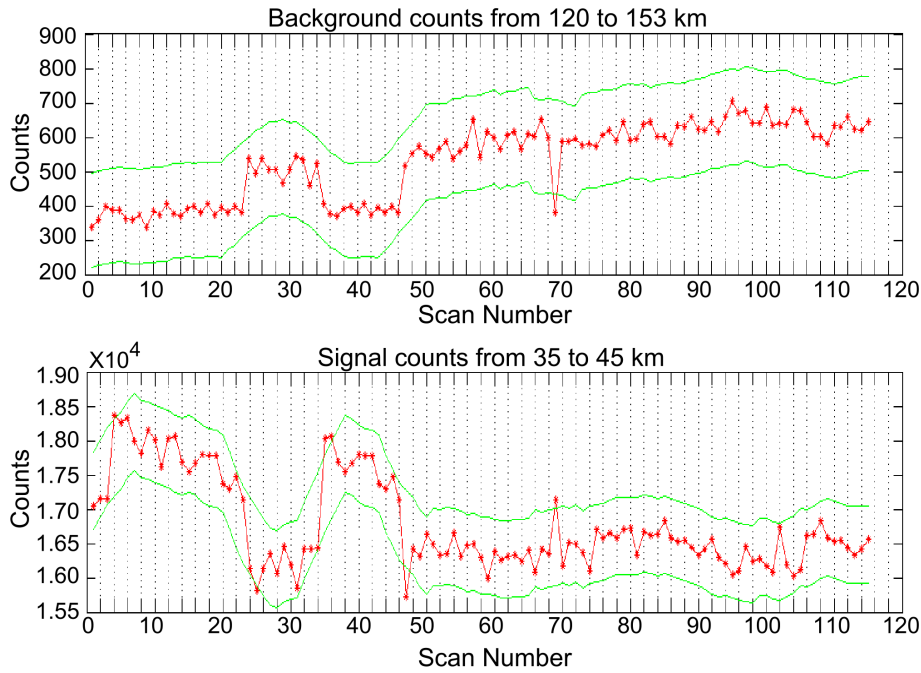


FIGURE 2.6: Example of lidar signal and noise during a night of measurements. Top panel shows the total background counts summed from 120 km to 153 km and the bottom panel shows the total signal summed between 35 km and 40 km. Green bounds are calculated based on a smoothed 2σ error estimation of the summed photon counts.

The simple reality of ground based observation means that lidar signals clearly detect changes in the viewing conditions such as moon-rise, thin cirrus clouds, optically thick clouds, changing light pollution, as well as changes in signal quality. Systematically identifying outlier signals is further complicated as there can be multiple signal to noise population medians during the course of the night. To properly characterise the non-Gaussian distribution of profiles and determine which should be excluded we require a non-parametric statistic. We use a one sided non-parametric Mann-Whitney-Wilcoxon rank-sum test (Mann and Whitney, 1947) to identify lidar profiles which do not belong to the nightly population or sub-populations of lidar profiles.

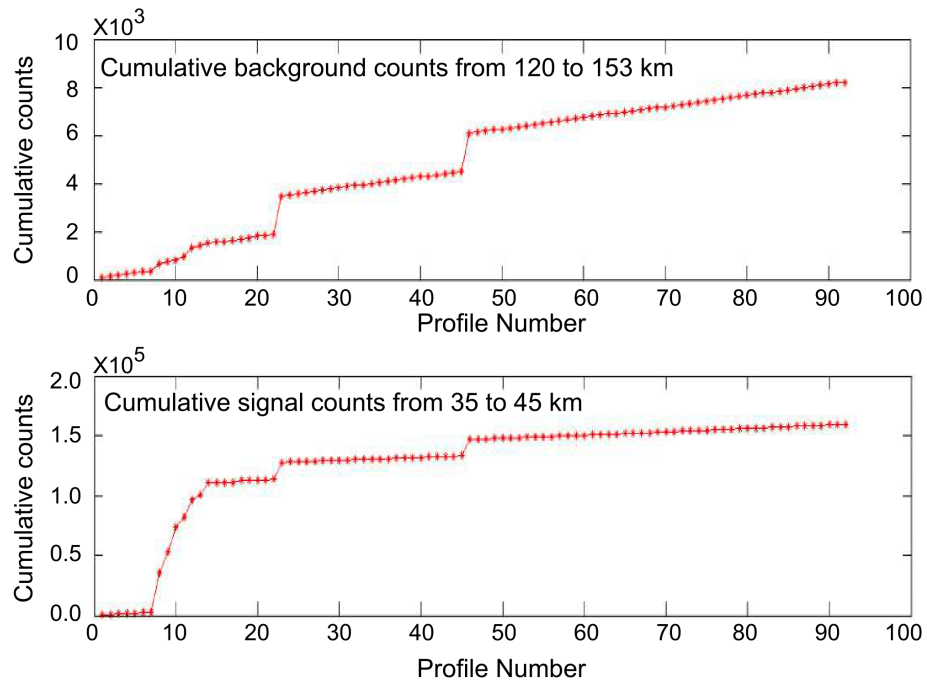


FIGURE 2.7: Rank sum plots for a night of lidar data. Top panel is the cumulative background count and the bottom panel is the cumulative signal count. The signal to noise ratio of the rank summed photon counts in each profile is evaluated using a Mann-Whitney-Wilcoxon rank-sum test to determine if an individual lidar profile belongs to the nightly population of lidar profiles.

Figure 2.7 shows the ranked sum of the background (noise) and signal counts for a night of lidar data. We do not exclude the profiles which fail the test for having high quality. The benefit of using this metric is that it allows us to have a standardised definition of a ‘bad profile’ which takes into account the nightly median without the assumption that the quality of lidar profiles is normally distributed. In this example the first 13 profiles fail the rank-sum test and are discarded.

Good Profiles

Given that our objective is to calculate accurate temperature profiles at the highest possible altitudes we must quality test each profile that we choose to include in the nightly average. It is possible to include partial profiles but that is not done in this work. The conceptual difference between a ‘bad profile’ and a ‘good profile’ is that bad profiles are positively identified as outliers to the general population whereas good profiles represent the portion of the population of profiles which contribute more information than noise to the nightly average at a given altitude. Consider that a poor quality lidar profile which has a signal to noise ratio of 1 at 70 km contributes more information from the signal than from the (background + noise) at 60 km, but less information from the signal than from the (background + noise) at 80 km. Thus, we need a flexible metric to determine signal quality over a diagnostic altitude which reflects the general signal quality of the night.

Quantitatively, we express this with a signal, S , to noise, N , inequality in Eq. (2.2). The background (noise) of an individual profile, N_i , is expressed as the summation of photon counts in bins which fall between 120 km and 155 km and the nightly background, N_{sum} is the summation of all N_i for the night. To determine a metric for the nightly average lidar signal, S_{sum} , we first calculate a quick density profile and determine the lowest altitude where the signal to noise ratio equals 1. We chose a cutoff value of SNR=1 because it is the least strict value we could use which ensures that we have more information than noise (or, specifically, more information than noise plus background counts), at the altitude within the density profile where we begin the downward temperature integration. Had we chosen a criterion which was less strict (SNR \ll 1), we would expect to see more statistical variability in the top altitudes of the temperature retrieval as a result of starting the temperature integration in a region which contains more noise than signal. Conversely, choosing a criterion which is too strict (SNR \gg 1) limits the maximum altitude of the temperature retrieval as discussed in Sect. 2.5.6. The SNR = 1 point forms the upper bound of the altitude range from which we derive the representative signal for the profile. The lower bound of this representative signal range is defined to be one density scale height (\sim 8 km) below the upper bound. The lidar range bins which correspond to this altitude range are then summed to yield S_{sum} . A similar calculation, using the same range bins as in the nightly average calculation, is done to determine the signal of a single profile, S_i . If a

profile fails the inequality test then it is not included in further nightly analysis.

$$\sqrt{\frac{S_{sum} + N_{sum}}{S_{sum}}} < \sqrt{\frac{(S_{sum} - S_i) + (N_{sum} - N_i)}{S_{sum} - S_i}} \quad (2.2)$$

2.5.4 Noise Reduction

Statistical uncertainty in photon counting can be described by a Poisson distribution based on the square root of the number of photons received. Systematic uncertainties in the photon counts are introduced by ambient background light (light pollution, moonlight etc.), thermal excitation in the photomultipliers (so-called dark current), and signal induced noise. The first two sources of error are minimised by using narrow filters in the optical receiver chain and by cooling the photomultipliers. The signal induced noise can be very difficult to correct experimentally and is usually estimated in data processing. This type of noise can occur if the photomultipliers have become saturated at any point in the signal acquisition process and often manifest as non-linear artefacts superimposed upon the true photon count profile.

Figure 2.8 shows the reduction in the background noise due to recent hardware improvements. The first drop corresponds improvements made to the photomultiplier cooling system which reduces the number of thermally excited electrons detected at the photo cathode of the photomultiplier in the absence of signal from the sky. The second drop in background counts results from replacing the Hamamatsu R7600U-20 multi-alkali photomultiplier with the improved Hamamatsu R9880U-110 photomultiplier having a super bi-alkali photo-cathode. The third and final drop in background counts is a result of replacing a 532 nm optical filter which has a width of 1 nm with a newer filter having a bandwidth of 0.3 nm. These experimental modifications result in a 100 fold decrease in the background noise and allows us greater confidence in our UMLT temperature retrievals. The regular monthly variations in the signal which become apparent at lower noise levels are due to the phase of the moon.

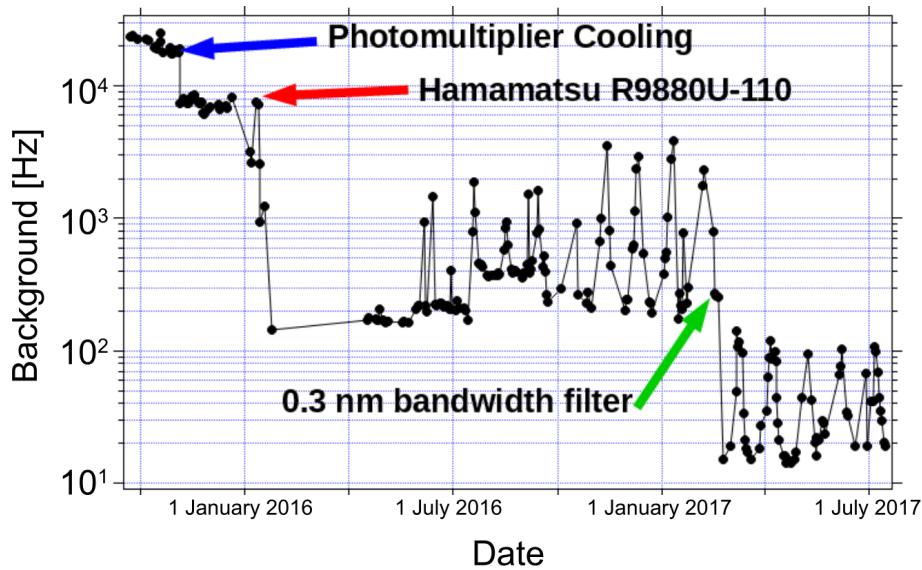


FIGURE 2.8: This figure shows the improvements in the background count rate due to photomultiplier cooling, new photomultiplier, and new optical filters. Note the logarithmic y-axis and the total reduction of background counts by more than 2 orders of magnitude.

2.5.5 Corrections Applied Before Temperature Calculation

In the previous subsection we detailed the process for removing bad data points and profiles from our nightly lidar measurement. In this subsection we will detail several corrections to our remaining photon count profiles which correct for signal saturation, atmospheric transmission, and background estimation.

Deadtime Correction

The OHP lidars measure photons using photomultipliers and a digitising signal counter. This system is highly efficient at detecting low signals and is optimised for single photon returns in the UMLT. However, given that the returned lidar signal directly follows the exponential density of the atmosphere, the photomultipliers

and counting systems are susceptible to missing photons at lower altitudes due to high count rates. To correct for this saturation effect we can estimate a correction coefficient, τ , also referred to as a deadtime.

The background theory and derivation of Eq. (2.3) is well described by (Donovan, Whiteway, and Carswell, 1993), where $N_{received}$ is the number of photons incident on the PMT per measurement time interval and $N_{counted}$ is the number of photons per measurement time interval which are actually counted by the system. In general, $N_{counted} < N_{received}$ due to effects of the system deadtime. This deadtime correction can be calculated based on factory specification of the counting electronics, a theoretically derived deadtime, or it can be measured directly using a low gain lidar channel. The OHP lidars measure the deadtime directly and correct for saturation in the high gain channels with information from the low gain channels. If the low gain channel is not available a theoretical correction of 7 ns is applied to pre-2013 data and 4 ns is applied to more recent data following the installation of a Licel digital recorder.

In order to measure the deadtime experimentally, we assume that the low gain channel, because it has low photon count rates, will always operate in the linear response regime and will never suffer from deadtime effects. Thus, it represents a value proportional to the ‘true’ rate for returned photons for each altitude. Once scaled by a constant (e.g. using MSIS or another model), we can use this count rate as $N_{received}$.

The high gain channel, conversely, measures higher photon count rates at every altitude than the low gain channel does. Similarly to the low gain channel, at the low end of its dynamic range, the high gain channel operates linearly, and therefore represents a value proportional to the ‘true’ rate for returned photons for each altitude. The constant of proportionality is different for low and high gain channels. At low count rates, the scaled counts measured by the high gain and low gain channels are equal. As photon count rates move into the higher end of the high gain channel’s dynamic range, deadtime begins to have an effect: The high gain channel will measure too few photons compared to the ‘true’ rate; the number of photons which are returned to the lidar. Therefore, we call the scaled high gain count rate $N_{uncorrected}$ in Eq. (2.3); it has not yet been dead time corrected. We will refer to the deadtime corrected scaled high gain count rate as N_{dte} . Equation (2.3) is used several times. First, we use data only from altitudes

for which the low gain and high gain channels both have measurements (nominally 40 to 60 km). We iterate through various values of τ , calculating a N_{dtc} for each $N_{uncorrected}$ value. This is carried out until the difference between $N_{corrected}$ (from the high gain channel) and $N_{received}$ (from the low gain channel) is minimised. This determines the dead time of the system, τ . Next, Eq. (2.3) is used again, using the measured nightly value for τ , to calculate N_{dtc} for all $N_{uncorrected}$ high gain channel measurements. This allows us to correct the high gain measurements for the entire profile.

$$N_{dtc} = N_{uncorrected} * \exp\left(\frac{\tau * N_{uncorrected}}{\Delta t}\right) \quad (2.3)$$

Atmospheric Transmission Correction

To correct for Rayleigh and ozone extinction we use MSIS-90 model (Picone et al., 2002) to generate a vertical profile of ozone, molecular oxygen, oxygen radical, molecular nitrogen, and argon, and then apply the correct Rayleigh cross-section to each species. This method is adapted from (Argall, 2007) and is important for accurate retrievals of density and neutral temperature in the UMLT. Correction for aerosols is not done in this work as we assume that the atmosphere is generally clean above 30 km (Alain Hauchecorne and M.-L. Chanin, 1980b).

Defining the Background

Normally, we assume that the rate of counted photons per laser shot is constant in the background region during the signal acquisition time and can therefore be approximated by a simple Poisson distribution. We further assume that in this background region we are not measuring returned photons from the laser signal but instead are measuring ambient sky light. However, if there is non-linear signal induced noise in the photon counting chain, the number of counted photons is not constant with time during the acquisition period of a single laser shot. When this occurs we cannot assume that the variation in the background is a strictly Poisson distribution around a constant expected value.

If left uncorrected, we risk overestimating the number of ‘true’ photons returned from the upper atmosphere and the result is an artificially dense and cold UMLT. Erring on the side of caution we fit three backgrounds (constant, linear, and quadratic) to each nightly summed profile, in a standard diagnostic region, and choose the function with the best Chi-squared goodness of fit as our estimate of signal induced noise. The best background function is subtracted from the raw photon counts profile. Shown in Fig. 2.9 is an example of a night where the low gain Rayleigh channel (blue) experienced signal induced noise which was best approximated by a quadratic function; the high gain Rayleigh channel (red) had a background best estimated by a small negative linear function; and the nitrogen Raman channel (green) had no apparent signal induced noise and was fit with a constant background. The optimal solution for non-linear signal induced noise is to determine the contribution of both the signal and the noise using exponential fits however, we have found that method to be extremely sensitive to the choice of background diagnostic region and was less stable than the simple quadratic approximation.

We have some confidence that the quadratic background correction to the low gain channel correctly approximates the moderate non-linear signal induced error because we can compare the corrected low gain channels to the high gain channel. In the overlap region we have two channels making coincident measurements and we can safely assume that the response rate for the high gain channel is linear. Therefore, a correction for signal induced noise in the low gain channel which brings the resulting low gain count rates into the closest agreement with the high gain channel count rates at the same altitudes will be the optimal choice for the correction. In some cases, the quadratic correction for signal induced noise in the low gain channel yields better agreement than the constant or linear corrections, in which case it is employed. The best individual choice (constant, linear, quadratic) is used for each profile. We believe these empirical corrections to be sufficient, because (a) the resulting agreement with the high gain channel improves as compared to the uncorrected profile, (b) the resulting corrected low gain count profiles are generally equal to the high gain count profiles to within statistical uncertainty, and (c) for the few cases in which the empirical correction ultimately fails, this will be apparent by the corrected signal retaining poor SNR values. The melding procedures of Section 3.6 weight the combined high and low gain Rayleigh channels according to SNR, and so in these cases, the poorly-corrected low gain contributions to the

final melded counts profile will be negligible, and all information will be obtained from the high gain channel.

For the quadratic case, as soon as there is signal induced noise the profiles no longer represent Poisson distributions as the count rate in each lidar bin is no longer fully independent of the count rates in the bins on either side of it. Therefore, precise calculations of the SNR would require the addition in quadrature of real noise (from sky background and signal photon counts) and contamination noise (from signal induced noise). Here, however, we make the assumption that the signal induced noise is able to be completely removed from the raw profiles with the subtraction of the quadratic function. We therefore interpret the background subtracted profiles to obey approximately Poisson distributions, thereby approximating the total noise in the profile to the noise of only the real photons, which can be treated as uncorrelated. Our standard altitude range for background selection is 120 km to 155 km but this number is system and channel specific. To illustrate this point we compare the background regions of the high gain Rayleigh channel (red) and the nitrogen Raman channel (green) in Fig. 2.9. The nitrogen Raman channel background could be calculated from 50 to 155 km or 120 to 155 km and yield the same result.

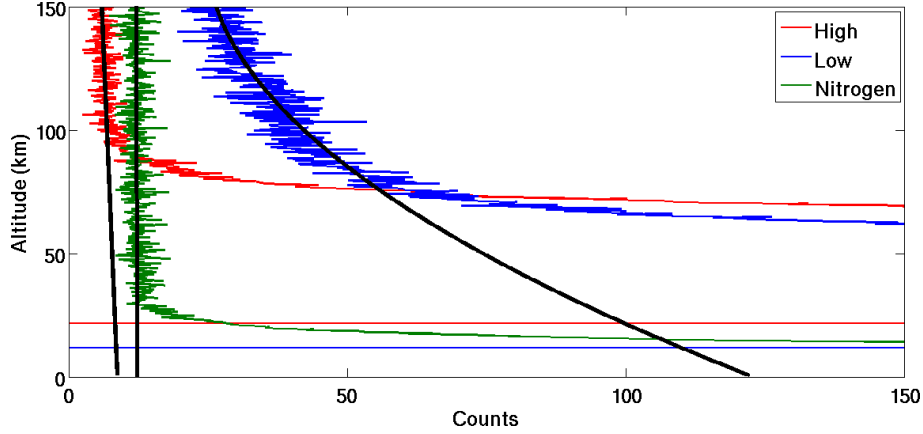


FIGURE 2.9: An example of non-linear signal induced noise in the low gain Rayleigh channel best estimated by a quadratic background. Also shown is the high gain Rayleigh channel (red) with a background best fit by a negative linear function and the nitrogen Raman channel (green) with no apparent signal induced noise and a constant background.

2.5.6 Temperature Inversion Equation

The standard NDACC algorithm for Rayleigh temperature retrieval is the Hauchecorne-Chanin (HC) method (Alain Hauchecorne and M.-L. Chanin, 1980b) which makes a scalar normalisation of the photon-count profile to an in-situ density measurement or to a density calculated from a model like CIRA-72, SPARC-80, or MSIS-90. From a density gradient profile we calculate a pressure gradient profile Eq. (2.4) and using the ideal gas law, Eq. (2.5), we can arrive at an expression for pressure, Eq. (2.6). Here P is pressure, z is altitude above the lidar station, ρ is density, g is the latitude dependent acceleration due to gravity for an ellipsoid Earth given by the Somigliana formula, R is the ideal gas constant, T is the temperature, and M is the molecular mass.

$$dP(z) = -\rho(z)g(z)dz \quad (2.4)$$

$$P(z) = \frac{R\rho(z)T(z)}{M} \quad (2.5)$$

$$\frac{dP(z)}{P(z)} = -\frac{Mg(z)}{RT(z)}dz = d(\log(P(z))) \quad (2.6)$$

The crux of the challenge for initialising the lidar equation lies in the non-linear nature of Eq. (2.6) which will necessitate the introduction of an a priori estimate of pressure at the top of the atmosphere followed by an iterative approach to retrieving the profile at lower altitudes. A full theoretical description of this problem was well laid out by (J. Khanna et al., 2012). In this work we have chosen to take our initial a priori seed pressure value, $P(z_1)$, from the MSIS-90 model. We now arrive at an iterative expression for the generation of the pressure profile as a function of altitude Eq. (2.7).

$$\frac{P(z_i) - \frac{\Delta z}{2}}{P(z_i) + \frac{\Delta z}{2}} = \exp \frac{Mg(z_i)}{RT(z_i)} \Delta z \quad (2.7)$$

Given our iteratively generated pressure profile we can do an inverse calculation to map our pressures to a set of temperatures using Eq. (2.8) and Eq. (2.9). This iteration starts at the top of the atmosphere, in a region of low signal to noise and thus of large relative uncertainty, and proceeds downwards in altitude and becomes exponentially less uncertain with each step as signal quality improves with increasing atmospheric pressure. As we iterate downward the influence of our choice of a priori pressure becomes less significant and the calculated temperature profile becomes entirely data driven.

$$X_i = \frac{\rho(z_i)g(z_i)\Delta z}{P(z_i) + \frac{\Delta z}{2}} \quad (2.8)$$

$$T(z_i) = \frac{Mg(z_i)}{R \log(1 + X_i)} \Delta z \quad (2.9)$$

In order to calculate a single temperature profile from 5 km to above 80 km we meld the photon counts from the high and low gain Rayleigh channels together with the counts from the N_2 Raman channel. The slope of the logarithm of each of the three photon counts profiles is compared to a synthetic lidar counts profile generated based on the nightly average MSIS-90 density profile. The comparison gives us a first estimation of the linearity and alignment of the lidar data. We then select a clear linear region of each profile to use in calculating a MSIS derived scaling factor for each profile. This procedure allows the top of the nitrogen Raman profile to be melded to the bottom of the low gain Rayleigh profile and the top of the low gain Rayleigh profile to be melded to the bottom of the high gain Rayleigh profile. The melding calculation is conducted over a signal-to-noise defined altitude range and is a straightforward weighted average. The resulting melded density and pressure profiles are used to generate a single nightly average temperature profile like the one shown in Fig. 2.10. The use of MSIS-90 as a scalar density reference for the synthetic lidar profile does not affect the final lidar temperature profile which depends only on the relative density and not the absolute value. We follow similar procedures to those described by (Alpers et al., 2004).

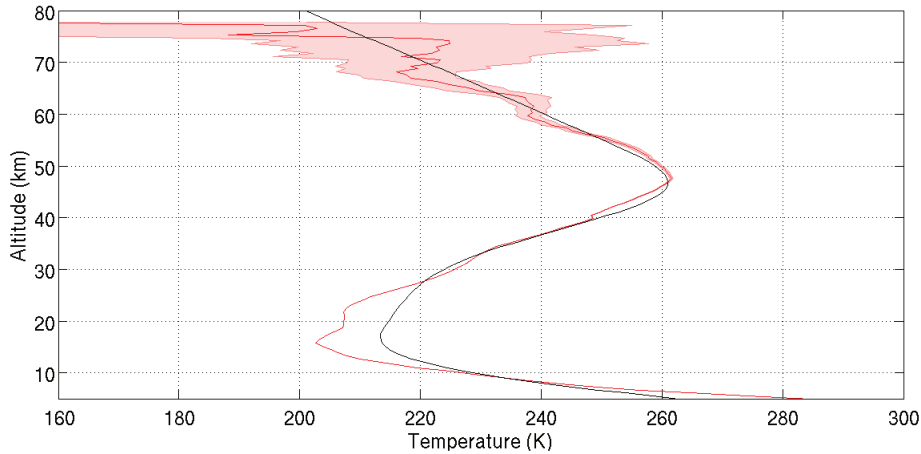


FIGURE 2.10: An example of a nightly average melded temperature profile from two Rayleigh channels and one Raman channel. The profile is calculated at 300 m vertical resolution from a single combined photon count profile and has a maximum relative error near 80 km of 30%. Black line is the MSIS-90 temperature profile which corresponds to the MSIS-90 pressure and density information we used as an a priori.

Where to start the inversion

As can be seen in Eq. (2.8) and Eq. (2.9) the calculation of lidar temperature requires an a priori guess of pressure at the top of the atmosphere and a relative density gradient. Given that the signal to noise in the UMLT can be very low, the choice of a priori as well as the uncertainties in the density gradient can have a very large effect on the temperature profile (J. Khanna, R. J. Sica, and McElroy, 2011). As a result, it is prudent to remove the top 15 km of the retrieval to minimise the contribution of the a priori (T. Leblanc, McDermid, Philippe Keckhut, et al., 1998).

In our treatment the a priori pressure is selected at the altitude where the signal to noise ratio in a smoothed photon counts profile is 1. The resulting temperature profile is subsequently cut when the relative error exceeds 30 percent. This treatment is not the optimal solution for the retrieval altitude as a fully Bayesian algorithm is required to properly characterise the influence of the a priori choice

(R. Sica and Haefele, 2015). However, we believe that our signal to noise metric is sufficiently rigorous, and more importantly reproducible.

2.6 Net result of temperature algorithm modifications

The NDACC algorithm contains such corrections as deadtime, background, and transmission. The new algorithm improves upon the background correction and identification of bad profiles, and introduces corrections for: signal spikes, TES, identification of good profiles, and noise reduction, all which have not previously been addressed by the NDACC algorithm.

The LTA data is recorded and saved at 75 m resolution. The spike and TES corrections described in sect.2.5.3 and 2.5.3 are carried out at this resolution. Then the profiles are integrated to 300 m, at which point the remainder of the corrections in Section 3 are applied.

Temperature profiles using the new algorithm are calculated at 300 m resolution for LTA, and are plotted as the green line in Fig. 2.11. This is higher resolution than the standard NDACC temperature resolution, which is 1 km, smoothed to 2 km effective vertical resolution. The LTA NDACC-calculated temperatures (black line in Fig. 2.11) are plotted at 2 km effective resolution. By implementing the new algorithm, we have cooled the UMLT lidar temperature retrievals with respect to the standard NDACC temperature algorithm. The modifications cool the mesospheric retrievals by approximately 5 K near 85 km and 20 K by 90 km. There is no significant difference between the new and the NDACC algorithms for LTA below 70 km.

Temperature profiles calculated for LiO₃S are all carried out using the NDACC algorithm at an effective vertical resolution of 2 km, and these are shown as the orange line in Fig. 2.11. Whereas the LTA NDACC algorithm results are warmer than the LiO₃S NDACC algorithm results above 70 km, we now see that the LTA new algorithm results are cooled sufficiently that they more closely match the LiO₃S measurements up to 78 km. Therefore the corrections for LTA proposed

in the new algorithm represent a significant improvement over the LTA NDACC algorithm for altitudes above 70 km.

A comparison with temperature retrievals from the satellites MLS (red line in Fig. 2.11) and SABER (blue with shaded ensemble variance), and with the MSIS-90 model (magenta line in Fig. 2.11), also shows an improvement in the LTA temperatures retrieved using the new algorithm as compared to the LTA NDACC algorithm. By implementing the techniques described in the sections above we can account for nearly half of the temperature difference between the lidar and the satellites at 90 km. The character change in the difference functions above and below 84 km is in part due to the increasing contributions of the species specific Rayleigh back-scattering correction and the corrections to the gravity vector. The remaining temperature difference between the improved lidar temperatures (green) and the satellites and model may be in part due to distortions in the satellite a priori for the geopotential vector. This possibility is explored further in the companion paper, and all coincidence criteria for the satellite comparisons are available therein (R. Wing, A. Hauchecorne, P. Keckhut, Godin-Beekmann, S. Khaykin, and McCullough, 2018b).

It is important to note that additional complications exist when comparing temperatures derived from ground based lidars to temperatures derived from satellite data which have their own calibration concerns. We explore the issues of lidar-satellite comparison in part B of this paper (R. Wing, A. Hauchecorne, P. Keckhut, Godin-Beekmann, S. Khaykin, and McCullough, 2018b). A co-located ground-based resonance Doppler or Boltzmann lidar would provide a better comparison data set as resonance lidars have high signal to noise ratios above 75 km (Alpers et al., 2004).

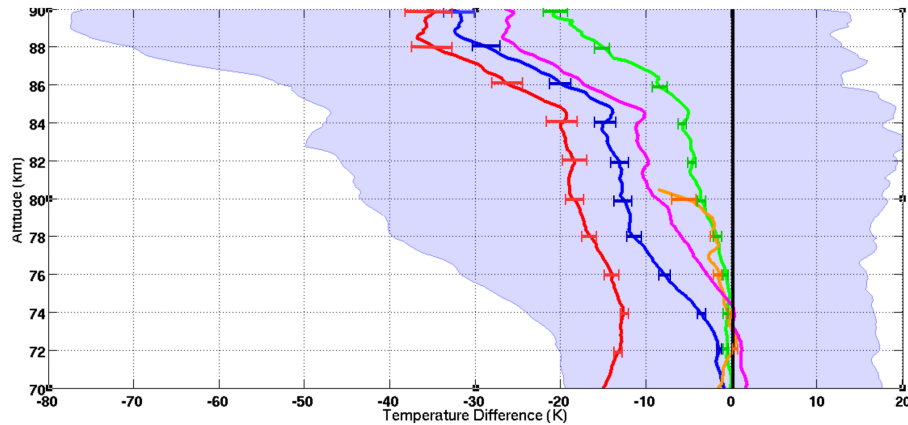


FIGURE 2.11: Ensemble temperature differences from NDACC standard LTA Rayleigh temperatures (black). MLS (red), SABER (blue with shaded ensemble variance), MSIS-90 (magenta), LiO₃S (orange), and LTA Rayleigh temperatures with corrections given in this work (green).

2.7 20 Year Comparison of OHP Lidar Temperatures

Conducting systematic inter-comparisons between independent lidar systems is essential for assuring data quality and is a requirement for NDACC certified instruments. Most comparisons are conducted on a campaign basis where two or more lidar systems are co-located and make coincident measurements. A good example of this type of work was the stratospheric lidar and Upper Atmospheric Research Satellite (UARS) validation campaign (Singh et al., 1996a). The present study proposes a completely novel type of inter-lidar study on the long term stability of the Rayleigh lidar technique. The first step in our analysis is to compare the temperature profiles from the LTA and LiO₃S systems. LTA temperatures were calculated using the OHP NDACC temperature code and LiO₃S temperatures were calculated using a modified version of the same code. There are very few significant differences between these two codes. The most important difference involves the choice of parameters for melding the high and low gain channels for

the two systems. Given the differences in the relative gain between the four lidar channels being considered, the melding of LiO₃S often occurs at a lower altitude than LTA. The present study considers temperatures between 35 km and 75 km to ensure that we are well above any contamination from aerosols and below any significant initialization errors. From Fig. 2.11 we can see that there is no significant difference in the temperature outputs of these two algorithms (black baseline and orange) or with the improved algorithm (green) below 75 km.

We selected the data from 1993 to 2013 for the comparison as both instruments operated regularly and without significant design changes during this time. Since the lidars are co-located and are operated by the same technicians they often make measurements simultaneously. Figure 2.12 shows the average number of measurements per month made by the LTA and LiO₃S which were included in this study as well as the average number of common measurements per month. We defined common measurement times based on more than 80% temporal overlap, good quality profiles in both systems, and good internal alignment of both lidars. Of the 2482 nights of LTA data and 3194 nights of LiO₃S, 1496 nights met our criteria for coincidence.

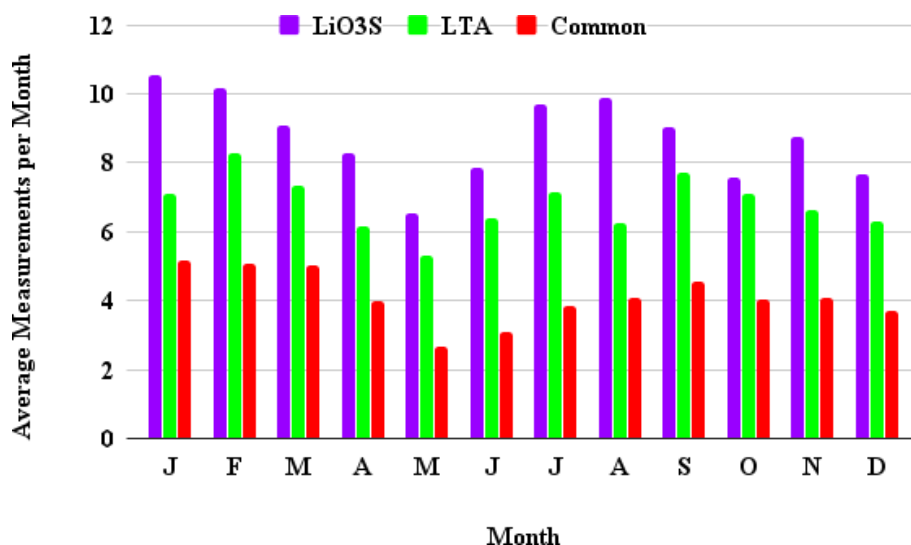


FIGURE 2.12: Average number of OHP lidar temperature measurements per month during the period of 1993-2013.

Figure 2.13 shows the nightly temperature differences between the two lidar systems. The 20 year data set contains 1496 coincident measurements lasting longer than four hours. Black vertical rectangles indicate some of the time periods where the high or low gain channels were misaligned in one or the other lidar. Internal misalignments happen when one or more of the five mirrors in LTA or four mirrors in LiO₃S are not properly aligned with the laser or the fibre optic is not centred on the focal point of the mirror. A few of these time periods can be associated with minor system modifications. Misaligned lidar signals were identified by comparing the slopes of the density profiles in the high (generally above 50 km) and low (below ~50 km) gain channels of each system. A simple chi-squared test was used to detect these nights and exclude them from the rest of the analysis. It is possible that the criteria described above for identifying periods of misalignment is not yet stringent enough. Therefore, one limitation of the OHP measurements in terms of accuracy, and depending on time scale, also precision, is the influence of periods of misalignment that have not been programmatically identified. An ideal solution would be to have an independent method of monitoring mirror alignment during atmospheric measurements (e.g. installation of a small sighting telescope to measure the alignment coupled with an automatic fibre optic alignment system). With the existing data set from OHP extending back two decades, we unfortunately cannot retrospectively address such a hardware goal, but there may be opportunities in future to look into the effects of choosing different criteria to identify periods of misalignment.

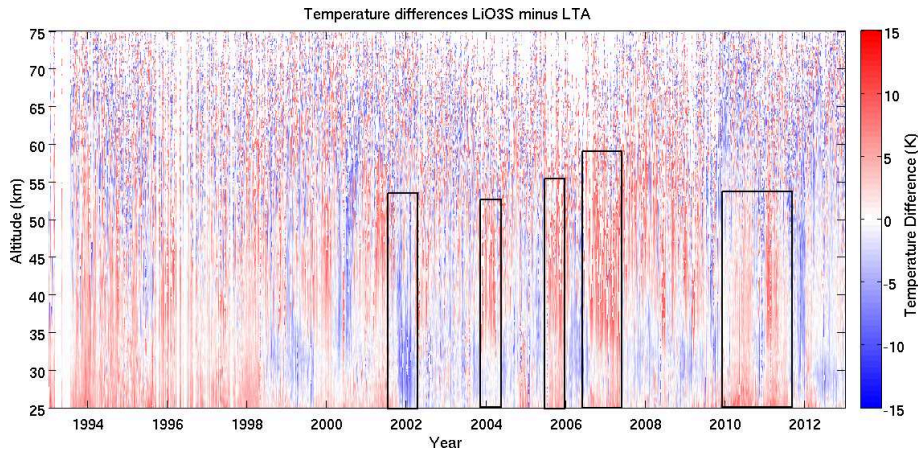


FIGURE 2.13: Temperature differences between LTA and LiO₃S OHP lidars for a 20 year period between 1993 and 2013. There are 1496 nights of comparison in this plot. Red indicates that LiO₃S was warmer than LTA and blue that it was colder. The black boxes highlight periods where the two lidars were out of alignment with respect to each other.

Figure 2.14 shows four curves depicting the average temperature differences as a function of altitude and year. The red curve is the average temperature difference between 65 km and 75 km with an average standard deviation of 6.6 K; the green curve is the average temperature difference between 55 km and 65 km with an average standard deviation of 4.5 K; the blue curve is the average temperature difference between 45 km and 55 km with an average standard deviation of 2.7 K; and the magenta curve is the average temperature difference between 35 km and 45 km with an average standard deviation of 1.6 K. A 30 day averaging window is applied to each of the four curves.

For reference, a typical LTA temperature profile with an effective vertical resolution of 2 km has an uncertainty due to statistical error of 0.2 K at 40 km; 0.4 K at 50 km; 0.6 K at 60 km; 0.7 K at 70 km; 1.8 K at 80 km; and 6 K at 90 km. For reference, a typical LiO₃S temperature profile with an effective vertical resolution of 2 km has an uncertainty due to statistical error of 0.3 K at 40 km; 0.5 K at 50 km; 1.0 K at 60 km; 2.7 K at 70 km; and 10 K at 80 km.

Examining the time evolution of the average temperature differences between LTA and LiO₃S at four altitude levels gives us confidence that both measurements are stable in both time and altitude. Using all data, including misaligned periods (example: winter 2006-2007 in Fig. 2.13 and Fig. 2.14) none of the lidar temperature differences are significant at the 2-sigma level, although certain periods do have temperature differences which are detectable at the 1-sigma level. This can be seen where the blue shaded region (2005 - 2008) and the magenta shaded region (in 2007) are entirely above the zero line. If the misaligned periods are disregarded, no temperature differences are significant, even at the 1-sigma level. Therefore, we conclude that the results from the lidars, when well-aligned, are stable in time, over the 20-year period studied.

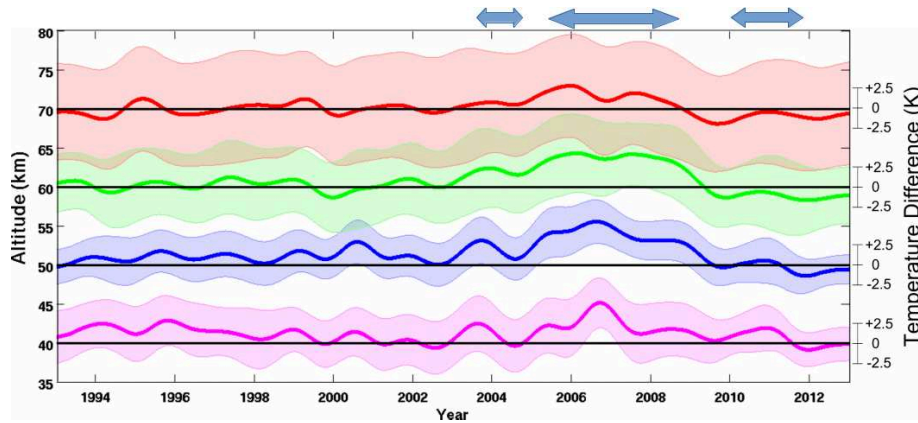


FIGURE 2.14: Average temperature differences between LTA and LiO₃S OHP lidars for a 20 year period between 1993 and 2013 at four altitude levels: 65-75 km (red), 55-65 km (green), 45-55 km (blue), and 35-45 km (magenta). Shaded uncertainties are shown at 1 sigma for clarity and the black lines are zero temperature difference displaced to 40, 50, 60 and 70 km. All measurements, including periods of lidar misalignment, are included in this plot. The apparent anomalies (blue arrows) occur only during times where the lidars were often misaligned, as indicated in Fig. 2.13.

After removing comparisons between misaligned instruments we can calculate the ensemble median difference between the two systems. The ensemble median difference in Fig. 2.15 shows very good agreement between the two co-located lidar

instruments. The temperatures produced by LTA and LiO₃S are statistically equal above 45 km for the 20 year period between 1993 and 2013. There is a small -0.6 K systematic difference which reaches a maximum near 40 km. We believe this slight cold bias is due to small differences in the signal melding technique between the high and low gain channels in both systems. On a typical night, the LTA low gain channel starts to significantly contribute to the combined signal near 50 km. If the photon count rate in the low gain channel is too large at these altitudes (due to residual noise contributions or from a slight misalignment with the high channel) the counts will be artificially higher than expected, resulting in a lower temperature. The converse holds true when the low gain channel is misaligned in the opposite sense, resulting in a slight warming due to underestimation of the counts.

The effect of these small temperature perturbations is so small that they can't be seen in single nightly temperature comparisons and were not detected before this study. It is important to note that the 2σ distribution about our ensemble at 40 km has a magnitude of approximately 0.45 K while the statistical error for a single night of lidar measurements near 40 km at 300 m vertical resolution can be on the order of 2 K. Detecting and resolving this small disagreement will be extremely challenging and will not be accomplished in this work.

Given that the primary interest of this work is the upper middle atmosphere (nominally above 50 km), we will focus on the upper portions of Fig. 2.15 where the two lidars are in statistically perfect agreement. To our knowledge, this is the first ever long term study of the temperatures produced by co-located temperature lidars operating at 532 nm and 355 nm. The excellent agreement between these two independent measurements gives us confidence that A) there is no vertical misalignment between the lidars, B) there are no unaccounted for optical transmission effects which influence our temperatures, C) the lidar measurements are reasonable and reproducible, D) we can now proceed with some confidence that our ground based lidar measurements can be useful as a calibration source for the space based satellite measurements.

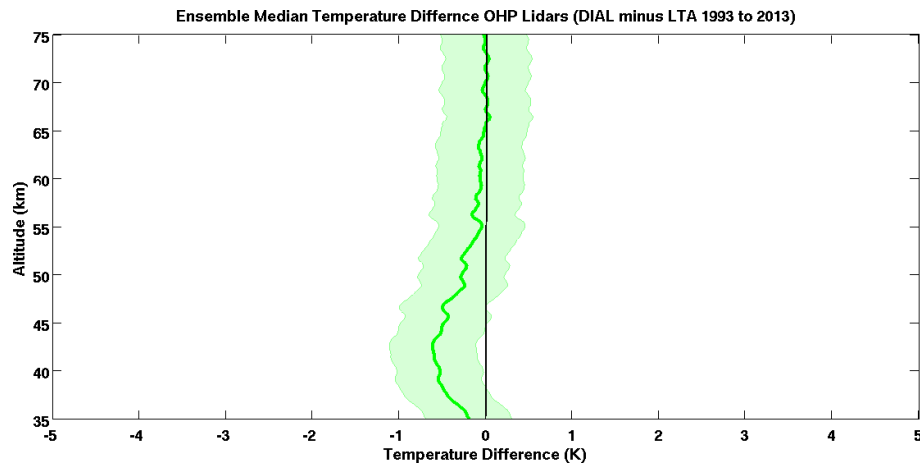


FIGURE 2.15: Ensemble of median temperature differences between LTA and LiO₃S based on temperature measurements between 1993 and 2013. Shaded error is the two sigma distribution about the ensemble.

2.8 Conclusions

2.8.1 Changes to Lidar Temperature Algorithm

In this work we have attempted to minimise the systematic temperature bias at the top of the lidar temperature retrieval which has been noted previously by several studies cited in the introduction. We have done this by clearly and carefully outlining a rigorous, and complete algorithm for the calculation of lidar temperatures in the UMLT. We have presented techniques for the detection of signal contamination, the selection of the best data for inclusion in the calculation, criteria for where to initialise the inversion when assuming an a priori pressure at the top of the atmosphere, and have demonstrated the benefit of photomultiplier cooling and narrow band pass filters to reduce lidar backgrounds.

After applying our techniques we have seen a reduction in the calculated values of the high altitude lidar temperatures which brings them into better agreement with the temperatures measured by both MLS and SABER (Fig. 2.11). It is also

important to note the large variance associated with these ensemble differences can partially be attributed to the lack of control exerted on the error contribution from the choice of a priori initial pressure for lidar data and a priori contribution and non-LTE effects for satellite data. Part of the difference may also be due to altitude offsets and coarse vertical resolution.

Having applied these new data filtering techniques we have produced an improved lidar temperature data set which is exploited in the companion paper (R. Wing, A. Hauchecorne, P. Keckhut, Godin-Beekmann, S. Khaykin, and McCullough, 2018b) in an effort to validate satellite temperatures.

2.8.2 OHP Lidar 20 Year Comparison

We have conducted the first ever decadal temperature inter comparison between a co-located 532 nm Rayleigh lidar and an ozone DIAL system calculating temperatures from a 355 nm line. We have shown that:

- 1) Rayleigh lidar temperatures calculated from ozone DIAL non-absorbing 355 nm line are statistically equal to temperatures from a traditional 532 nm Rayleigh temperature lidar over a large altitude range. This finding is of particular interest for the NDACC lidar temperature database as temperatures from ozone lidars may also be available for validation and inclusion.
- 2) Further theoretical work must be done on algorithms for melding data from high and low gain photon counting channels. The current techniques produce statistically identical nightly temperature profiles however, a -0.6 K bias near 40 km becomes apparent when multiple years of data are compared. It is doubtful that current data processing techniques can be easily adapted to address this problem. However, an iterative, cost minimising, Bayesian approach such as the one proposed by (R. Sica and Haeefele, 2015) would be able to produce a single melded temperature profile with the accompanying averaging kernels and an estimate of the error due to the photon count melding. As a lidar development note, Fig. 2.13 demonstrates the need move towards the use of automated nightly alignment of lidar system optics. Manual alignment by operators appears to lack consistency over the time frame of multiple decades.

3) The two independent lidars show no evidence of significant instrument drift over a 20 year period. This means that ground based lidars are the ideal choice of instrument for detecting small calibration drifts in satellite remote measurements over long time scales. We rely on this finding to justify the use of lidars as a reference data set for satellite validation in the companion paper R. Wing, A. Hauchecorne, P. Keckhut, Godin-Beekmann, S. Khaykin, and McCullough, 2018b.

4) There is no evidence of a relative vertical offset between the two independently calibrated lidar systems which would be seen as an ‘S’ shaped temperature bias in Fig. 2.15 due to the sign change in temperature vertical gradient at the stratopause (T. Leblanc et al., 1998a). Based on personal communication, recent July-August 2017 and March 2018 NDACC Ozone validation campaign at OHP (LAVANDE) revealed no vertical shifts between either OHP lidar and the NASA STROZ mobile validation lidar (McGee et al., 1995).

3 Lidar temperature series in the middle atmosphere as a reference data set. Part B: Assessment of temperature observations from MLS/Aura and SABER/TIMED satellites

1

3.1 Author Contribution

Robin Wing conceived of the study idea systematically compare OHP lidar temperature profiles to MLS and SABER over a decadal time span. He conducted sensitivity testing and wrote the codes for a data selection and coincidence criteria. He ran the comparison between the ground and space based temperature profiles and calculated the statistics and comparison parameters. He analysed the temperature differences and developed the idea to shift the stratopause height to ameliorate the comparison. He then wrote the manuscript.

¹Wing, R., Hauchecorne, A., Keckhut, P., Godin-Beekmann, S., Khaykin, S., and McCullough, E. M. (2018). *Lidar temperature series in the middle atmosphere as a reference data set. Part B: Assessment of temperature observations from MLS/Aura and SABER/TIMED satellites*, Atmospheric Measurement Techniques, European Geosciences Union, pp.(Under Review).

3.2 Abstract

We have compared 2433 nights of Rayleigh lidar temperatures measured at L'Observatoire de Haute Provence (OHP) with co-located temperature measurements from the Microwave Limb Sounder (MLS) and the Sounding of the Atmosphere by Broadband Emission Radiometry instrument (SABER). The comparisons were conducted using data from January 2002 to March 2018 in the geographic region around the observatory (43.93° N, 5.71° E). We have found systematic differences between the temperatures measured from the ground based lidar and those measured from the satellites which suggest non-linear distortions in the satellite altitude retrievals. We see a winter stratopause cold bias in the satellite measurements with respect to the lidar (-6 K for SABER and -17 K for MLS), a summer mesospheric warm bias (6 K near 60 km), and a vertically structured bias for MLS (-4 to 4 K). We have corrected the stratopause height of the satellite measurements using the lidar temperatures and have seen an improvement in the comparison. The winter relative cold bias between the lidar and SABER has been reduced to 1 K in both the stratosphere and mesosphere and the summer mesospheric warm bias is reduced to 2 K. Stratopause altitude corrections have reduced the relative cold bias between the lidar and MLS by 4 K in the early autumn and late spring but were unable to address the vertical artefacts in the MLS temperature profiles.

3.3 Introduction

Satellite atmospheric measurements are vital for providing global assessments of long term atmospheric temperature trends. However, particular care must be taken to validate each new satellite as well as provide periodic ground checks for the entire instrument lifetime in order to counter drifts in calibration and local measurement time (Wuebbles, Fahey, and Hibbard, 2016). Changes in satellite measurements can occur over the course of a mission due to instrument degradation, calibration uncertainties, orbit changes, and errors/assumptions in the forward model parameters. Additionally, most mission planning agencies have guidelines which require that satellite programs conduct formal validation studies to ensure accuracy and stability of the measurements (Council, 2007).

3.3.1 Lidar as a Validation Tool

Rayleigh lidar remote sounding of atmospheric density and temperature is an excellent tool for use in validating satellite measurements over a specified geographic area and vertical range. Lidars can make routine high resolution measurements over a large portion of the middle atmosphere in regions which are notoriously difficult for other techniques to measure routinely or precisely. There are three key strengths in the Rayleigh lidar technique which set it apart from other atmospheric sounders. First is the ability to retrieve an absolute temperature profile from a measured relative density profile with very high spatio-temporal accuracy and precision. Second, lidars measure range by measuring the time required for a back-scattered photon to return to the station and be recorded by the photon counting electronics. The current OHP lidar uses a Licel digital recorder and has a sampling 40 MHz which corresponds to a vertical resolution of 7.5 m. The uncertainty on the sampling rate is negligible however, there is the possibility of trigger delay and jitter in the counting electronics of 50 ± 12.5 ns Licel, 2018 contributing a maximum possible uncertainty of 18.25 ± 3.25 m in the raw lidar measurement. This error is constant with altitude which allows us to sample the upper middle atmosphere with the same range resolved confidence as the lower middle atmosphere and troposphere. Third, as a benefit of active remote sensing raw lidar measurements don't suffer from vertical distortion in the altitude vector. Each altitude level in a lidar measurement corresponds to an independent collection of back-scattered photons which are returning at a defined time from a given altitude range. In contrast, passive remote sensors such as limb scanning satellites can suffer biases at high altitudes due to: radiometric and spectral calibration, field of view and antenna transmission efficiency, satellite pointing uncertainty, as well as biases introduced by the forward model (Schwartz et al., 2008). Additionally, many satellites like MLS are optimised for tropospheric and lower stratospheric measurements and conduct faster scans with fewer channels at higher altitudes (N. J. Livesey et al., 2006). These different biases can exist simultaneously in both the retrievals of temperature and pressure and can be considered, in part, as distortions in the altitude vector when compared to lidar measurements.

3.3.2 Previous Lidar-Satellite Temperature Studies

Previous studies comparing ground based lidar and satellite measurements of temperature have often used Sodium Resonance lidars to compare the lidar derived neutral temperature between 85 km and 105 km to satellite temperatures in the mesopause region. Studies of this sort have generally shown good agreement between ground and satellite observations (Xu et al., 2006). Due to the strength of Na lidars in the upper mesosphere they naturally lend themselves well to studies of tides and wave breaking dynamics.

Coincident with this work (Dawkins et al., 2018) submitted a comparison of temperature profiles from 9 different metal resonance lidars with temperature profiles from SABER from 75 to 105 km. At all sites they found that SABER temperatures were cooler than the lidar temperatures by $-9.9 (\pm 9.7)$ K at 80 km. The study used coincidence criteria of $\pm 15^\circ$ longitude, $\pm 5^\circ$ latitude, and ± 30 minutes between the lidar and satellite profiles. A weak and unexplained mesospheric summer bias was also reported. In the supplemental material to (Dawkins et al., 2018) a sensitivity study was done for SABER overpasses as a function of season and size of the co-location area. They found no significant differences between a co-location area with a longitudinal size of $\pm 5^\circ$ and $\pm 15^\circ$.

A study by (Yuan et al., 2010) compared Na lidar and SABER temperatures in the context of a 6 year tidal analysis. They found semiannual disagreements in the tidal amplitude around the spring and autumn equinoxes with a maximum difference of 12 K near 90 km occurring in February. Several explanations and partial corrections were offered but the phenomenon is robust and the authors concluded that further study was required to fully resolve the temperature discrepancy. Studies have also been done comparing temperatures calculated from the Rayleigh lidar technique and those derived from SABER and MLS observations. (Taori, Dashora, et al., 2011; Taori, Jayaraman, et al., 2012; Taori, Kamalakar, et al., 2012) comprise an excellence series of publications using multiple instruments to measure the atmospheric temperature from 40 km to 100 km. These works found good agreement between the lidar and SABER up to 65 km and significant initialization errors in the lidar of up to 25 K near 90 km. We have partially accounted for this initialization induced lidar warm bias in the companion paper (Robin Wing et al., 2018a). Our work here offers two improvements on these three publications. Firstly, we have not focused as much on case studies but rather on the statistics of

nearly a decade of lidar-satellite inter-comparisons. Secondly, we have conducted our comparisons on a 1 km grid in an effort to match small scale features in the temperature profiles.

A good lidar to satellite temperature comparison was done by (Siva Kumar, Rao, and Krishnaiah, 2003) using 240 nights of lidar temperatures, temperatures from UARS, and model temperatures from CIRA-86 and MSIS-90. They compared monthly and seasonal averages and found significant semiannual temperature anomalies in the region of 45 – 50 km in February-March and September-October as well as initialization related biases above 70 km. A second study by the same authors compared 14 years of monthly average lidar temperatures to temperatures from the satellites SABER, HALOE, COSMIC, and CHAMP (V. Sivakumar et al., 2011). As with the previous study temperature anomalies of 3-5 K were identified in the region near the stratopause. The differences were attributed to monthly averaging and slight differences in measurement time and location of the lidar and satellites. The approach employed in our work is to make comparisons of nightly averages and then study the monthly median of the temperature differences – an approach which will allow for finer temporal precision.

Another study which compares 120 nights of Rayleigh lidar temperatures measured over Beijing to temperatures from SABER over the course of one year found good agreement between monthly average temperature profiles (Yue et al., 2014). This study found winter time temperature anomalies in the stratopause region and attempted to account for these features by fitting an annual, semi-annual, and 3 month sinusoid to the data. The objective of our study is similar to that of Yue et al., 2014 insofar as we are interested in the time evolution of lidar-satellite temperature comparisons and identifying potential seasonal or decadal trends. However, we are seeking to make nightly temperature comparisons between lidar and two satellites, SABER and MLS, over multiple years without assuming large contributions from an Annual Oscillation (AO) or its harmonics. Our study uses more than 9 times as many coincident measurements and spans the entire SABER data record.

Further study of seasonal temperature anomalies between ground based lidar and SABER was done by (Dou et al., 2009) comparing 2332 nights of lidar data from 6 different sites in the Network for the Detection of Composition Change (NDACC) to zonally averaged temperature profiles from SABER. This study found a 2-5 K

systematic bias in the stratopause region and concluded that this result may be due to either a bias in SABER, tidal aliasing, or sporadic aerosols. As well the study found systematic temperature differences in the upper mesosphere which were attributed to tidal aliasing, bias in the SABER temperature retrieval, or temperature differences due to the AO. In our work we use a smaller geographic window and not a zonal average temperature to compare more truly co-incident measurements. As well we limit the time difference between the lidar and satellite measurements to minimise possible tidal contributions.

3.3.3 Alternative Measurement Techniques

Other current measurement techniques for atmospheric temperature in this region of the atmosphere include:

- a) Rocketsondes were used during the early satellite era to make in situ measurements of the middle atmosphere but this technique has many well known limitations and requires large corrections and uncertainties in the upper mesosphere (Johnson and Gelman, 1985).
- b) Meteor radar techniques provide an estimation of the temperature at 90 km and can operate on a near continuous basis but they require several a priori assumptions and must be calibrated with data from an independent source (Meek et al., 2013)
- c) Satellites, like MLS and SABER provide globally distributed temperature measurements at several pressure levels throughout the vertical atmospheric column (Waters et al., 2006) (Mertens et al., 2001). Satellite based measurements provide a very good global view of the Earth's middle atmosphere but can suffer from calibration errors, temporal coverage gaps, and problems with vertical resolution.
- d) OH airglow imagers (Pautet et al., 2014) provide high spatio-temporal resolution 2D images of temperature perturbations derived from OH emissions near 87 km. These instruments can provide excellent wide field of view measurements over a geographic area but cannot yield vertical profiles of temperature.
- e) Ground-based resonance doppler and Boltzmann lidars can derive temperatures from sodium, iron, and other meteoric metal layers in the upper mesosphere and lower thermosphere (80 - 115 km) (Chu et al., 2002). These techniques are not

only useful in deriving temperature profiles but are also well situated for studies of other middle atmospheric phenomena such as gravity waves and noctilucent clouds. These lidars are restricted to measuring in the altitude band defined by the distribution of each metallic layer.

Considered together, this suite of remote sensing techniques can provide a comprehensive view of the middle atmosphere. The inclusion of Rayleigh lidar data into multi-sensor studies of the middle atmosphere provides an important local ground truthing perspective which helps to refine the global view offered by other techniques.

3.3.4 Outline of this Work

In this work we give a brief description of the instruments involved in the study (Sect. 3.4), a definition of the geographic area under consideration, and several criteria for determining coincidence between lidar and satellite measurement profiles (Sect. 3.5). In Sect. 3.6 we directly compare temperature profiles from MLS and SABER to the lidar temperatures and show a monthly median difference climatology and note several systematic differences. Section 3.7 details a procedure to correct the satellite temperature profiles based on the height of the stratopause in the lidar data. Finally, Sect. 3.8 shows an improved lidar-satellite monthly median difference climatology based on the altitude corrected satellite data.

3.4 Instrumentation

The Observatoire de Haute Provence (OHP) Rayleigh lidars have been in operation in southern France since 1978 and routinely produce nightly average temperature profiles of the upper stratosphere and lower mesosphere. The details of the Rayleigh lidar algorithm and the OHP lidar specifications are presented in the companion publication (Robin Wing et al., 2018a).

SABER is a broadband radiometer aboard NASA's TIMED (Thermosphere Ionosphere Mesosphere Energetics Dynamics) satellite and makes temperature measurements based on CO₂ limb radiances from 20 km to 120 km. SABER has a

vertical resolution of 2 km and random temperature errors of less than 0.5 K below 55 km, 1 K at 70 km, and 5 K at 100 km (Remsberg et al., 2008). TIMED does not have a sun synchronous orbit and does not pass through our OHP comparison area at a fixed local time. This makes finding temporally coincident measurements with the lidar relatively easy. We are using version 2.0 of the published SABER temperatures. Further information for SABER/TIMED can be found in (Mertens et al., 2001).

MLS is a microwave spectrometer aboard the Aura satellite and makes temperature measurements based on emissions from O₂. Further information can be found in (Waters et al., 2006). MLS vertical averaging kernels have a full-width-half maximum of 8 km at 30 km, 9 km at 45 km, and 14 km, at 80 km and a temperature resolution which goes from 1.4 K near 30 km to 3.5 K above 80 km (Schwartz et al., 2008). We are using version 4.0 of the published MLS temperatures. MLS is a sun synchronous satellite which passes the equator around 1h45 UTC and is generally temporally coincident with the last hour or so of lidar measurements.

3.5 Comparison Parameters

Defining coincident measurements between satellites and lidars can be difficult due to temporal and spatial offsets, differences in viewing geometry, and different approaches to smoothing. Studies such as García-Comas et al., 2014b have defined short time windows over a 1000 km square surrounding the observatory as sufficient for coincidence while others such as (Yue et al., 2014) have chosen to approach the problem by looking at monthly averages over a much narrower latitude band.

For this study we wanted to compare to satellite profiles geographically near the lidar to minimise latitudinal variations in the temperature and within a small time frame to minimise the contribution of tides, tidal harmonics, and gravity wave effects. This desire for close spatio-temporal matching was balanced against the need for a sufficiently large number of comparisons as to produce results which are statistically significant and useful. Ultimately, we decided on a geographic window of $\pm 4^\circ$ latitude and $\pm 15^\circ$ longitude similar to the analysis done by (Dou et al., 2009). We reasoned that the UMLT (Upper Mesosphere and Lower Thermosphere) structure would vary with latitude to a greater degree than with longitude and

that the longitudinal separation between consecutive SABER satellite passes gives a natural bound on the longitude. The contemporaneous work by (Dawkins et al., 2018) includes a sensitivity study on the choice of longitudinal co-location limits. Their final choice for a spatial coincidence ($\pm 5^\circ$ latitude, $\pm 15^\circ$ longitude) is comparable to our study which employs ($\pm 4^\circ$ latitude, $\pm 15^\circ$ longitude). Figure 3.1 shows the geographic extent of our study.

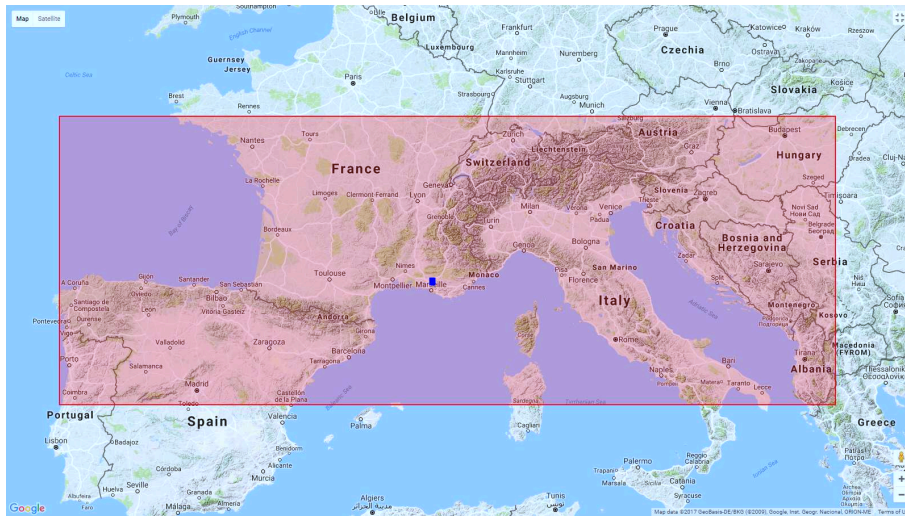


FIGURE 3.1: Area defined for coincident measurements (40° N, 9° E) to (48° N, 21° E). L'Observatoire de Haute-Provence in blue at (43.93° N, 5.71° E). (Google, 2017)

The minimum length of an OHP nightly lidar temperature measurement is four hours. We chose to use a ± 4 h window around the lidar measurement as the temporal limit for coincidence with a satellite pass. This gives us a roughly 12 h window centred around the middle of the lidar measurement. Our choice was influenced by a desire to minimise the effect of the 12 h tidal harmonic. Previous work comparing between satellites have been able to take advantage of daytime satellite overpasses and chose to work within a ± 2 h window (Hoppel et al., 2008). (French and Mulligan, 2010) conducted a comparison between an OH spectrometer (in conjunction with a sodium lidar) and SABER at ± 15 min and ± 8 h and found no significant difference. However, it must be noted that this study was conducted at a latitude of 69° S and the comparison may not hold in the mid-latitudes.

3.6 Temperature comparisons without considering vertical offset

Here we demonstrate the directly-calculated temperature biases between OHP and both SABER and MLS which are present before we carry out the adjustment for satellite altitude offsets which are discussed in Sect. 3.7. An example of all three temperature profiles for the night of the 25th of July 2012 is shown in Fig. 3.2. In this comparison the lidar profile was produced over 4 hours and has a vertical resolution of 150 m from 30 km to above 90 km. The large temperature uncertainty above 70 km is a result of the fine vertical resolution required to capture the mesospheric inversion layer present near 77 km.

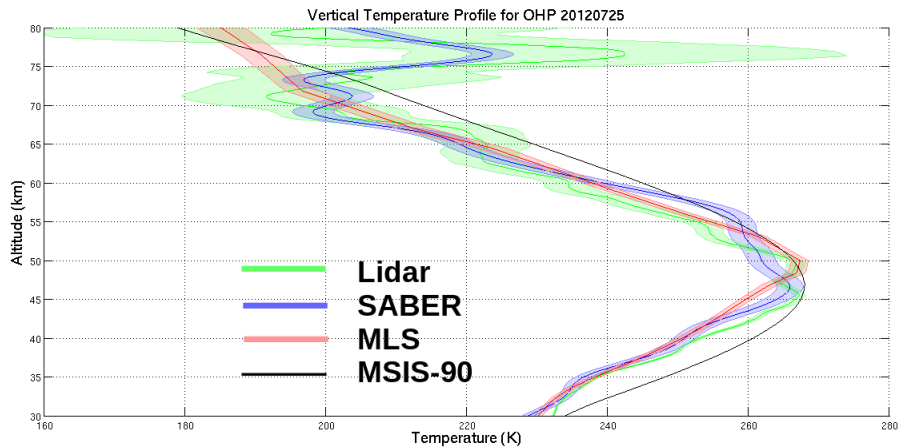


FIGURE 3.2: Example co-located temperature profiles from the OHP lidar (green), SABER (blue), MLS (red), and MSIS (black).

3.6.1 Comparison OHP Lidar and SABER

From 2002 to 2018 there were 1100 coincident measurements of sufficient quality between OHP lidars and SABER. Figure 3.3 (upper panel) shows the monthly median temperature differences between the lidar and SABER while Fig. 3.3 (lower panel) shows the mean seasonal temperature bias with altitude.

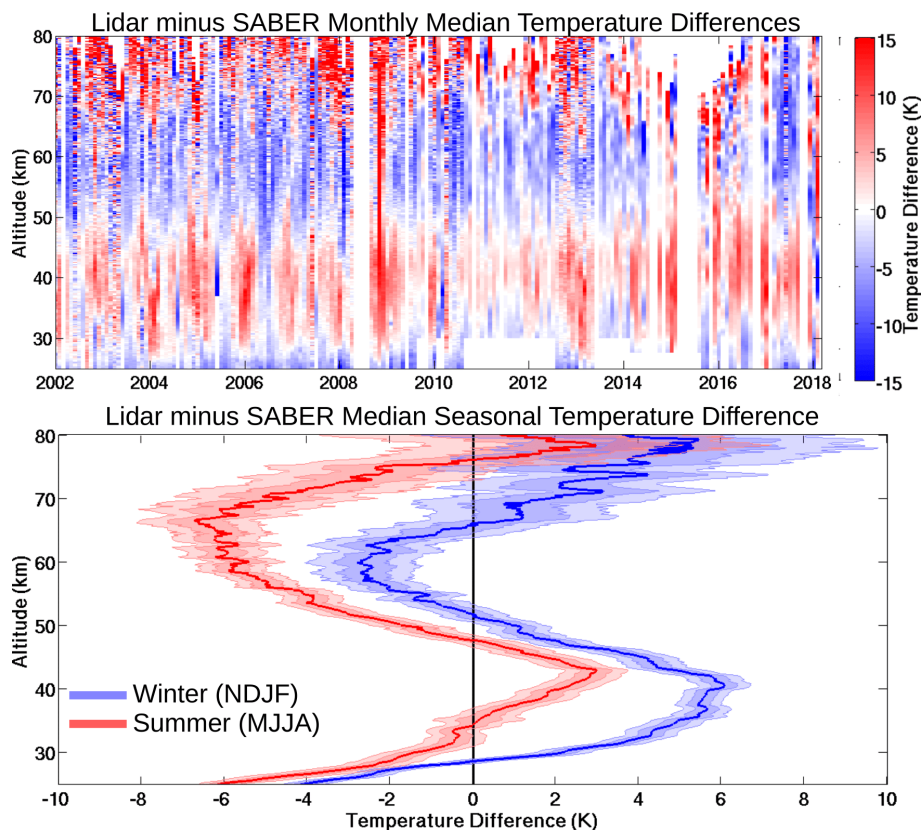


FIGURE 3.3: Sixteen year systematic comparison of OHP lidars and SABER temperatures. The monthly median temperature differences between the lidar and SABER are shown in the upper panel. Red indicates that the lidar is warmer than SABER and blue that the lidar is colder. There are 1100 nights of coincident measurements in the colour plot. The lower panel is a seasonal ensemble of lidar minus SABER temperature differences. The summer (May, June, July, August) ensemble in red includes 306 nights of coincident measurements and the winter (November, December, January, February) ensemble in blue includes 397 nights of coincident measurements. Shaded errors represent 1 and 2 standard deviations.

Figure 3.3 upper panel contains the monthly median temperature differences between an OHP lidar temperature profile and a SABER temperature profile. After 2010 there are several time periods where the Lidar Température et Aérosol (LTA) was not in routine operation or was in the process of being upgraded. To fill in these data gaps we have used temperature profiles derived from the ozone Differential Absorption Lidar (DIAL), also referred to as Lidar Ozone Stratosphère (LiO₃S), which is described and validated for temperature in (Robin Wing et al., 2018a). Given that the main scientific interest of LiO₃S is stratospheric ozone, the noise floor of the raw lidar signal occurs at a lower altitude than for LTA for similar vertical integration. To produce temperature profiles which extend into the mesosphere we use a coarser vertical resolution, a minimum altitude of 30 km, and often stop the temperature profile below 80 km if the temperature error becomes excessive.

The upper panel shows a relative warm bias for the lidars with respect to SABER above 70 km. Discrepancies in this region are likely due to lidar initialization errors and background uncertainty which we have attempted to minimise in the companion publication (Robin Wing et al., 2018a). There is also an evident seasonal relative warm bias in the winter stratosphere between 30 km and 50 km - a region where lidar uncertainties in both altitude and temperature are well described (T. Leblanc, R. J. Sica, et al., 2016) (T. Leblanc et al., 2016). The lower panel shows a very distinctive ‘S’ shape to the bias in both the winter and summer ensembles which is indicative of a vertical offset between the lidar and satellite measurements. The basic ‘S’ shape bias was identified in studies of synthetic lidar data as being due to vertical offsets between lidar instruments (T. Leblanc et al., 1998b). Unfortunately, this offset is neither constant from night to night, nor constant with altitude as evidenced by the elongated and distorted nature of the ‘S’ shape.

If we bin all the temperature differences by month we can clearly see that there is a winter stratospheric warm bias below 45 km and a pronounced summer cold bias in the mesosphere between 50 and 70 km, as shown in Fig. 3.4.

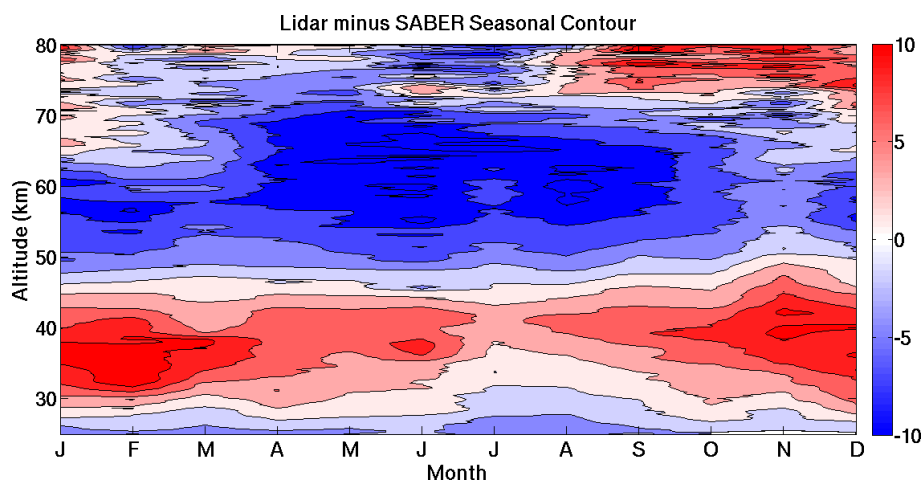


FIGURE 3.4: Monthly median temperature difference between lidar and SABER temperature measurements. Red indicates regions where the lidar measures warmer temperatures than SABER and blue regions where the lidar measures colder temperatures than SABER.

3.6.2 Comparison OHP lidar and MLS

From 2004 to 2018 there were 1741 coincident measurements of sufficient quality between OHP lidars and MLS. Figure 3.5 (upper panel) shows the monthly median temperature differences between the lidar and MLS while Fig. 3.5 (lower panel) shows the mean seasonal temperature bias with altitude.

As was the case with the lidar-SABER comparison, in the upper panel we see a lidar warm bias above 70 km and a strong winter stratospheric warm bias near 45 km. In this comparison the stratospheric warm bias appears to have a downward phase migration as the winter progresses. In the corresponding lower panel we see very pronounced summer time systematic differences which alternate from warm to cold throughout the stratosphere and mesosphere. The winter ensemble shows a very large lidar warm bias near the stratopause.

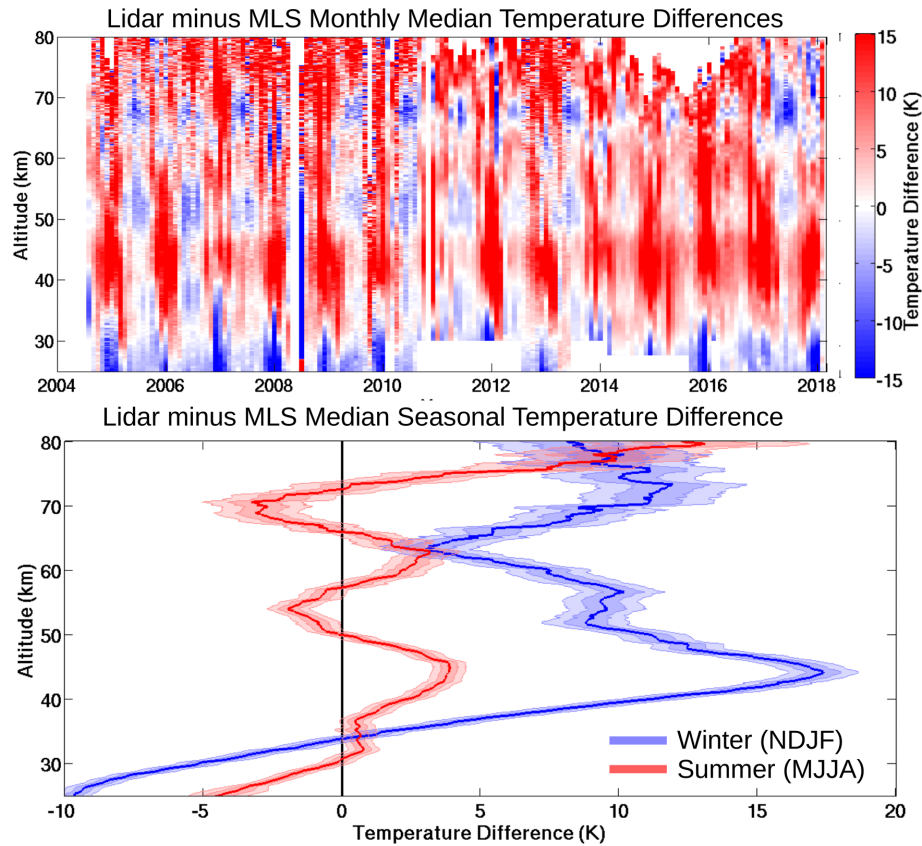


FIGURE 3.5: Fourteen year systematic comparison of OHP lidar and MLS temperatures. The monthly median temperature differences between the lidars and MLS are shown in the upper panel. There are 1741 nights of coincident measurements. The lower panel is a seasonal ensemble of lidar minus MLS temperature differences. The summer (May, June, July, August) ensemble in red includes 554 nights of coincident measurements and the winter (November, December, January, February) ensemble in blue includes 653 nights of coincident measurements. Shaded errors represent 1 and 2 standard deviations.

Following the same procedure of binning lidar-MLS temperature differences by month we see a very pronounced downward phase progression of the winter stratospheric warm bias from 45 km in January descending down to 40 km in February

and March. Additionally, there is an evident layered cold bias in the summer stratosphere and mesosphere. The three layers appear near 37 km, 53 km, and 68 km in Fig. 3.6.

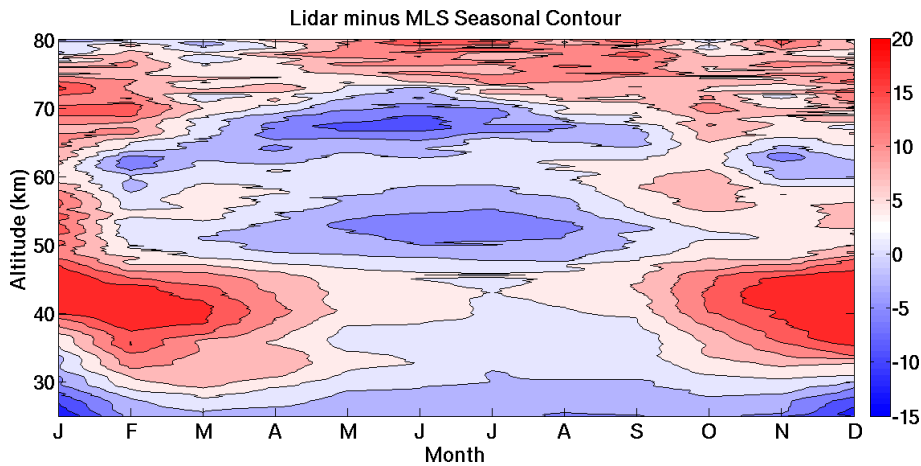


FIGURE 3.6: Monthly median temperature difference between lidar and MLS temperature measurements. Red indicates regions where the lidar measures warmer temperatures than MLS and blue regions where the lidar measures colder temperatures than MLS.

3.7 Minimising Temperature Difference Between Lidar and Satellites with a Vertical Offset

We investigated a possible vertical offset between the lidar and satellite measurements to determine whether this could be contributing to the temperature biases seen in Sect. 3.6.

3.7.1 Method to determine the vertical offset between measurements

To match the two temperature profiles exactly in amplitude and altitude requires a unique altitude dependent correction factor for each comparison. However, we can make a rough estimate of the average vertical offset between the two measurements by focusing on the region of the stratopause which generally has a defined altitude and a clear structure. We used a simple least squares method to best estimate the vertical offset that would minimise the temperature differences between the lidar measurement and the satellite measurement. Two examples of this offset calculation for SABER are shown in Fig. 3.7 and two examples for MLS are shown in Fig. 3.8. The examples in these figures show nights where the lidar and satellite temperatures are in good agreement or can be brought into good agreement by applying a small vertical displacement. However, it is important to note that there are examples of lidar-satellite temperature measurements which cannot be brought into good agreement with small vertical displacements. Two such examples can be found in Fig. 3.9. These examples of poor agreement are almost exclusively found in winter on nights where the stratopause is greatly disturbed.

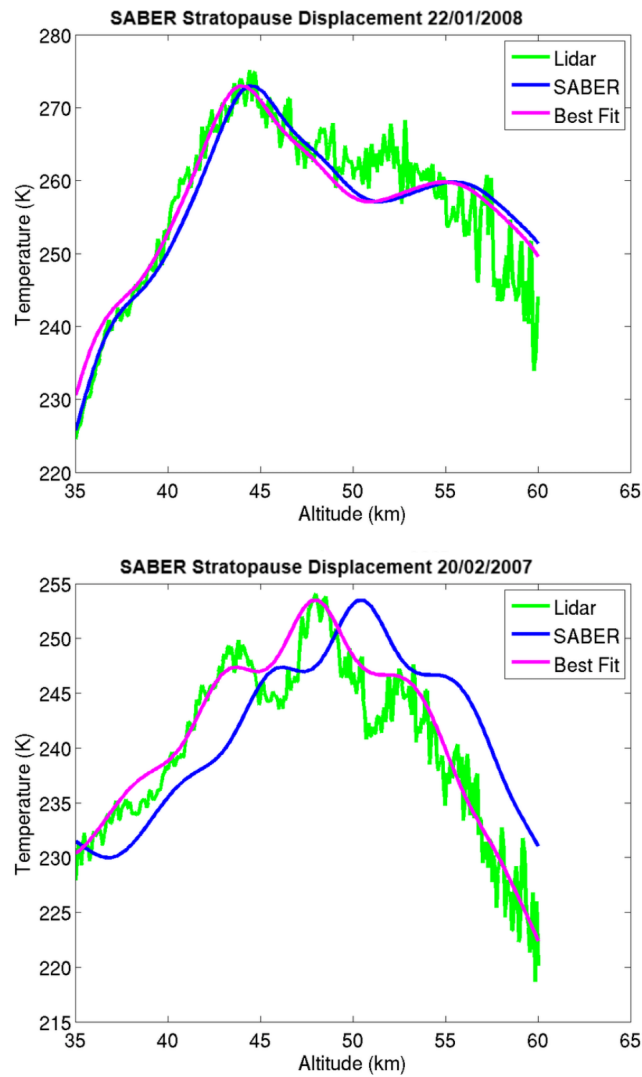


FIGURE 3.7: The upper panel shows a case where the lidar and SABER were well aligned in altitude. The lower panel shows a case where a vertical displacement of the SABER profile ameliorated the agreement with the lidar measurement.

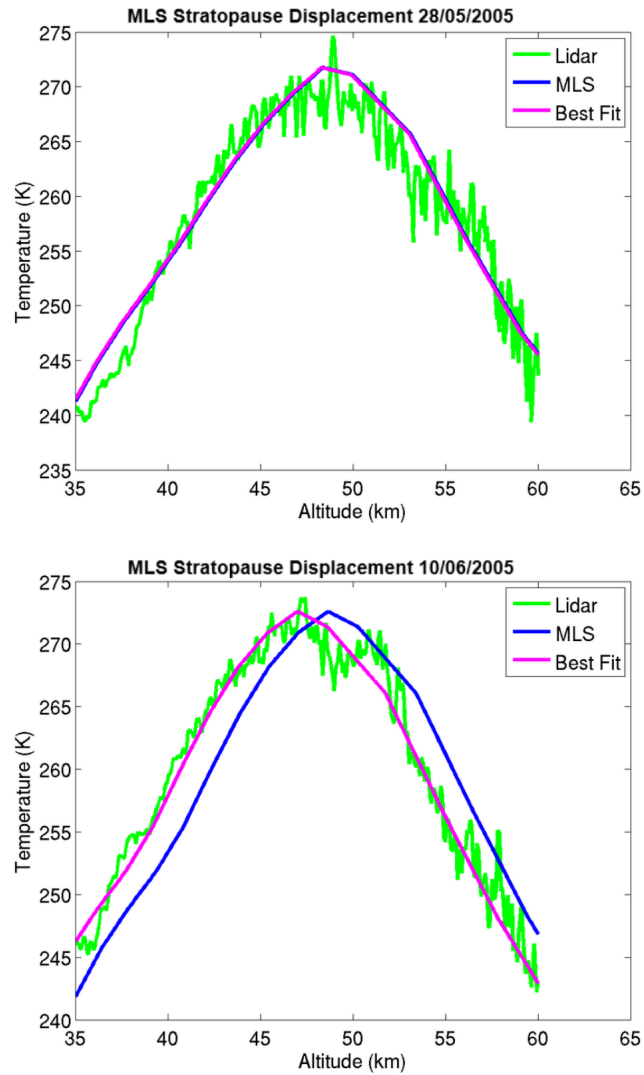


FIGURE 3.8: The upper panel shows a case where the lidar and MLS were well aligned in altitude. The lower panel shows a case where a vertical displacement of the MLS profile ameliorated the agreement with the lidar measurement.

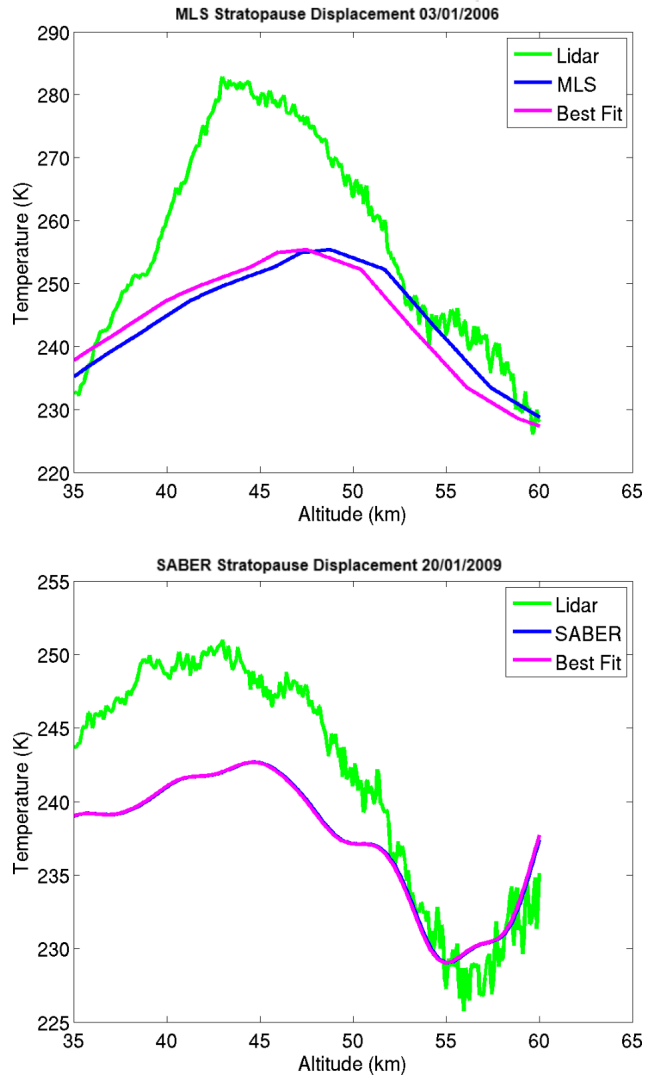


FIGURE 3.9: Two examples of poor matches between lidar and satellite temperature profiles (MLS upper panel, SABER lower panel). These mismatches mainly occur between late November and early April on nights where the stratosphere was disturbed and experiencing a warming.

3.7.2 Trends in Vertical Offset between Lidar and Satellites

We calculated an offset for every coincident measurement between the lidars and SABER and the lidars and MLS. The monthly average of this altitude offset value is represented in Fig. 3.10 as a green line for years where the comparisons were primarily between LTA and the satellites and as a blue line for years where LiO₃S temperatures were used. The green and blue shaded regions are the respective standard deviations. Given the reduced vertical resolution of the temperature profiles from LiO₃S, the least-squares minimised correction for stratopause height is less sensitive to small and medium scale fluctuations in the temperature profiles such as the triple peak structure seen in the lower panel of Fig. 3.7. As a result, comparisons between LiO₃S and both satellites (blue curve in Fig. 3.10) tend toward the mean altitude displacement. This effect is more pronounced when comparing with SABER, which has a finer vertical resolution, than when comparing with MLS which has a coarser vertical resolution. There is a clear, but imperfect, seasonality to these altitude displacements.

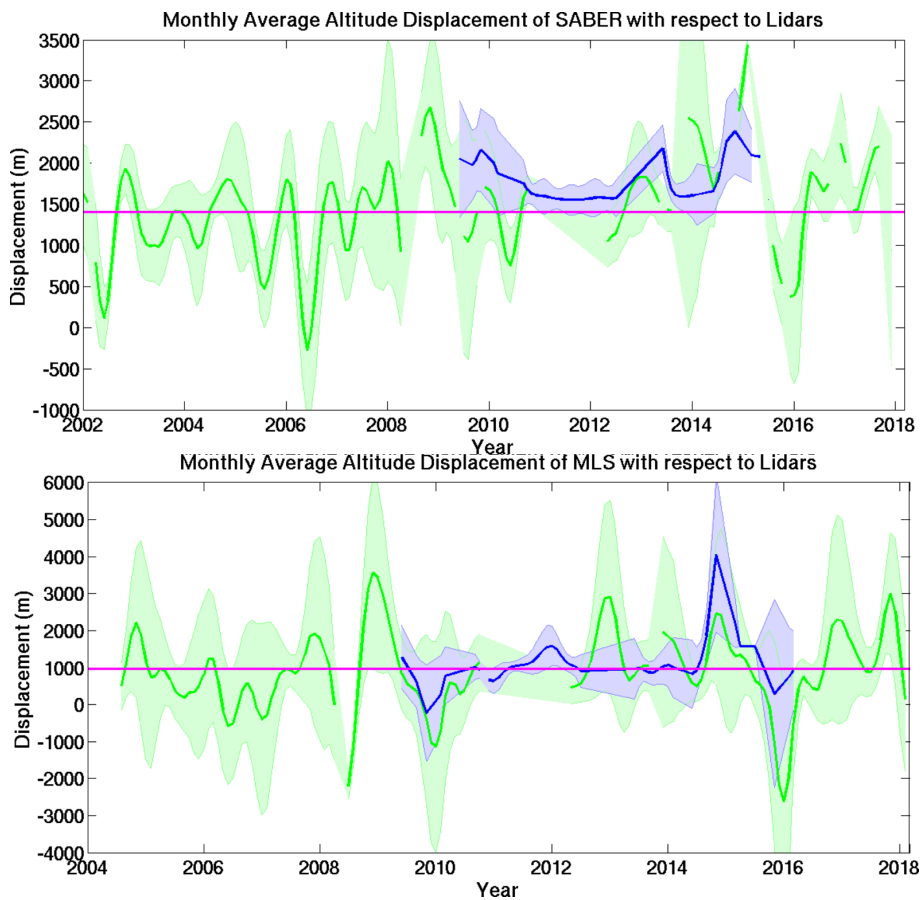


FIGURE 3.10: The upper panel features the monthly average displacement of SABER measurements with respect to the OHP lidars (green for LTA and blue for LiO_3S). The standard deviation is given as the shaded area. The mean offset (magenta) is 1446 m with a standard error of 49 m. The lower panel shows the same analysis with the monthly average MLS displacement. The mean value is 911 m with a standard error of 90 m.

Superimposing the traces shown in Fig. 3.10 onto the colour plots in Fig. 3.3 and Fig. 3.5 shows a clear correlation between lidar-satellite temperature anomalies and mean monthly altitude displacement between the lidar and satellite temperature profiles, as shown in Fig. 3.11.

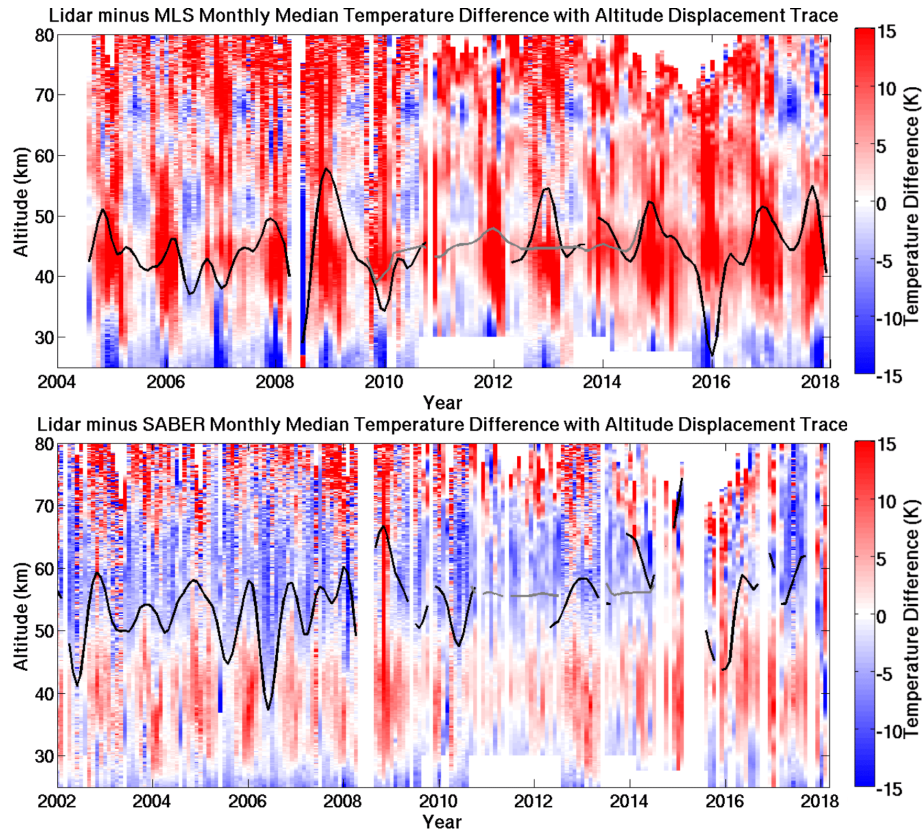


FIGURE 3.11: The upper panel features the monthly median temperature differences between the lidar and MLS seen in 3.5 with the estimated vertical displacement of the stratopause height over-plotted. The lower panel features the monthly median temperature differences between the lidar and SABER seen in 3.3 with the estimated vertical displacement of the stratopause height over-plotted. The black line represents comparisons between LTA and the satellite and the grey line represents comparisons between LiO₃ and the satellite.

3.8 Recalculated Lidar-Satellite Temperature Differences

We have attempted to make a more accurate comparison of the lidar and satellite temperatures by using the stratopause height as a common altitude reference. We re-calculated the lidar-satellite temperature differences shown in Fig. 3.4 and Fig. 3.6 after displacing the satellite measurement by a scalar value. Each satellite measurement was shifted vertically according to the lidar derived stratospheric displacements shown in Fig. 3.10.

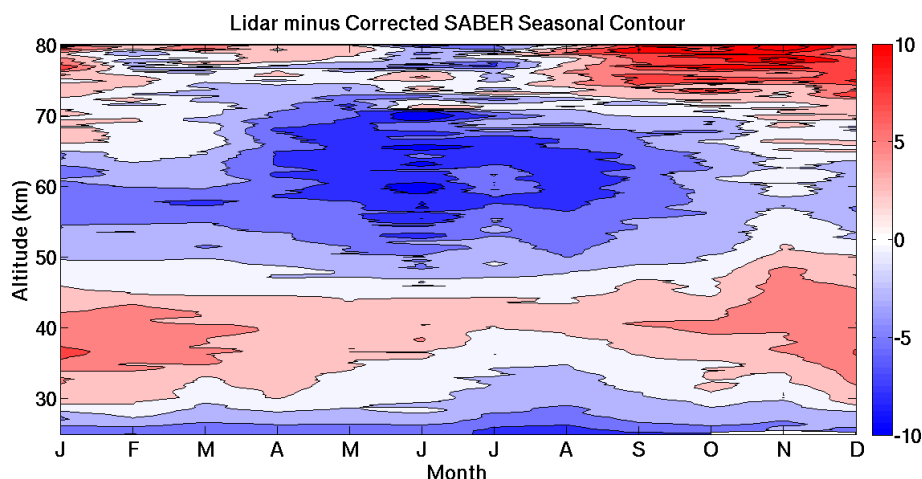


FIGURE 3.12: Corrected seasonal temperature differences between the lidar and the vertically displaced SABER temperatures. The magnitude of the temperature differences is reduced in both the stratosphere and mesosphere over the majority of the altitude range when compared to a similar uncorrected temperature difference contour seen in Fig. 3.4.

In Fig. 3.12 we see that by displacing the SABER temperature profiles so that the stratopause height is the same in both the lidar and satellite measurements we have reduced the maximum winter time stratospheric warm bias from approximately 8 K to 4 K. The summer time mesospheric cold bias of -10 K has likewise been reduced by between 4 and 6 K depending on altitude and season. The remaining

bias in both the stratosphere and mesosphere cannot be further minimised by a simple vertical shift. The altitude dependent correction which would be required to correct the temperature lapse rate is beyond the scope of this work.

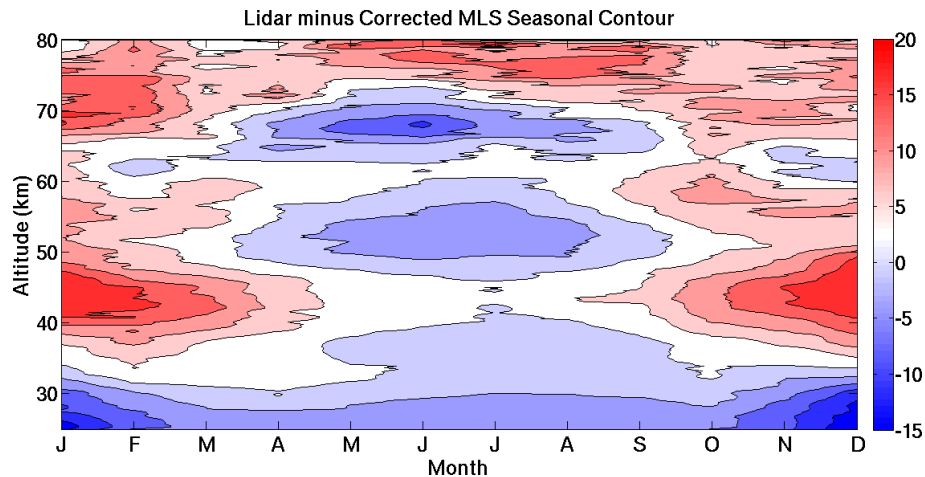


FIGURE 3.13: Corrected seasonal temperature differences between the lidar and the vertically displaced MLS temperatures. The structured nature of the temperature bias seen in Fig. 3.6 remains unchanged by the vertical correction.

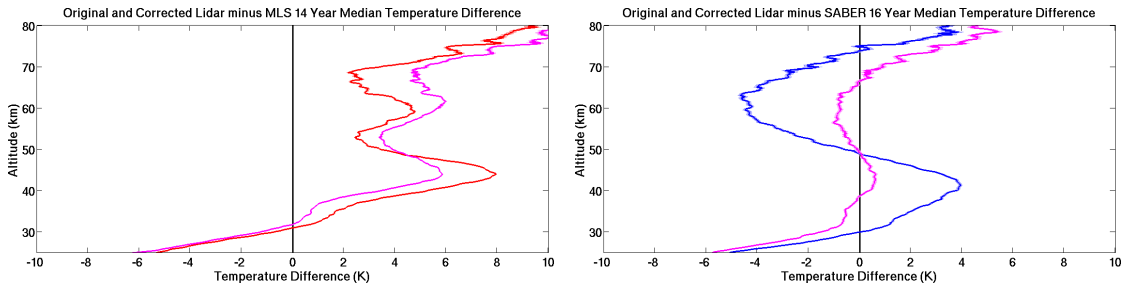
In Fig. 3.13 we see that displacing the MLS temperature profiles was less successful than in the case of the SABER measurements. We have reduced the magnitude of beginning and end of winter time stratospheric warm bias by up to 5 K during the months of March, April, October, and November but the correction does not completely eliminate the issue. As well we have an improvement of 5 K in the biased layer at 65 km. However, the horizontal layering inherent in the MLS temperature data makes determining a scalar correction even more challenging than in the case of SABER.

We have re-plotted the seasonal ensemble temperature difference curves shown in the lower panel of Fig. 3.3 (lidar-SABER) and Fig. 3.5 (lidar-MLS) alongside the ensemble temperature differences after we applied the correction for stratopause

height. Figure 3.14a shows the ensemble temperature difference for all 1741 lidar-MLS temperature comparisons before correction (red) and after correction (magenta). The prominent warm bias near 45 km has been reduced from 8 K to 6 K but the cold biases at 53 km, and 68 km are made worse by the correction. To understand this result we can look at the seasonal dependence of the applied correction. Figure 3.14c is the summer ensemble temperature difference (MJJA) consisting of 554 lidar-MLS temperature comparisons before correction (red) and after correction (magenta). There is marginal improvement after correction below 55 km but the change is not significant at 2σ and the structure of the temperature bias remains unchanged. Figure 3.14e is the winter ensemble temperature difference (NDJF) consisting of 653 lidar-MLS temperature comparisons before correction (blue) and after correction (magenta). There is significant improvement of 4 K in the large cold bias at 45 km. The corrected lidar-MLS comparison is also significantly worse near the cold bias at 63 km.

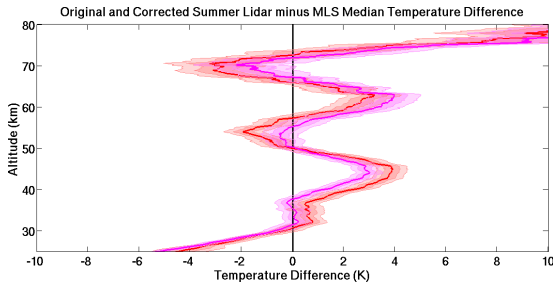
Figure 3.14b shows the ensemble temperature difference for all 1100 lidar-SABER temperature comparisons before correction (blue) and after correction (magenta). the stratopause height correction has reduced the stratospheric warm bias from 4 K to less than 1 K and has reduced the mesospheric cold bias from -4 K to -1 K. The warm bias above 70 km has been slightly increased. Figure 3.14d is the summer ensemble temperature difference (MJJA) consisting of 306 lidar-SABER temperature comparisons before correction (red) and after correction (magenta). There is a significant 3 K reduction in the warm bias at 45 km and a significant reduction in the mesospheric cold bias from -6 K to -3 K. Figure 3.14f is the winter ensemble temperature difference (NDJF) consisting of 397 lidar-SABER temperature comparisons before correction (blue) and after correction (magenta). By applying the altitude correction we have eliminated the ‘S’ shape in the temperature difference curve between 30 and 60 km. There is a significant 1 K constant warm bias that remains after correction. Above 70 km there is no statistically significant change.

Chapter 3. Lidar temperature series in the middle atmosphere as a reference
78data set. Part B: Assessment of temperature observations from MLS/Aura and
SABER/TIMED satellites

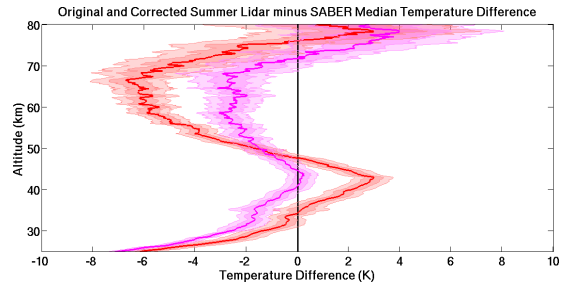


(A) Median temperature difference for 1741 lidar minus MLS temperature profiles from 2004 to 2018. Red is the original ensemble and magenta is the ensemble after correction.

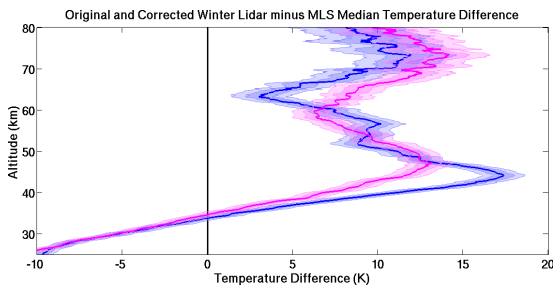
(B) Median temperature difference for 1100 lidar minus SABER temperature profiles from 2002 to 2018. Blue is the original ensemble and magenta is the ensemble after correction.



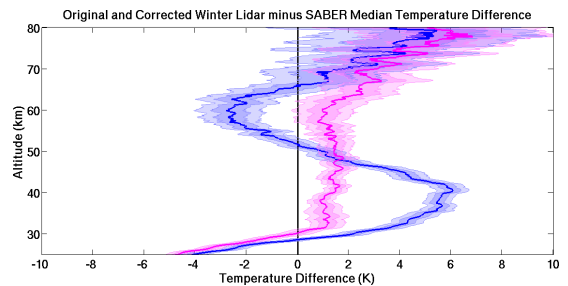
(C) Median summer (MJJA) temperature difference for 554 lidar minus MLS temperature profiles from 2004 to 2018. Red is the original ensemble and magenta is the ensemble after correction.



(D) Median summer (MJJA) temperature difference for 306 lidar minus SABER temperature profiles from 2002 to 2018. Red is the original ensemble and magenta is the ensemble after correction.



(E) Median winter (NDJF) temperature difference for 653 lidar minus MLS temperature profiles from 2004 to 2018. Blue is the original ensemble and magenta is the ensemble after correction.



(F) Median winter (NDJF) temperature difference for 397 lidar minus SABER temperature profiles from 2002 to 2018. Blue is the original ensemble and magenta is the ensemble after correction.

FIGURE 3.14: Ensemble for lidar minus MLS temperature differences (left) and lidar minus SABER (right). Ensembles for all profiles are on the top row, summer (MJJA) profiles in the middle row, and winter (NDJF) in the bottom row.

3.9 Discussion

3.9.1 The need for vertical altitude correction of satellite data

Improved observations of stratospheric and mesospheric temperature profiles and dynamical phenomena are required to advance our understanding of the middle atmosphere. The process of ground to satellite measurement comparison and validation is a vital ongoing scientific activity. By comparing long term, stable, continuous, high quality temperature measurements, such as those made by the lidars at OHP, to other data sets we can help to identify potential issues with calibration or retrieval algorithms.

We have presented individual cases in Fig. 3.7 and Fig. 3.8 where both MLS and SABER temperature profiles benefited from a slight vertical displacement based on lidar derived stratopause height. While this scalar adjustment does not correct for non-linear distortions in the altitude vector it can significantly reduce the magnitude of the temperature bias in the stratosphere and lower mesosphere as seen in Fig. 3.14a and Fig. 3.14b. This technique does not seem to work well when the stratopause is highly disturbed as can be seen in the two winter time examples in Fig. 3.9. The implications of satellite underestimation of sudden stratospheric warming events is of particular concern to reanalysis projects attempting to model middle atmosphere dynamics. However, by using lidar data to supplement the satellite record these fast dynamical processes can be better resolved.

3.9.2 Temperature biases between OHP lidar and SABER

In the companion publication (Robin Wing et al., 2018a) we attempted to reduce the magnitude of the initialization induced lidar warm bias which is often reported above 70 km. We have reduced the bias by up to 5 K near 85 km and nearly 20 K at 90 km. There still remains some residual systematic warm bias between the lidar satellite comparisons in this publication.

The average 9.9 ± 9.7 K bias at 80 km reported by (Dawkins et al., 2018) using 9 different metal layer resonance lidars compares favourably to our ensemble bias

of 5 K at 80 km Fig. 3.14b. Given that the resonance lidars do not initialise their temperatures using the same inversion algorithm as the Rayleigh lidars, and that the resonance lidars have a minimum uncertainty near 85 km, perhaps our Rayleigh temperatures are not as influenced by a priori as we thought. Further work needs to be done on the topic of initialization related bias to fully address the effects of noise and a priori choice on high altitude Rayleigh lidar retrievals. However, we are encouraged by our results and cannot discount the possibility that some of the remaining temperature difference is due to incorrect altitudes in the satellite data product.

When considering the residual temperature differences between the OHP lidars and SABER after the altitude correction based on lidar derived stratopause height we can see that much of the seasonal variability in the stratosphere and mesosphere has been reduced. We are still left with a general summer time cold bias over most of the atmospheric column, except near 45 km, which now achieves a maximum of -4 K in the June mesosphere. We cannot explain this bias from the perspective of the lidar data as nothing in our range resolution changes, our data acquisition cadence and measurement duration are very similar (Robin Wing et al., 2018a), and we are well into the linear region of lidar count rates and are not influenced by our a priori or saturated count rates. It is possible that there could be a tidal contribution as summer time lidar measurements start a bit later than winter time measurements due to a shorter astronomical night. However, given that our criteria for coincidence were chosen to minimise the effects of the first few tidal harmonics this seems unlikely. It is also possible that there is a seasonally dependent bias in the a priori used in the satellite retrieval of the geopotential height which could influence the satellite altitude vector.

The cold bias seen below 30 km is most likely due to possible contamination in the lidar data from aerosols and saturation in the low gain Rayleigh channel. Current OHP lidar measurements use Raman scatter data to correct for these effects and produce temperature profiles down to 5 km. However, this Raman data is not available for the entire 2002 to 2018 analysis period so we have opted not to include it in this work.

3.9.3 Temperature biases between OHP lidar and MLS

As with the comparison between the lidar and SABER, the lidar and MLS comparison has a pronounced warm bias above 70 km which is in keeping with previous studies. However, the magnitude and extent of this warm bias in MLS is much more pronounced than in the SABER comparison plot. Much of this difference is due to the reduced vertical resolution of MLS at these high altitudes. This holds true particularly when comparing lower vertical resolution lidar data to MLS.

The lidar MLS comparison has a winter time stratospheric warm bias which is not much reduced by simply shifting the location of the MLS stratopause (Fig. 3.14e). We have reduced the magnitude of the difference by 4 K but the stratopause altitude correction was markedly less successful than in the case with SABER. It is almost universally the case that sudden stratospheric warmings seen by the lidar are missed or smoothed over in the corresponding MLS measurement. Figure 3.9 (upper panel) is very much a typical comparison for periods when the stratosphere is highly disturbed. There is a limit to how much can be done to improve the lidar-MLS comparison using a simple scalar correction.

The vertical structure which dominates much of the middle portion of the lidar MLS comparison is also difficult to account for. The structure is particularly evident in Fig. 3.14c and is nearly insensitive to our applied altitude correction. There is nothing in the lidar technique that could explain this pattern. A similar horizontal banding pattern is seen in the comparison of MLS to The European Centre for Medium-range Weather Forecasts (ECMWF) assimilation in the MLS geopotential validation paper (Schwartz et al., 2008). The effect is most likely an artefact introduced in some stage of the satellite retrieval. Studies like ours provide a perfect opportunity to incorporate lidar information into the satellite retrieval and improve the satellite data products. Given the confidence we have in the fixed width and amplitude of the vertical kernels in the lidar measurement, a lidar altitude and temperature vector could be used to recalculate the MLS geopotential and temperature profiles to help identify the source of this artefact.

It is also important to acknowledge that simply correcting for stratopause height offset was counter productive for our lidar-MLS comparisons above 50 km as seen in Fig. 3.14a. It is likely that any potential lidar-derived correction for MLS will

be more complex than a simple scalar offset. Such a correction may even have different functional forms in the stratosphere and mesosphere.

3.9.4 Seasonality of Temperature biases between OHP lidar and satellites

We have seen the 5 K difference between lidar-SABER stratopause temperatures which was reported in (V. Sivakumar et al., 2011) however, unlike this study we have found a clear seasonal dependence. We have correlated this temperature bias directly to a vertical displacement of the satellite altitude with respect to the lidar altitude and not with the Annual Oscillation. Further work must be done to explore the possibility of North Atlantic Oscillation/Annual Oscillation effects but a quick correlation of relative vertical displacement seen in Fig. 3.10 and a monthly average AO phase shows an R squared value of only 0.04 for SABER and 0.03 for MLS. There are isolated periods of up to a year where it seems like the correlations are significant however, it is clear that over a period of nearly a decade the AO phase and winter time stratospheric temperature anomaly are not correlated. The 5 K stratospheric warm bias was attributed to tides in (Yue et al., 2014) however, this explanation cannot explain the seasonal nature of this bias found in this work nor explain why a simple vertical displacement of the satellite stratopause height offers a suitable correction.

3.10 Conclusions

We can draw the following conclusions from the comparison of the lidar and satellite temperature measurements.

- 1) We have found the same systematic 5-15 K warm bias in the lidar-satellite comparisons above 70 km found in studies like (García-Comas et al., 2014b), (Taori, Dashora, et al., 2011), (Taori, Kamalakar, et al., 2012), (Taori, Jayaraman, et al., 2012), (Dou et al., 2009), (Remsberg et al., 2008), (Yue et al., 2014), (Dawkins et al., 2018), and (V. Sivakumar et al., 2011). We have attempted to carefully account for the the background-induced warm bias in high altitude Rayleigh lidar

temperatures. We believe that the algorithm set out in the companion publication (Robin Wing et al., 2018a) is robust and accounts for many of the uncertainties in the lidar initialization process. However, we are as yet unable to determine to what extent the a priori estimate warms the lidar temperature retrieval at these heights.

2) We have seen a layered summer stratosphere-mesosphere cold bias in lidar-MLS seasonal temperature comparisons with peak differences at 37 km, 50 km, and 65 km. There is nothing in the lidar data or retrieval algorithm which could account for this structure. The results of this study will be useful for any future satellite validation studies in the style of (Schwartz et al., 2008) where lidar data could be used as a reference dataset. In particular, lidar - satellite bias study results are useful for the ongoing NASA project "The Mesospheric and Upper Stratospheric Temperature and Related Datasets" (MUSTARD) which seeks to merge historic and ongoing satellite datasets.

3) The persistent summertime cold bias between the lidar and SABER results from a disagreement in the thermal lapse rate above and below the stratopause which is independent of the scalar stratopause height offset. Given that lapse rate is a fundamental geophysical parameter further work must be done to explore possible errors in vertical resolution and altitude definition.

4) The periods of greatest lidar-satellite temperature disagreement are found during times when the middle atmosphere is highly disturbed. In particular, the amplitude of stratospheric warming events can be underestimated and features like double stratopauses can be missed in the satellite measurements.

We have shown that ground based lidars can provide reliable and consistent temperature measurements over decades. This kind of high vertical resolution temperature database is useful both as a validation source for other instruments as well as for fundamental geophysical research.

4 A new MesosphEO dataset of temperature profiles from 35 to 85 km using Rayleigh scattering at limb from GOMOS/ENVISAT daytime observations

1

4.1 Author Contribution

Robin Wing contributed the validation of the GOMOS temperature profiles using the OHP Rayleigh lidar temperature profiles. By using data selection algorithms and statistical tools for lidar developed in chapters 2 and 3 he tested both the validity of the GOMOS temperature profiles as well as the general applicability of his technique beyond comparisons with SABER and MLS. The majority of this contribution is presented in Sect. 4.6. Robin Wing was also involved in the discussion and selection of the lidar-satellite co-incidence criteria as they relate to the section on tidal analysis.

¹Hauchecorne, A., Blanot, L., Wing, R., Keckhut, P., Khaykin, S., Bertaux, J.L., Meftah, M., Claud, C., and Sofieva, V. (2018). *A new MesosphEO dataset of temperature profiles from 35 to 85 km using Rayleigh scattering at limb from GOMOS/ENVISAT daytime observations*. Atmospheric Measurement Techniques, European Geosciences Union, 2018, pp.(Under Review).

4.2 Relation to Thesis Questions

Chapter 2 presented a series of algorithm changes to the traditional lidar temperature retrieval technique which are primarily focused of improving the retrievals above 70 km. One of the key motivations for making these changes was to minimise the systematic temperature bias which exists between ground based remote sensing instruments and their space based counterparts in the UMLT. Figure 2.11 shows the net cooling of the lidar temperature profiles resulting from the changes proposed in this paper. We can account for 20 K of the initial 33 K difference between the original NDACC algorithm and the temperatures from SABER at 90 km. However, further cooling of the lidar temperatures in this region by algorithm modification and noise filtering is not recommended. In order to further increase the retrieved lidar relative densities (and cool the resulting lidar temperatures) in this region we would be forced to make unrealistic assumptions regarding our noise or artificially distort our raw lidar photon counts profile. As a result of the work done in chapter 2 as well as the further exploration of lidar to satellite temperature biases done in chapter 3, we concluded that there were several possible sources of error that could contribute to the residual lidar warm bias with respect to the satellite:

1. Residual a priori errors in the lidar temperatures resulting from the classical frequentist approach (classical non-Bayesian statistics).
2. Geo-spatial and sampling errors associated with the number of co-incident satellite overpasses in the comparison region.
3. Offsets and vertical distortions in the pressure based geopotential height vectors of both MLS and SABER.
4. Tidally induced biases related to temporal offset between the lidar measurement and the satellite overpass.

4.2.1 Addressing Uncertainties in A Priori and Sampling

As was concluded in chapter 2, we have, to the best of our ability, minimised the contribution of initialisation related biases in the lidar temperature retrieval.

Further efforts may be possible by taking a Bayesian approach to the lidar retrieval similar to the work presented by (R. Sica and Haefele, 2015). In section 3.5 we outlined the rationale for our latitude and longitude range choices based on satellite orbital cadence, assumptions about of latitudinal temperature variation, and the sampling rate for coincident measurements. Subsequent sensitivity studies by (Dawkins et al., 2018) concluded that our choice of geo-spatial coincidence was unlikely contribute to sampling bias. However, in chapters 2 and 3 we were unable to properly account for contributions due to altitude shifting and distortion, and effects resulting from atmospheric tides.

4.2.2 Addressing Uncertainty in Geopotential Height

GOMOS is a star occultation experiment (method outlined in section 4.5.1) as opposed to MLS and SABER which are spectral radiometers. This means that MLS and SABER derive their geopotential altitude data using the thermal and microwave emissions of specific molecules over a specified atmospheric volume. These molecular emission measurements are then combined with similar measurements from adjacent channels and are inverted to infer a relative pressure profile. These relative pressure profiles are then normalised at some point in the lower atmosphere (nominally 100 hPa) where the signal to noise ratio is high. The pressure profile can then be converted to geopotential altitude by the Hyposometric Equation for a dry atmosphere 4.1 where Φ_1 and Φ_2 are two geopotential layers, R_d is the dry gas constant, g_0 is the gravitational acceleration at sea level, \bar{T} is the mean dry temperature, and P_1 and P_2 are two relative pressure levels.

$$\Phi_1 - \Phi_2 = \frac{R_d}{g_0} \int_{P_2}^{P_1} \bar{T} \frac{dP}{P} \quad (4.1)$$

Geopotential height, Φ is later converted to geometric height 4.2 for comparison with the lidar measurements by assuming a vector for gravitational acceleration as a function of latitude and geometric altitude.

$$\Phi(h) = \int_0^h g(\phi, z) dz \quad (4.2)$$

There are two main sources of error in this approach. The first involves the uncertainty associated with the pointing of the radiometers aboard the satellite. For example, the MLS data quality reference document estimates the uncertainty in the accuracy of the geopotential height due to uncertainty in pointing/field-of-view, uncertainty in spectroscopic parameters, and retrieval numerics to be on the order of 100-150 m in the lower atmosphere (N. Livesey et al., n.d.). It is reasonable to expect greater uncertainty at higher altitudes. As a result of this type of uncertainty in satellite geometry, there exists the possibility of vertical shifting and distortion in the calculated geopotential vector. In addition, the MLS data quality document shows evidence of a small seasonal temperature bias and a calibration drift in the initial years of the instrument. The second source of uncertainty arises from the inversion algorithm and forward model used to convert spectral radiance from target gasses into profiles of temperature as a function of pressure. Continuing to use MLS as an example, a single scan from the ground to 90 km is conducted in roughly 20 seconds and radiance is measured every 1/6 of a second. Many scans comprising multiple radiance profiles are assimilated into the forward model and are inverted to produce a relative pressure profile. Given that in any Bayesian inversion calculation there exists some necessary a priori information, some gain matrix, and some averaging kernels, there exists the possibility that some approximations may distort the resulting profile when the signal to noise ratio is low. This is particularly the case for small artefacts having a 'flat' spectral shape having a cumulative effect on the data matrix and the associated variances. As an additional complication, the satellites do not have an external calibration source for altitude/pressure for most of the atmospheric column. For tropospheric work they may use in situ radiosonde data but above 25 km they rely exclusively on model generated pressure-altitude conversions.

Section 4.5.1 lays out the methods for the GOMOS temperature retrieval. The differences in measurement technique address several of the outstanding concerns we have raised so far. First, GOMOS measure light from a calibration star and a star being occluded by Earth's atmosphere and thus, has none of the calibration related errors associated with radiometric instruments. Second, GOMOS makes tangent point measurements meaning that altitude is directly determined geometrically and there are no errors associated with the radiance-pressure-geopotential-altitude chain we have described. Third, the technique for deriving temperatures is very

similar to the Rayleigh lidar algorithm 2.1 and does not have the associated uncertainties of a Bayesian technique. As well, this makes GOMOS temperatures more directly comparable to the Rayleigh lidar temperature profiles and will help us to discriminate sources of potential bias when comparing ground based observations and space based observations.

4.2.3 Addressing Uncertainty from Tides

Both GOMOS and MLS sun synchronous satellites which means that they make measurements near OHP at nearly the same time every day. For GOMOS the orbit crosses into the geographic region shown in figure 3.1 around 11 am local time while MLS overpasses occur near 1:30 am. SABER has a precessing orbit with a 60-day yaw cycle and can pass through our study region at different times of the day and night. As a result we are able to apply a tight ± 4 hour window about the lidar measurement which ensures that the SABER measurements used in our study occur during or relatively soon before or after the lidar measurements. Our temporal coincidence criteria were designed to minimise the possible effects resulting from the 12 hour, 8 hour and 6 hour harmonics of the diurnal tides.

Atmospheric tides are primarily driven by solar heating of the atmosphere and have a primary period of 24 hours corresponding to the length of a solar day. The solar energy is primarily absorbed in the lower atmosphere by water vapour and in the stratosphere by ozone and can cause local perturbations in atmospheric pressure and density. Given the exponential decrease in atmospheric density with increasing altitude, small perturbations caused by solar warming in the lower atmosphere can grow rapidly in size as they propagate upwards. When these waves reach the mesosphere they can have a substantial amplitude and affect a large change to the mean atmospheric state.

The presence of these solar driven tides is a possible confounding variable when we compare our nightly average lidar temperature profiles to temperature profiles from MLS, which occur after the lidar measurement is made, and GOMOS which are made during the day. In the following section we have conducted a tidal analysis for the summer time at mid-latitudes which is a good climatological approximation of the mean tidal perturbations as a function of solar hour. Given that the orbits for both sun synchronous satellites are only a few hours apart this exercise can be

applied to the results from MLS seen in chapter 3 as a partial explanation for the observed temperature biases.

4.3 Abstract

Given that the scattering of sunlight by the Earth's atmosphere above 30-35 km is primarily due to molecular Rayleigh scattering, the intensity of scattered photons can be assumed to be directly proportional to the atmospheric density. From the measured relative density profile it is possible to retrieve an absolute temperature profile by assuming local hydrostatic equilibrium, the perfect gas law, and an a priori temperature from a climatological model at the top of the atmosphere. This technique is applied to Rayleigh lidar observations for over 35 years. The GOMOS star occultation spectrometer included spectral channels to observe daytime limb scattered sunlight close to the star direction. GOMOS Rayleigh scattering profiles in the spectral range 420-480 nm have been used to retrieve temperature profiles in the altitude range 35-85 km with a 2-km vertical resolution. A database of more than 309,000 temperature profiles has been created.

A global climatology was built and compared to GOMOS external model. In the upper stratosphere, where the external model is based on ECMWF analysis, the agreement is better than 2 K. In the mesosphere, where the external model follows MSIS climatology, 5 to 10 K differences are observed. Comparison with nighttime collocated Rayleigh lidar profiles above south of France shows some differences with a vertical structure that may be at least partially explained by the contribution of thermal diurnal tide.

The temperature evolution obtained at Equator indicates the occurrence of mesospheric inversion layers in the temperature profile with global longitudinal extension, descending in about one month from 80 to 70 km. The climatology shows a semi-annual variation in the upper stratosphere, a stratopause altitude varying between 47 and 54 km and an annual variation in the mesosphere. The technique to derive temperature profiles from Rayleigh scattering at limb can be applied to any other limb-scatter sounder providing observation in the spectral range 350-500 nm. This is also a good candidate for a future small satellite constellation due to the simplicity of the principle.

4.4 Introduction

The middle atmosphere (MA: stratosphere and mesosphere, 12 to 90 km altitude) is a transition region between the troposphere, which is heavily influenced by anthropogenic activity, and the upper atmosphere (thermosphere and ionosphere) at the edge of the space and strongly impacted by solar activity. The MA is a unique environment for fundamental research as it is subject to the conjugated influence of climate change, due to anthropogenic activities, and natural solar driven variability.

The increase of GHGs (GreenHouse Gases) induces a global warming at the surface and in the troposphere but also a global cooling in the MA (e.g. (P. Keckhut, W. Randel, et al., 2011)) induced by the thermal infrared radiation emitted by GHGs escaping directly to the space due to the low optical thickness of the atmosphere above.

The mesosphere is a region where temperature and wind observations are sparse or not well resolved. Recent studies have demonstrated the role of MA dynamics in both tropospheric weather and climate ((Baldwin and Dunkerton, 2001); (Shaw, Perlwitz, and Weiner, 2014); (Charlton-Perez, Ferranti, and Lee, 2018)). Weather and climate-chemistry models are currently moving towards a more comprehensive representation of the MA ((Beagley et al., 2000); (Baldwin and Dunkerton, 2001); (Hardiman et al., 2010)). Atmospheric observations in this region can also be used as a benchmark for climate change studies due to its high sensitivity to the increase of GHGs and to the external solar forcing. Furthermore several applications, such as e.g. the re-entry of space and sub-orbital vehicles, the impact of meteors on the atmosphere and infrasound propagation modelling in the atmosphere, are dependent on the good knowledge of the mesospheric mean state and variability at different scales.

The MA temperature is insufficiently observed above the top altitude of radiosoundings, about 30 km. GNSS (Global Navigation Satellite System) Radio-Occultation technique provides accurate measurements of temperature up to about 35 km with high vertical resolution. Nadir viewing satellite sensors observing in the thermal infrared (SSU: Stratospheric Sounder Unit) and microwave (AMSU: Advanced Microwave Sounding Unit) spectrum provide brightness temperature up to the upper stratosphere (around 45 km) but with very broad vertical weighting

functions (≈ 10 km). These are the only temperature observations assimilated in NWP (Numerical Weather Prediction) models. Limb viewing satellite sounders, e.g. MLS (Microwave Limb Sounder on the Aura satellite) and SABER (Sounding of the Atmosphere using Broadband Emission Radiometry on the TIMED mission), provide temperature profiles up to the upper mesosphere with a good vertical resolution. However these data are not assimilated in NWP models because these instruments are not part of operational meteorological satellite.

The scattering of sunlight (near UV and visible wavelengths) by the Earth atmosphere above the top of the stratospheric layer, about 30-35 km altitude, is only due to Rayleigh scattering by atmospheric molecules. Its intensity is directly proportional to the atmospheric density. It is thus possible to retrieve a temperature profile in absolute value using the hydrostatic equation and the perfect gas law. The temperature is initialised at the top of the profile from a climatological model. This technique has been applied to Rayleigh lidar observations since more than 35 years (Alain Hauchecorne and M.-L. Chanin, 1980a). Rayleigh lidars operated in NDACC (Network for the Detection of Atmospheric Composition Changes) obtain local observations of the temperature profile between 30 and 80-90 km with a good accuracy and vertical resolution, but in less than 10 locations worldwide. They have been used for trend analysis ((Alain Hauchecorne, M.-L. Chanin, and P. Keckhut, 1991); (P. Keckhut, A. Hauchecorne, and M. Chanin, 1995); (Li et al., 2011)) and or validation of satellite data and identification of possible biases and trends due to orbital changes and instruments ageing ((Funatsu, Claud, Philippe Keckhut, and Alain Hauchecorne, 2008); (Philippe Keckhut, Funatsu, et al., 2015); (Funatsu, Claud, Philippe Keckhut, Alain Hauchecorne, and T. Leblanc, 2016)).

The observation from space of the Rayleigh scattering at atmospheric limb during daytime may be also used to derive density and temperature profiles in the UMLT. This technique has been applied by (Clancy, Rusch, and Callan, 1994) who derived temperature profiles from 40 to 92 km for the period 1982-1986 using Solar Mesosphere Explorer bright limb observations at 304, 313 and 442 nm. (M. G. Shepherd et al., 2001) determined temperature profiles from 65 to 90 km during the period March 1992 - January 1994 analysing WINDII/UARS data at 553nm. More recently (Sheese et al., 2012) retrieved temperature profiles using OSIRIS/Odin bright limb observations at 318.5 and 347.5 nm in the altitude range 45-85 km. In the frame of the ESA funded Mesospheric project, a new dataset of temperature profiles in the altitude range 35-85 km was created from the analysis

of GOMOS/ENVISAT bright limb observations in the spectral band 420-480 nm. A dataset of more than 309,000 profiles from June 2002 to April 2012 is available for climatology and atmospheric dynamics studies.

The paper is organised as follows. In Section 4.5, the principle of the method is explained and the data processing is described. Section 4.6 is dedicated to the validation against Rayleigh lidar observations. Section 4.7 presents the first scientific results with a focus on the evolution of equatorial temperature profiles. Finally, a summary is given in Sect. 4.8.

4.5 Principle and data processing

4.5.1 Method

GOMOS (Global Ozone Monitoring by Occultation of Stars), on board the European Space Agency ENVISAT (ENVIRONMENTAL SATellite) platform, was the first operational space instrument dedicated to study the middle atmosphere by the technique of stellar occultations. A description of the instrument as well as an overview of the main scientific results is given in (Bertaux et al., 2010). GOMOS observed the spectrum of a star during its occultation by the atmosphere. The atmospheric transmission spectrum is equal to the ratio between the star spectrum absorbed by the atmosphere and the reference star spectrum measured outside the atmosphere. Atmospheric constituents are identified by their absorption spectral features. As the reference spectrum is measured at the beginning of each occultation, we can consider GOMOS as a self-calibrated instrument, independent of any radiometric calibration. Furthermore the stellar occultation technique allows a perfect knowledge of the tangent altitude, depending only on the geometry of the light path between the star and the satellite. The 250-680 nm spectral domain is used for the determination of O₃, NO₂, NO₃ and aerosols from the upper troposphere to the mesosphere (Kyrölä et al., 2010). In addition, two high spectral resolution channels centred at 760 and 940 nm allow measuring respectively O₂ and H₂O. In order to remove the background signal due to the sunlight scattered by the atmosphere, two background spectra are observed just above and below the location of the star, referenced as upper and lower spectra. In this study we use

only these background spectra during daytime (bright limb occultations). Bright limb spectra have been used to derive vertical profiles of ozone during daytime (Tukiainen et al., 2011). Here we use for each daytime occultation the vertical profile of bright limb light averaged over three 20 nm spectral bands, 420-440 nm, 440-460 nm and 460-480 nm in the upper and lower background spectra. Above about 35 km, the scattering of the sunlight by the stratospheric aerosol layer is negligible and the signal at 420-480 nm is only due to the Rayleigh scattering by atmospheric molecules and, hence, directly proportional to the atmospheric density (at these wavelengths ozone and other trace gases absorption is negligible). Figure 4.1 shows an example of scattering profile at limb in the 3 spectral bands. The decrease of the Rayleigh scattering signal due to the exponential decrease of the atmospheric density is seen up to about 70 km. Above this altitude the contribution of the measurement noise becomes more important but the Rayleigh signal can be exploited up to at least 90 km after removing this noise.

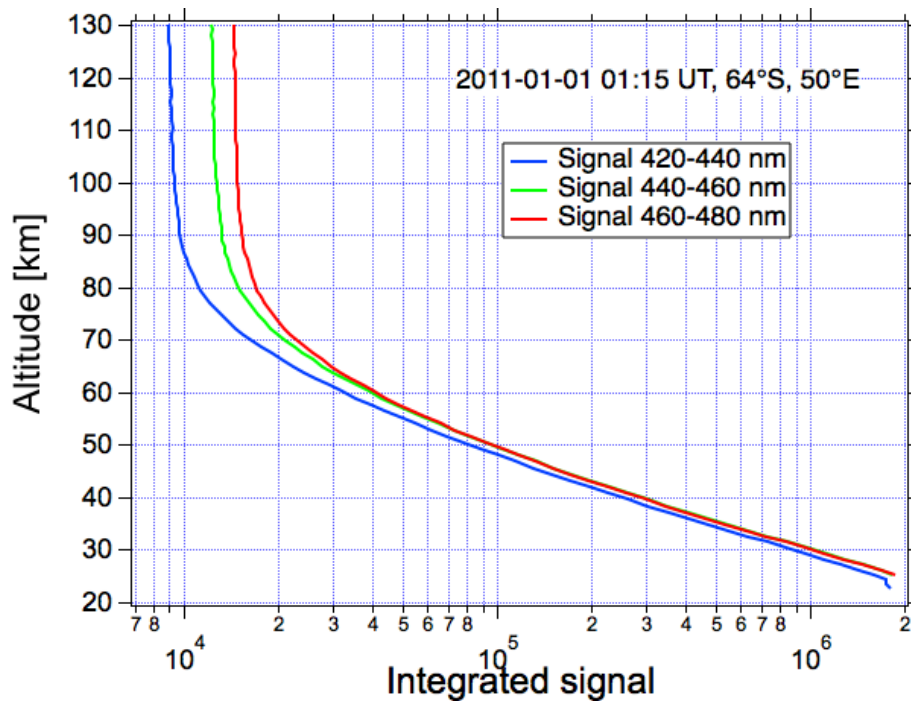


FIGURE 4.1: Spectrometer signal integrated in the three 20-nm spectral ranges for one occultation on 1st January 2011 (star ID =3, orbit number = 46209), lower background spectrum.

Data processing

For this study we used the full Level 1 GOMOS database between June 2002 and April 2012 containing 418,000 bright limb occultations. A screening is made to keep only data exploitable to retrieve temperature profiles:

- Occultations with a solar zenith angle larger than 84° are eliminated to avoid spectra with too much absorption between the sun and the limb.
- Profiles, which do not cover the altitude range between 35 and 125 km, are not considered. The lower limit is set to retrieve a temperature profile covering the full altitude range 35-85 km and the upper limit is set to have

enough data at the top of the profile to estimate correctly the measurement noise.

- Occultations with the presence of Polar Mesospheric Clouds (PMCs) are also removed. PMCs detection is based on the algorithm described by (Pérot et al., 2010). After this screening 309341 occultations are selected.

Processing one occultation

For each spectrum the signal is integrated in the upper and lower background bands of GOMOS spectrometer A2 (400-680 nm) in 3 spectral ranges, 420-440 nm, 440-460 nm and 460-480 nm to obtain 6 profiles versus tangent altitude. After removing the noise contribution (stray light and detector noise), estimated at altitudes higher than 110 km and extrapolated at lower altitude, a vertical inversion is performed using an onion peeling method. The resulting 6 profiles of Rayleigh scattering versus altitude are assumed to be proportional to the atmospheric density. The algorithm to retrieve temperature profiles is very similar to Rayleigh lidar algorithm described in details in (R. Wing, A. Hauchecorne, P. Keckhut, Godin-Beekmann, S. Khaykin, McCullough, et al., 2018). The temperature is computed by downward integration of the hydrostatic equation 2.4 assuming the perfect gas law 2.5 where z is the altitude, P is the pressure, T the temperature, ρ the atmospheric density, g the gravity, R the perfect gas constant ($R=287.06 \frac{J}{K \cdot kg}$) and M the air molar mass ($M=28.96 \frac{g}{mol}$). The initialisation of the pressure at the top of the profile is made at about 95 km assuming that the mean temperature in the layer 85-95 km is equal to the temperature of the NRLMSISE-00 climatological model (Picone et al., 2002). For each occultation, 6 individual temperature profiles are retrieved corresponding to 3 selected wavelength intervals and upper and lower panels Fig. 4.2. For the following, we use only the median profile as a temperature profile corresponding to this occultation, and the dispersion (1 standard deviation) interval of the 6 individual profiles) as an estimation of the its uncertainty.

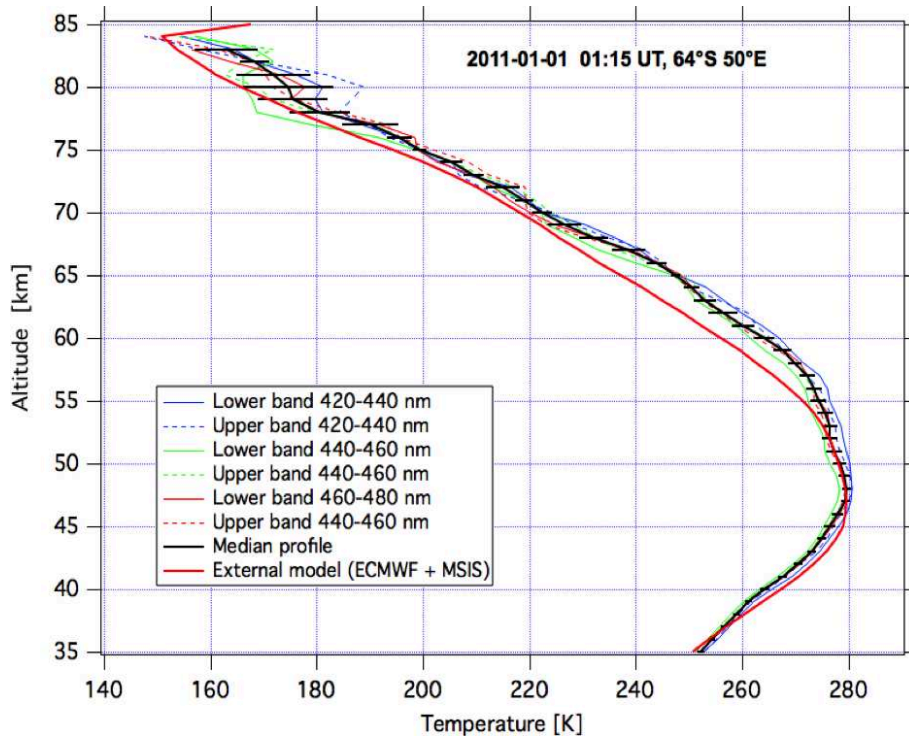


FIGURE 4.2: Temperature profiles processed for the same occultation as in Fig. 4.1. The horizontal bar indicates the dispersion (1 standard deviation) between the 6 individual profiles.

4.6 Validation using Rayleigh lidar observations

A validation exercise has been made using the Rayleigh lidar located at Observatoire de Haute Provence (OHP; 43.9° N, 5.7° E). This lidar has been part of the Network for Detection of Atmospheric Composition Change (NDACC; <http://www.ndsc.ncep.noaa.gov/>) since its creation in 1991 and has participated in several satellite validation experiments for instruments on board UARS satellite ((Fishbein et al., 1996); (Gille et al., 1996); (Hervig et al., 1996); (Singh et al., 1996b); (Wu et al., 2003); (Philippe Keckhut et al., 2004b)), and more

recently for MLS-Aura and SABER-TIMED (R. Wing, A. Hauchecorne, P. Keckhut, Godin-Beekmann, S. Khaykin, and McCullough, 2018a). For the present study GOMOS profiles were selected in a geographical region around OHP (40° N, 9° E); (48° N, 21° E). Night-mean lidar profiles smoothed down to a 3-km vertical resolution were used for the comparison. A maximum of 12h difference between GOMOS and lidar measurements was accepted for the time coincidence. When several GOMOS profiles reached the coincidence criteria, as shown in Fig. 4.3, the median profile was used for the statistical comparison.

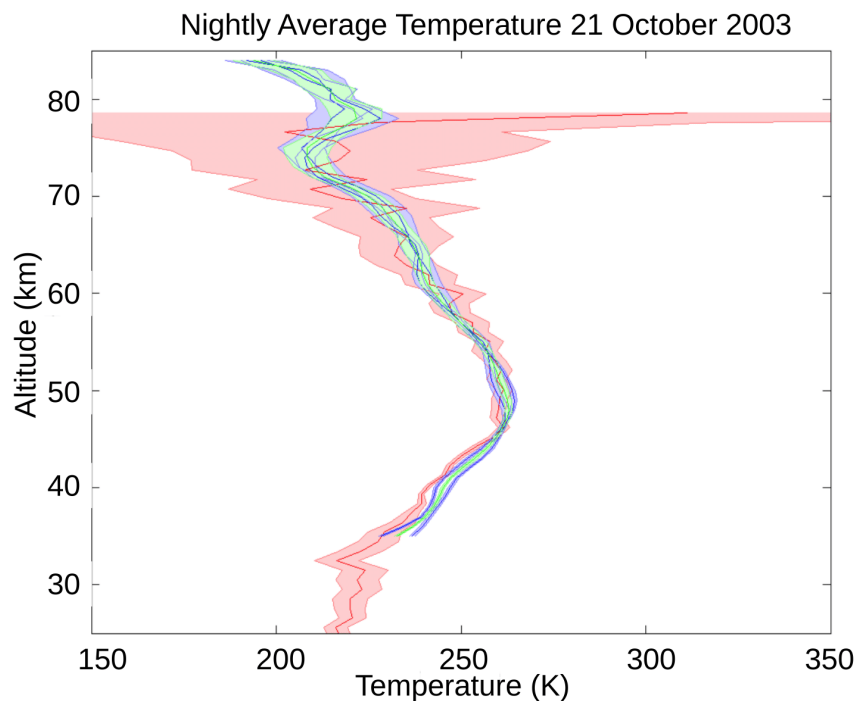


FIGURE 4.3: Example of comparison between a Rayleigh lidar profile at OHP on 21st October 2003 (in red) and two collocated GOMOS profiles selected using the co-location criteria (in blue and green). When two or more GOMOS profiles are selected, the median profile is used for the statistical comparison. For the lidar profile (red), each individual GOMOS profile (blue) and the median GOMOS profile (green), the standard deviation of its uncertainty is represented by the shaded area.

The statistical median difference between OHP lidar and GOMOS temperature (Fig. 4.4) is close to zero below 46 km, negative between 46 and 73 km with down to -5 K between 55 and 60 km and again positive above 73 km with up to +7 K at 85 km. The dispersion of the differences stays between ± 5 K and ± 1 K in the full altitude range. The positive difference in the upper part of the profile may be at least partially due to a warm bias in OHP temperature above 75 km as reported by (R. Wing, A. Hauchecorne, P. Keckhut, Godin-Beekmann, S. Khaykin, and McCullough, 2018a) using a comparison with SABER-TIMED. The alternation of positive and negative differences with altitude may indicate a contribution of atmospheric thermal tides, as temperature measurements are not obtained simultaneously. This effect has been already observed when comparisons involved measurements obtained at different solar time (Wild et al., 1995); (Philippe Keckhut, Gelman, et al., 1996); (Philippe Keckhut, Funatsu, et al., 2015)). GOMOS measurements above OHP are performed during daytime at around 11:00 am solar time while lidar operations are conducted during the first part of the night for several hours, with an estimated mid-sequence around 21:00 solar time in average.

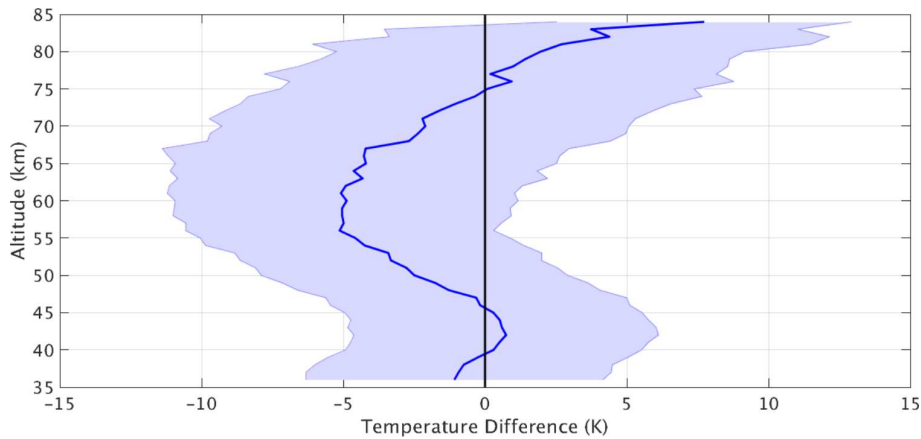


FIGURE 4.4: Statistical median temperature difference between OHP lidar and GOMOS temperature profiles (lidar minus GOMOS temperature). The shaded area represents the dispersion of the differences (one standard deviation).

To evaluate the potential effect, tidal characteristics above the lidar site have been extracted from the Global Scale Waves Model (GSWM; (Hagan et al.,

1999)). The model has been optimised to provide the migrating thermally forced tides on a global scale throughout the atmosphere on a monthly mean basis. The amplitude and phase of the diurnal and the semi-diurnal components can be calculated from the outputs of the GSWM-00 tidal model (<http://www.hao.ucar.edu/modeling/gswm/gswm.html>), which is an extension of the GSWM-98 (Hagan et al., 1999). Such a model has been compared with many observations. While the vertical shape of the observations is well reproduced with this model, the amplitude is often smaller as reported by (Raju et al., 2010). In this study, the amplitude (Fig. 4.5, left panel) and the phase (Fig. 4.5, middle panel) of the diurnal component of the tides have been extracted from the GSWM for the 45°N latitude for August and middle panels). In the summer period and in the middle atmosphere diurnal component is the dominant one. The expected difference between lidar and GOMOS temperatures is represented in Fig. 4.5, right panel. In the middle mesosphere we observe a +3 K difference while in the vicinity of the mesopause, we note a reverse effect of -3 K. The expected tide contribution does not fully reproduce the observed temperature difference between the OHP lidar and GOMOS but, considering uncertainties associated with the amplitude and phase of the tidal effect, and the fact that non-migrating tides were not taken into account, it appears that at least some part of the observed differences may be explained by local time differences. Further work would be needed to confirm this hypothesis.

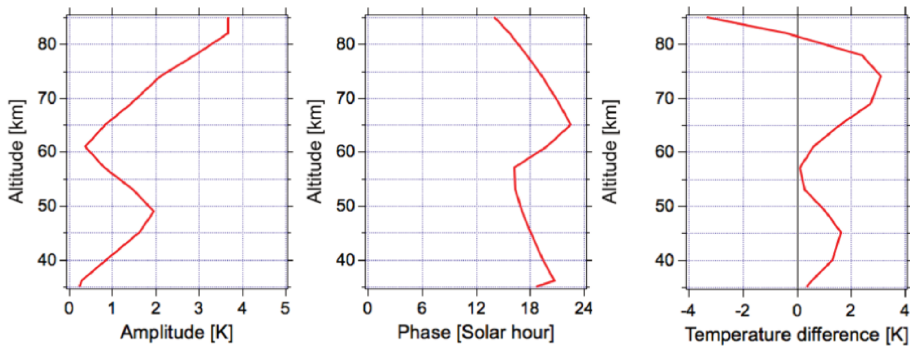


FIGURE 4.5: Amplitude (left panel) and phase (time of the maximum temperature; right panel) of the diurnal tides extracted from the GSWM above 45°N for August. Temperature differences (lidar minus GOMOS; right panel) expected from diurnal atmospheric tides as simulated by the GSWM-00 model.

4.7 First scientific results

The monthly climatology of GOMOS temperature has been built by averaging the data into 10° bins from 80°S to 80°N . For each month-latitude bin, the average value is kept only if at least 15 valid profiles are considered. The results are presented in Fig. 4.6. At the stratopause the warmest temperatures are observed at the North Pole from April to September and at the South Pole from November to January, the equatorial stratopause temperature showing relative maximum all around the year. As expected, the coldest temperatures are observed in the upper mesosphere at high latitudes in summer, from May to August in the North hemisphere and from November to February in the South hemisphere. This is due to adiabatic cooling of ascending air in this configuration.

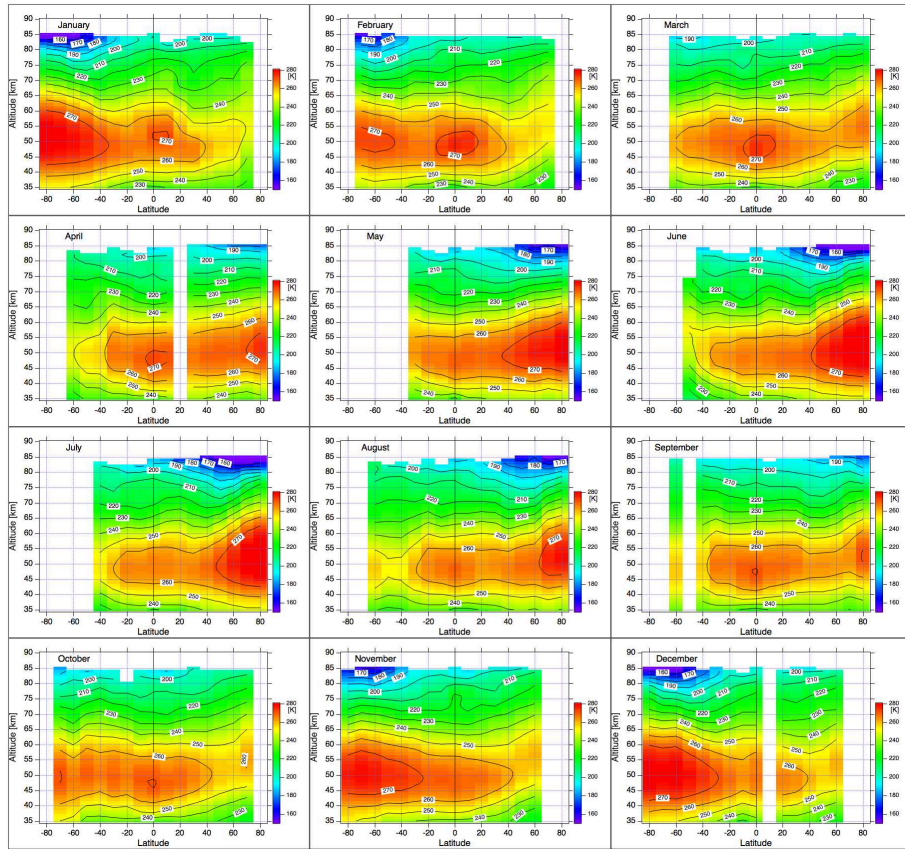


FIGURE 4.6: Monthly climatology of GOMOS Rayleigh temperature. Data are averaged over 10° latitude bins.

In order to better visualise the main features of the GOMOS climatology, the temperature difference with the GOMOS external model is represented in Fig. 4.7. The GOMOS external model is used for processing of GOMOS data for the retrieval of atmospheric species as described by (Kyrölä et al., 2010). For each occultation the external atmospheric profile is built by using ECMWF analysis up to 1 hPa (about 48 km) with a smooth transition to NRLMSISE-00 climatological model above 1 hPa, preserving the hydrostatic equilibrium at all altitudes.

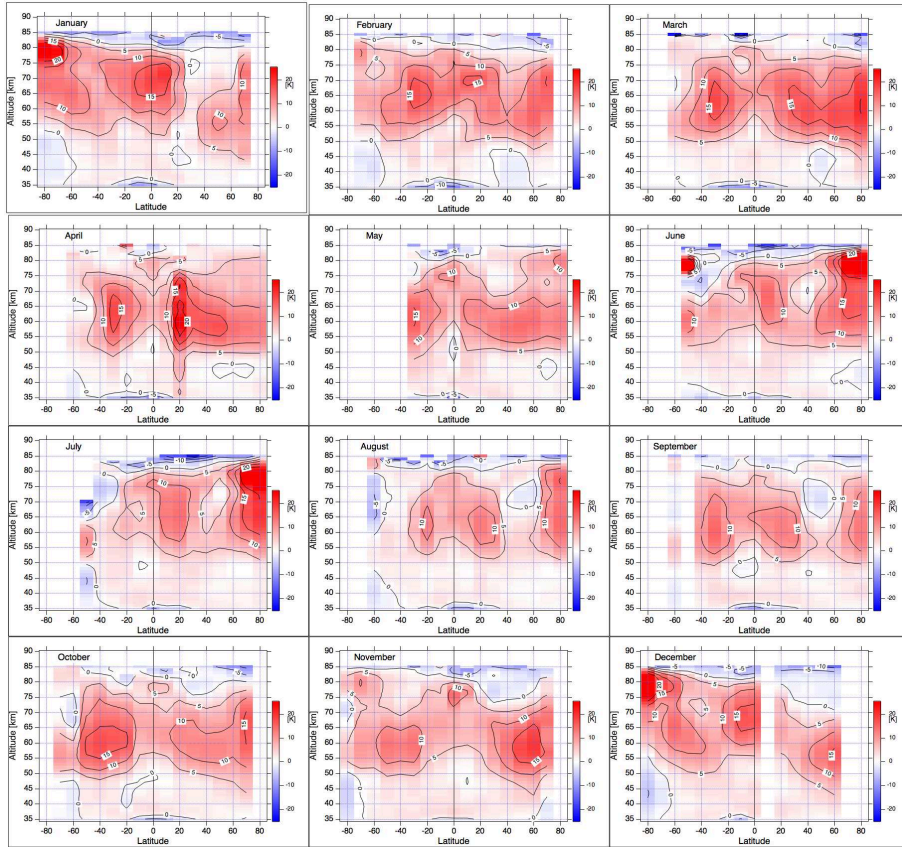


FIGURE 4.7: Monthly climatology of the temperature difference between GOMOS and the external (ECMWF+MSIS). Data are averaged over 10° latitude bins.

Figure 4.8 shows the average temperature difference between GOMOS and the external model averaged over all latitudes and months. Below 48 km, where the external model is based on ECMWF analysis, the agreement is very good, almost always better than 5 K and in average better than 2 K. The only exception is at 35 km in the equatorial region where GOMOS presents a cold bias compared to the model, especially from January to May (cold bias of about -10 K). We attribute this cold bias to a contamination of the Rayleigh scattering profile by Mie scattering due to the presence of aerosols in the lower stratosphere that may reach 35 km at the equator (Vernier et al., 2009). Above 48 km, where the external

model is driven by NRLMSISE-00, the temperature is warmer in GOMOS data than in the external model up to 80 km by up to +10 K in average at 60 km. Above 80 km GOMOS is colder than the external model.

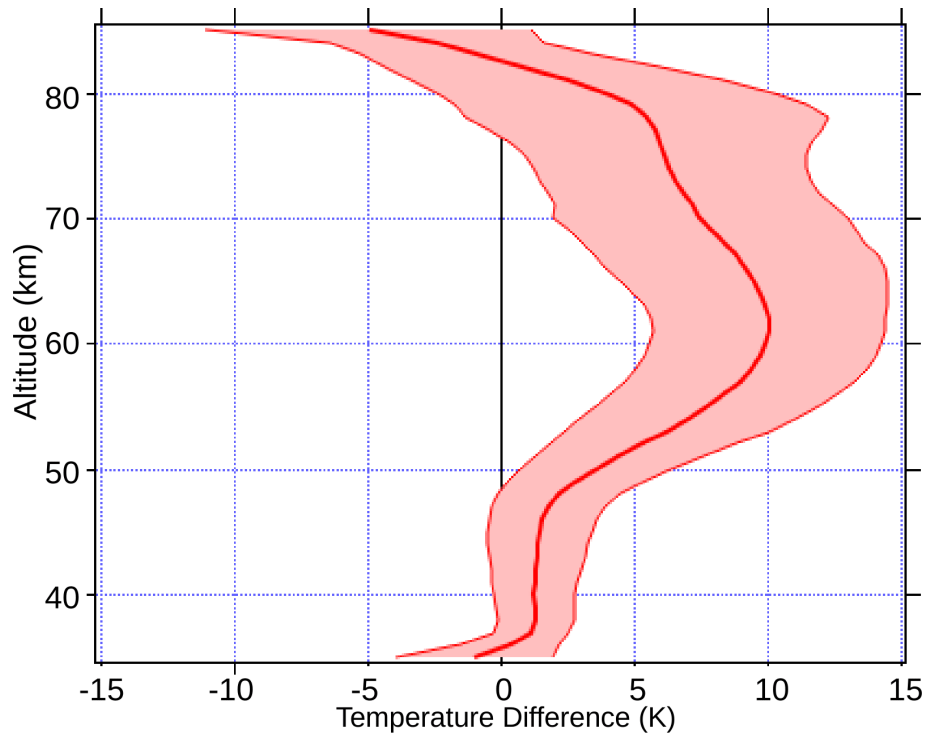


FIGURE 4.8: Mean difference between GOMOS Rayleigh temperature and external model temperature as a function of altitude. The standard deviation of the difference is shaded.

An interesting characteristic of the geometry of observation is that for a line of sight parallel to the Earth pole axis, the tangent point in the atmosphere is exactly at the Equator. The occultation of Polar Star, with 89.5° declination, gives all around the year a tangent point between 0.8°S and 0.8°N in bright limb conditions. More than 22,000 occultations of the Polar Star have been performed during the 10 years of ENVISAT life, providing a quasi-continuous survey of the temperature evolution at the Equator (Fig. 4.9, left panel). The temperature at the stratopause exhibits a semi-annual variation. In the mesosphere we observe the descent of cold layers

from 80 to 70 km in about 1 month. The more intense cold layers occurred in April-May 2007. The vertical profile during the first week of May ((Fig. 4.9, right panel) shows that this cold layer corresponds to a so-called mesospheric inversion layer (MIL) in vertical temperature profiles.

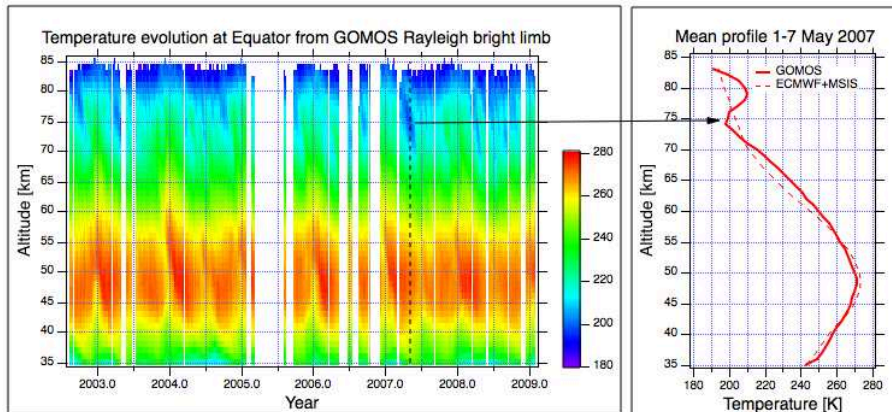


FIGURE 4.9: Left) Evolution of the weekly averaged temperature profile at Equator obtained using all occultations of the polar star with a tangent point latitude always situated in the interval 0.8°S - 0.8°N . Right) Vertical weekly mean profile beginning of May compared to the GOMOS external model.

MILs have been observed by rocketsondes (Schmidlin, 1976) and Rayleigh lidars at middle latitudes ((A. Hauchecorne, M. L. Chanin, and Wilson, 1987); (Duck et al., 2001)), high latitudes (Cutler et al., 2001) and low latitudes (Ratnam et al., 2003). Satellite observations showed the global extend of MILs ((T. Leblanc and Alain Hauchecorne, 1997); (Fechine et al., 2008); (Gan, Zhang, and Yi, 2012)). Several explanations have been proposed to explain the formation of MILs including gravity wave breaking ((Alain Hauchecorne and Maillard, 1990)), planetary wave structure (Salby et al., 2002) and thermal tides (Meriwether et al., 1998). Explanations of the long duration and the global longitudinal extend of the observed equatorial MILs are beyond the scope of this paper and will be the topic of a future publication.

Polar Star profiles have been used to build a seasonal climatology at the Equator Fig. 4.10. In the upper stratosphere the dominant feature is the semi-annual evolution with maxima at equinoxes (February to April and September-October) and minima at solstices (June-July and December). The altitude of the stratopause, taken at the altitude with warmest temperature, varies between 47 and 54 km during the year with a maximum in December-January, a secondary maximum in July. In the mesosphere the evolution is dominated by the annual variation with a maximum in December-January, corresponding to the period with an elevated stratopause, and a long minimum from April to October.

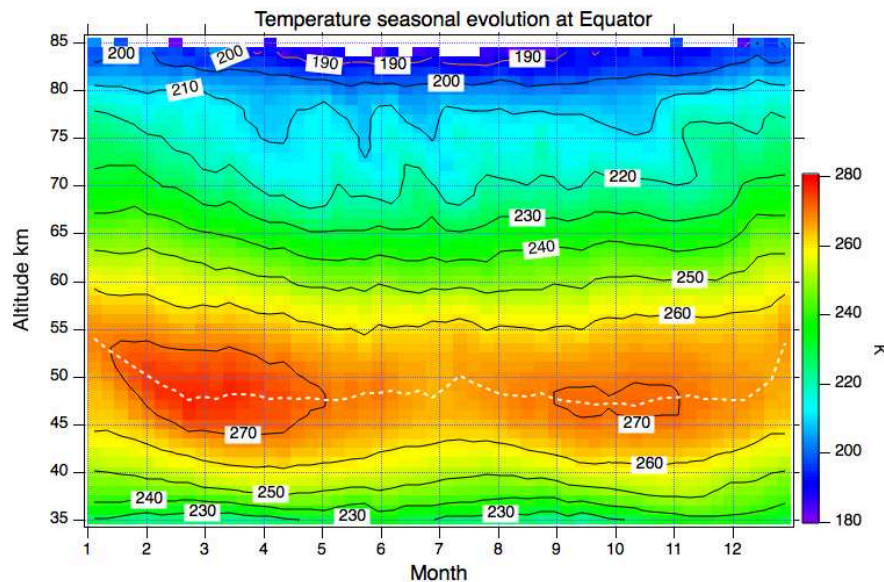


FIGURE 4.10: Seasonal evolution of the equatorial temperature derived from temperature data presented in Fig. 4.2 The altitude of the stratopause is indicated by the white dotted line.

4.8 Conclusions

A database of more than 309,000 temperature profiles from 35 to 85 km, covering the period June 2002 to April 2012, has been created in the frame of the ESA

funded MesosphEO project using the daytime Rayleigh scattering at limb observed by GOMOS.

Comparison with nighttime Rayleigh lidar profiles at OHP shows some differences with a vertical structure that may be at least partially explained by the contribution of thermal diurnal tides. This data set was used to build temperature climatology as function of latitude and month and to compare it with the GOMOS external model. The agreement is better than 2 K in the upper stratosphere below 48 km (1 hPa) where the model is driven by ECMWF, but 5 to 10 K differences are observed in the mesosphere from 50 to 80 km where the model follows NRLMSISE-00 climatology. The evolution of the temperature at Equator shows the occurrence of temperature MILs with global longitudinal extension, descending in about one month from 80 to 70 km. The climatology shows a semi-annual variation in the upper stratosphere, a stratopause altitude varying between 47 and 54 km and an annual variation in the mesosphere.

The technique to derive temperature profiles from Rayleigh scattering at limb can be applied to any other limb-scatter sounder providing observation in the spectral range 350-500 nm where the Rayleigh scattering is efficient and the absorption by ozone and other stratospheric constituents not too important. This is also a good candidate for a future small satellite constellation due to the simplicity of the principle.

5 General Conclusions and Future Work

5.1 Conclusions

In this work we have presented an improved algorithm which minimises the systematic temperature warm bias at the top of the lidar temperature retrieval. The bias in the lidar temperatures has been reduced by 20 K near 90 km as is represented in figure 2.11. The modification were made to the classic iterative technique of (Alain Hauchecorne and M.-L. Chanin, 1980a) and focused mainly of the improvements to signal to noise ratio reduction and background identification (see chapter 2.5). The techniques we have employed for the detection of signal contamination, the selection of the best data for inclusion in the calculation, and criteria for where to initialised the inversion when assuming an a priori pressure at the top of the atmosphere, are easily adaptable to other lidar systems. We hope that the suggestions presented here will be of help in the ongoing discussion of how to better NDACC lidar temperatures in the UMLT.

Having conducted the first ever decadal temperature inter comparison between a co-located 532 nm Rayleigh lidar and temperatures from the 355 nm Rayleigh line of an ozone DIAL system we have shown that these two techniques can produce statistically identical and robust temperature profiles over an extended time period as is seen in figure 2.14. Residual temperature differences between the two sets of temperature profiles is likely due to periods of internal or inter-system misalignment and underscores the need for an automated alignment system going forward. This should provide motivation for all NDACC DIAL systems to contribute temperature data products to the NDACC database.

The OHP lidars have been shown to be stable and consistently produce high quality temperature profiles over a period of four decades. After applying our new data processing techniques, we have seen a systematic cooling of the high-altitude lidar temperatures which brings them into better agreement with the temperatures

measured by both MLS and SABER. Additionally, these profiles are made at a high cadence, averaging two to five nightly average profiles per week allowing for statistically rigorous comparisons with other instruments. In particular, we would conclude that these improved lidars are ideal candidates for long-term validation of temperature profiles measured by satellites.

We have detected the same systematic 5-15 K warm bias in the lidar to satellite temperature comparisons above 70 km found by many other authors (described in section 3.3.2). Having addressed many of the issues concerning the initialisation of the lidar temperature profile using the integrative technique in Chapter 2 we are confident that our temperatures are not unduly influenced by noise, electrical transients or background and that the resulting temperature differences between the lidar and satellites is either indicative of systematic effects in the satellites or geophysical variation.

In total, 2433 nights of Rayleigh lidar temperatures from OHP were compared to 1741 temperature profiles from MLS (2004-2018) and 1100 temperature profiles from SABER (2002-2018). The comparisons were done in the geographical region surrounding OHP [(40° N, 9° E) to (48° N, 21° E)] using a time window of ± 4 hours for coincidence with a SABER orbit and ± 12 hours for a MLS orbit (refer to map 3.1).

In general, we found that the SABER to lidar temperature comparison has a seasonally dependent bias which varies with altitude. In the summer we determined that the SABER temperatures were approximately 2 K colder than the lidar temperatures in the upper mesosphere above 70 km, up to 6 K warmer than the lidar in the mesosphere (50 to 70 km), up to 3 K colder than the lidar in the stratopause region (40 to 50 km), and warmer than the lidar below 35 km. In the winter we determined that the SABER temperatures were approximately 4 K colder than the lidar temperatures in the upper mesosphere above 70 km, up to 3 K warmer than the lidar in the mesosphere (50 to 70 km), up to 6 K colder than the lidar in the stratopause region (40 to 50 km), and also warmer than the lidar below 35 km. These seasonal, altitude dependant biases are seen in figure 3.3. We concluded that the upper most bias could be due to lidar a priori choice but that further corrections are not possible using an iterative technique for lidar temperature estimation. The middle two regions from 40 to 70 km are where the lidar measurements and technique are most robust and we can not account for

the temperature differences from the ground based perspective. The lowest layer biases below 35 km are possibly due to aerosol contamination of the Rayleigh lidar or perhaps some non-linearity in the low gain channel. This problem will be resolved by the addition of a rotational Raman temperature channel to the OHP lidar in the near future. We theorised that the seasonal variation in the systematic bias could be due to improper estimation of the stratopause height in the satellite estimation of geopotential height.

After correcting for satellite geopotential height using the lidar data we redid the comparison between the SABER and lidar temperature profiles. The summer time showed statistically significant improvements between 35 and 70 km. The temperature bias in the mesosphere was reduced from 6 K to 3 K and is now characterised by a flatter shape as opposed to the “S” curve which dominated the uncorrected comparisons. The bias in the stratopause temperature was reduced to nearly zero from an initial peak of 3 K. Above 70 km and below 30 km the temperature differences are slightly larger after the altitude correction but the results are either small or not significant (see figures 3.14d). The winter comparison showed marked improvement after adjusting the satellite altitudes using the lidar determined stratopause height. In the region from 35 to 65 km, the bias was reduced to a nearly constant offset of 1 K with the almost no residual altitude dependence. No significant changes were found below 35 km or above 70 km (see figure 3.14f).

When repeating the satellite to lidar temperature comparison using temperature profiles from MLS we found a highly layered bias in the stratosphere and mesosphere that also varied with season and altitude. In the summer the lidar minus MLS temperature bias had an oscillating structure with local extrema at 25 km (-5 K), 37 km (4 K), 50 km (-2 K), 63 km (3 K), 70 km (-5 K), and 80 km (13 K). The winter temperature comparison shared the same general layered form as the summer comparison but had an even more extreme bias near the stratopause. In the winter we saw a systematic bias with local extrema at 25 km (-10 K), 37 km (17 K), 63 km (3 K), and 70 km (12 K). These extreme seasonal variations are presented in figure 3.5.

Correcting the MLS temperature profiles using the stratopause height as measured by the lidar had no significant affect on the temperature differences in the summer time comparison (see figure 3.14c). Likewise, the winter comparison saw no

meaningful improvement beyond a 5 K reduction near 50 km.

Based on the success of our technique in correcting the satellite temperature profiles using the lidar derived stratopause height as well as making qualitative observation for nightly comparisons during the winter (figure 3.9), we have concluded that both satellites often have difficulty identifying the altitude of layers with sharp temperature gradients such as the stratopause. In particular these instruments have difficulty during the winter when the middle atmosphere is more dynamic and rapid, wave-driven events such as sudden stratospheric warmings can be missed entirely.

We have used the lidar database which was assembled and tested in this work to validate the temperature retrievals from the newly derived temperature database from the GOMOS satellite. This is another example of the value of lidar as a ground based remote sensing instrument for middle atmospheric temperature.

5.2 Future Work

We are collaborating with colleagues from the UK Met Office to produce an analysis of NDACC temperature lidars, the MLS temperatures and the ERA-interim reanalysis model. The scope of this work is to use the ERA-interim pressure grid to compare the lidars, satellites and models and attempt to eliminate temperature differences which may be due to conversion errors in the geopotential height. Given the stability of the lidar temperature measurements and the utility they show as tools for validation of other measurements, the next logical step is to compare the lidar data to numerical weather predictions of the stratosphere. Given that the lidar data is not assimilated by the current weather prediction models they will provide a good independent reference in the effort to identify potential sources of error and bias.

We are also collaborating with colleagues in Canada who are using the Bayesian Optimal Estimation Method for temperature retrieval (R. Sica and Haeefe, 2015). We have calculated the averaging kernels for the OHP temperature lidar but we need to fully express the error contributions in the gain matrix for the OHP lidar. We are attempting to characterise the a priori error in the OHP temperature profiles to address one of the major sources of uncertainty we have left in our

temperatures. However, some challenges remain in the characterisation of the background and the selection of which profiles to include in the Bayesian forward model. I need to reconcile the work presented in Chapter 2 where I have relied on a frequentist approach to noise and background reduction with the new Bayesian techniques. The inclusion of several of my data quality processes into the Canadian lidar forward model may also help constrain data variances.

Chapters 2 and 3 represent the first two stages in presenting the temperature profiles from the OHP lidars as a valuable dataset for long-term geophysical and validation studies. We have raised some interesting questions about the resolution and identification of the stratopause in the temperature profiles from MLS and SABER which need further study. The next paper for the series is a study of temperature and geophysical trends in the middle atmosphere using the lidars, satellites, and models to identify the cause of the disagreements regarding stratopause shape and altitude. Given that we have 40 years of middle atmospheric lidar profiles we can also do a trend study to look at both temperature trends broadly as well as the altitude of the stratopause.

A Résumé Français

Des observations lidar de longue durée de l'atmosphère moyenne ont été effectuées depuis 1978 à l'Observatoire de Haute-Provence (OHP), situé dans le sud de la France (43.93° N, 5.71° E). Dans cette thèse, j'ai décrit la configuration technique actuelle des deux expériences lidar co-localisées à OHP. La première expérience est le lidar Rayleigh, Lidar Température et Aérosols (LTA), qui fonctionne à une longueur d'onde de 532 nm et mesure les profils verticaux de la densité atmosphérique, des aérosols et de la température. La deuxième expérience est le lidar pour l'Ozone dans la Stratosphère (LiO₃S), utilise deux longueurs d'onde à 355 nm et à 308 nm et mesure la densité, la température, les aérosols et l'ozone. En utilisant 20 années de mesures lidar co-localisées de haute qualité, nous avons montré que les températures lidar calculées à l'aide de la technique de Rayleigh au LTA à 532 nm sont statistiquement identiques aux températures lidar calculées à partir du voie non absorbant à 355 nm de LiO₃S. La figure A.1 montre une série chronologique complète des différences de température sur 20 ans entre les deux lidars à quatre niveaux d'altitude différents. La figure A.2 montre la différence de température moyenne médiane statistique entre les deux lidars.

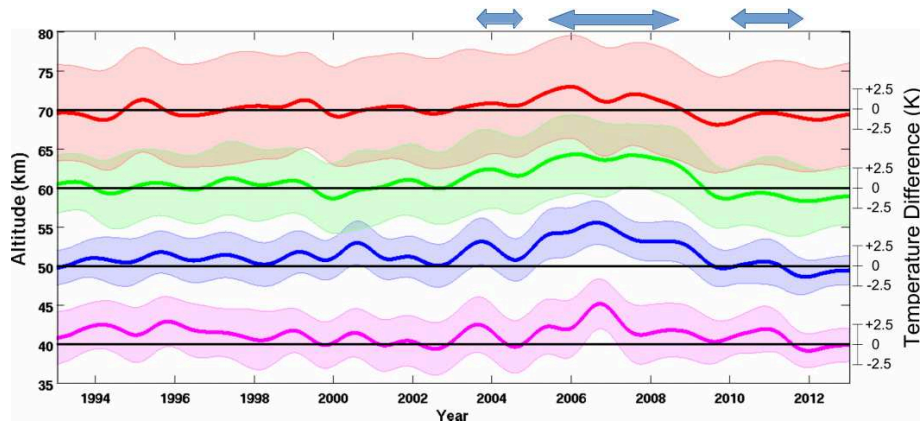


FIGURE A.1: Différences des température moyennes obtenues avec les lidars de OHP, LTA et LiO₃S, pendant une période de 20 ans entre 1993 et 2013 à quatre niveaux d'altitude: 65-75 km (rouge), 55-65 km (vert), 45-55 km (bleu) et 35-45 km (magenta). Les incertitudes ombrées sont indiquées en 1 sigma pour plus de clarté et les lignes noires représentent une différence de température nulle décalée à 40, 50, 60 et 70 km. Toutes les mesures, y compris les périodes de mauvais alignement de lidar, sont incluses dans ce graphique. Les anomalies apparentes (flèches bleues) ne se produisent que pendant les périodes où les lidars étaient souvent mal alignés.

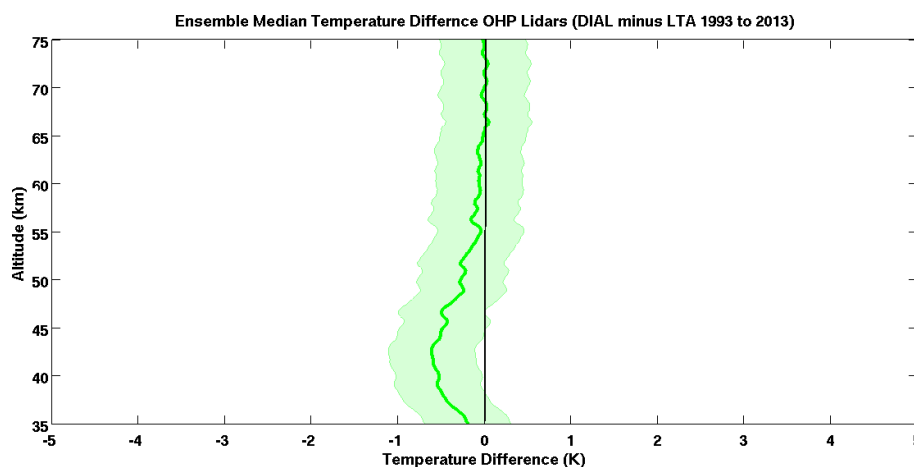


FIGURE A.2: Ensemble des différences de température médianes entre LTA et LiO₃S basé sur les mesures de température effectuées entre 1993 et 2013. L'erreur ombrée correspond à la distribution en deux sigma de l'ensemble.

En plus, nous avons abordé les préoccupations précédemment publiées concernant le biais relatif chaud lidar-satellite lors de comparaisons dans la haute mésosphère et la thermosphère inférieure en préparation de notre comparaison lidar décennale. Nous détaillons un algorithme de traitement de données qui minimise les erreurs connues dues aux procédures de sélection de données, aux choix a priori et aux paramètres d'initialisation inhérents à la récupération lidar. Comme on peut le voir sur la figure A.3, notre algorithme a pour résultat un refroidissement médian du profil de température absolue calculé par le lidar de 20 K à 90 km d'altitude par rapport à l'algorithme standard de la température du lidar. La confiance suscitée par la validation croisée à long terme de deux lidars indépendants et le base de données de température lidar amélioré est exploitée pour être utilisée dans des validations de satellites pluriannuels.

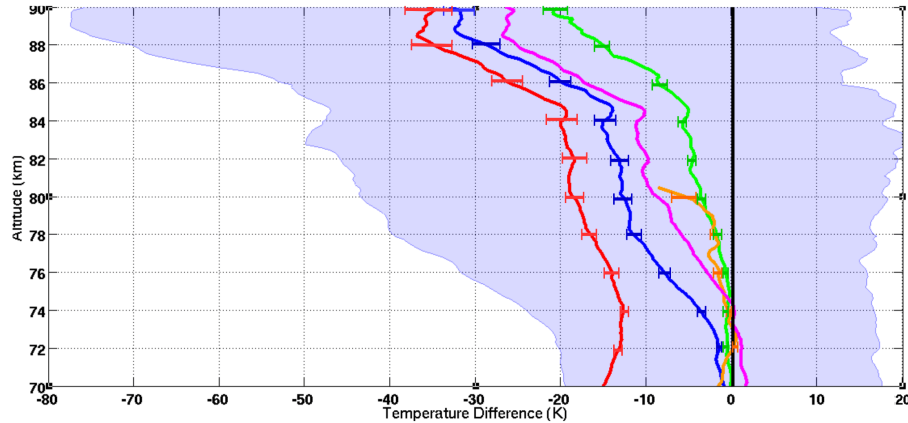


FIGURE A.3: Différences de température d'ensemble par rapport aux températures standard NDACC LTA de Rayleigh (noir). MLS (rouge), SABER (bleu avec variance d'ensemble ombrée), MSIS-90 (magenta), LiO_3S (orange) et LTA Rayleigh températures corrigées dans cet ouvrage (vert).

Ce travail est la première analyse décennale des différences de température systématiques entre les lidars OHP et 2433 nuits de températures lidar OHP avec des mesures de température co-localisées à partir du Sondeur Micro-onde des Limbes (MLS) et de l'instrument Sondage de l'Atmosphère par Radiométrie à Émission du large bande (SABER). Les comparaisons ont été effectuées à l'aide de données de janvier 2002 à mars 2018 dans la région géographique située autour de l'observatoire (43.93° N , 5.71° E). Nous avons trouvé des différences systématiques entre les températures mesurées à partir du lidar terrestre et celles mesurées à partir des satellites, ce qui suggère des distorsions non linéaires dans les récupérations d'altitude des satellites. Nous trouvons un biais froid dû à la stratopause hivernale dans les mesures satellitaires par rapport au lidar (-6 K pour SABER et -17 K pour MLS), un biais chaud mésosphérique (6 K vers 60 km), et un biais structuré verticalement pour MLS (-4 à 4 K). Nous avons corrigé la hauteur de stratopause des mesures satellites en utilisant les températures lidar et avons constaté une amélioration de la comparaison. Le biais relatif en hiver entre le lidar et SABER a été réduit à 1 K dans la stratosphère et dans la mésosphère et le biais chaud mésosphérique en été est réduit par 2 K. Les corrections d'altitude de stratopause ont réduit le biais relatif entre le lidar et le MLS de 4 K au début de

l'automne et à la fin du printemps, mais n'ont pas permis de traiter les artefacts verticaux dans les profils de température du MLS.

Un exemple des trois profils de température de la nuit du 25 juillet 2012 est présenté à la Fig. A.4. Dans cette comparaison, le profil lidar a été produit en 4 heures et a une résolution verticale de 150 m, allant de 30 km à plus de 90 km. La grande incertitude sur la température au-dessus de 70 km résulte de la résolution verticale fine requise pour capturer la couche d'inversion mésosphérique présente à proximité de 77 km.

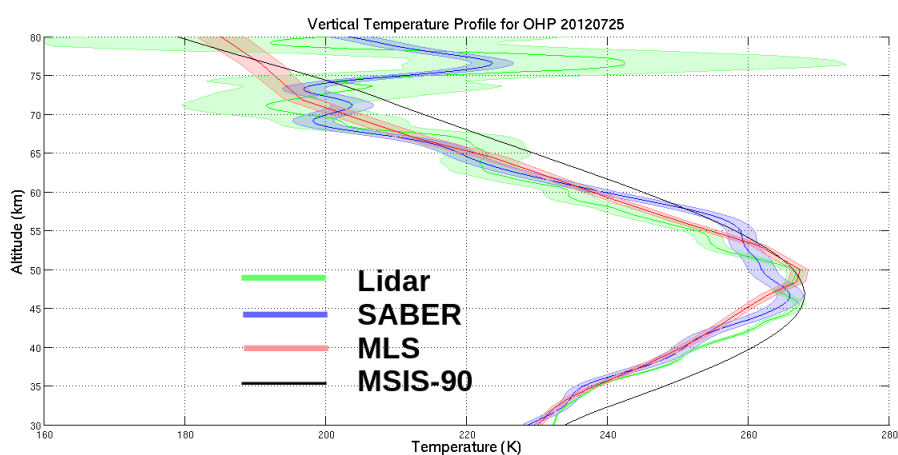


FIGURE A.4: Exemple de profils de température co-localisés du lidar OHP (vert), SABER (bleu), MLS (rouge) et MSIS (noir).

De 2002 à 2018, il y a eu 1100 mesures simultanées de qualité suffisante entre les lidars OHP et SABER. La figure A.5 (panneau supérieur) indique les différences de température mensuelles médianes entre le lidar et SABER, tandis que la Fig. A.5 (panneau inférieur) indique le biais de température saisonnier moyen avec l'altitude.

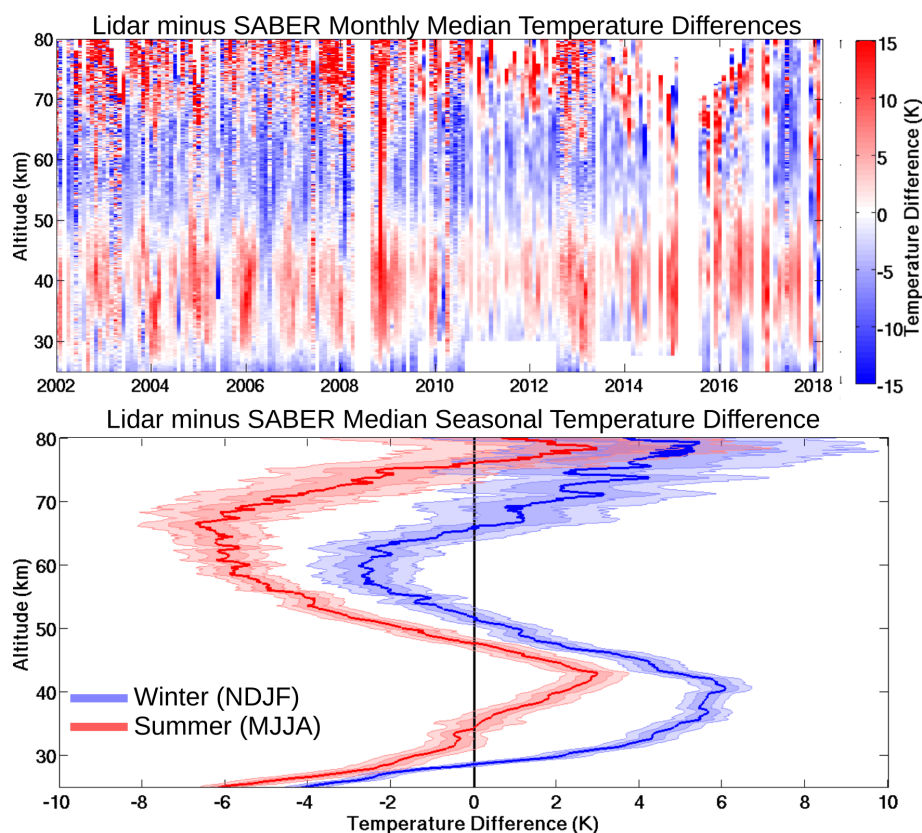


FIGURE A.5: Comparaison systématique sur 16 ans des lidars OHP et des températures SABER. Les différences de température mensuelles médianes entre le lidar et SABER sont indiquées dans le panneau supérieur. Le rouge indique que le lidar est plus chaud que SABER et le bleu que le lidar est plus froid. Il y a 1100 nuits de mesures coïncidentes dans le diagramme de couleurs. Le panneau inférieur est un ensemble saisonnier des différences de température lidar moins SABER. L'ensemble d'été (mai, juin, juillet et août) en rouge comprend 306 nuits de mesures coïncidentes et l'ensemble d'hiver (novembre, décembre, janvier, février) en bleu comprend 397 nuits de mesures coïncidentes. Les erreurs ombrées représentent 1 et 2 écarts types.

Entre 2004 et 2018, 1741 mesures simultanées de qualité suffisante entre lidars

OHP et MLS ont été effectuées. Dans la figure [A.6](#), nous voyons un biais chaud dans la stratosphère qui semble avoir une phase de migration vers le bas à mesure que l'hiver avance. Dans le panneau inférieur correspondant, nous voyons des différences systématiques très marquées de l'heure d'été qui alternent du chaud au froid dans la stratosphère et la mésosphère. L'ensemble hivernal présente un très important biais chaud lidar près de la stratopause.

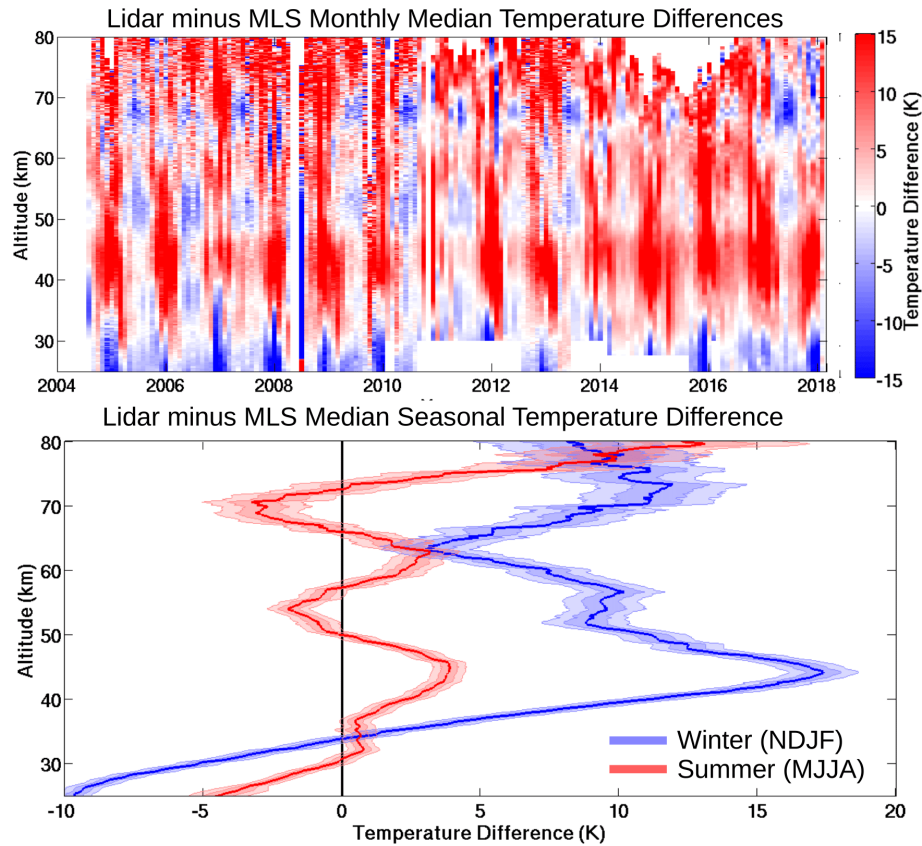


FIGURE A.6: Comparaison systématique sur 14 ans des températures de OHP lidar et de MLS. Les différences de température mensuelles médianes entre les lidars et MLS sont indiquées dans le panneau supérieur. Il y a 1741 nuits de mesures coïncidentes. Le panneau inférieur est un ensemble saisonnier des différences de température lidar moins MLS. L'ensemble d'été (mai, juin, juillet et août) en rouge comprend 554 nuits de mesures coïncidentes et l'ensemble d'hiver (novembre, décembre, janvier, février) en bleu comprend 653 nuits de mesures coïncidentes. Les erreurs ombrées représentent 1 et 2 écarts types.

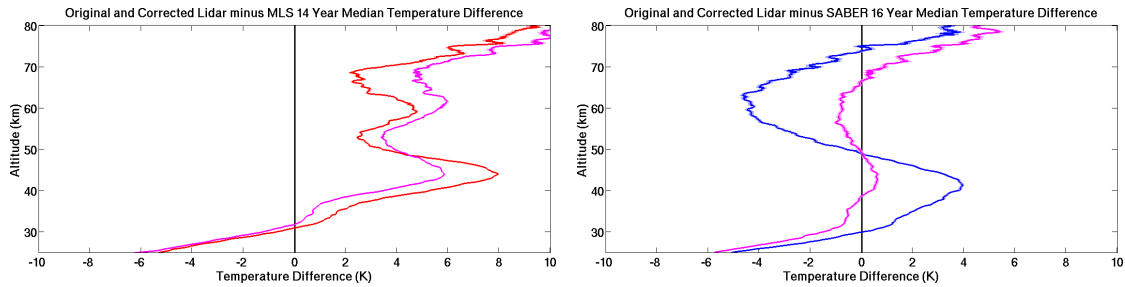
Nous avons étudié un décalage vertical possible entre les mesures lidar et satellite afin de déterminer si cela pouvait contribuer aux biais de température. Pour que les deux profils de température correspondent exactement en amplitude et en altitude,

un facteur de correction dépendant de l'altitude unique est utilisé pour chaque comparaison. Cependant, nous pouvons faire une estimation approximative du décalage vertical moyen entre les deux mesures en nous concentrant sur la région de la stratopause qui a généralement une altitude définie et une structure claire. Nous avons utilisé une méthode simple des moindres carrés pour estimer au mieux le décalage vertical qui minimiserait les différences de température entre la mesure lidar et la mesure par satellite. Nous avons calculé un décalage moyen de 1446 m avec une erreur standard de 49 m pour SABER et de 911 m avec une erreur standard de 90 m en MLS. Nous avons appliqué cette correction d'altitude aux données satellite et comparé aux mesures lidar d'origine.

La figure A.7a montre la différence de température d'ensemble pour toutes les comparaisons de température entre le lidar et le MLS 1741 avant correction (rouge) et après correction (magenta). Le biais chaud important près de 45 km a été réduit de 8 à 6 km, mais les polarisations dues au froid à 53 km et à 68 km sont aggravées par la correction. Pour comprendre ce résultat, nous pouvons examiner la dépendance saisonnière de la correction appliquée. La figure A.7c représente la différence de température d'ensemble d'été (MJJA), constituée de 554 comparaisons de température lidar-MLS avant correction (rouge) et après correction (magenta). Il y a une amélioration marginale après correction au-dessous de 55 km, mais le changement n'est pas significatif à 2σ et la structure du biais de température reste inchangée. La figure A.7e représente la différence de température d'ensemble d'hiver (NDJF) composée de 653 comparaisons de température lidar-MLS avant correction (en bleu) et après correction (en magenta). Il y a une amélioration significative de 4 K dans le grand biais froid à 45 km. La comparaison lidar-MLS corrigée est également nettement moins bonne près du biais froid, à 63 km.

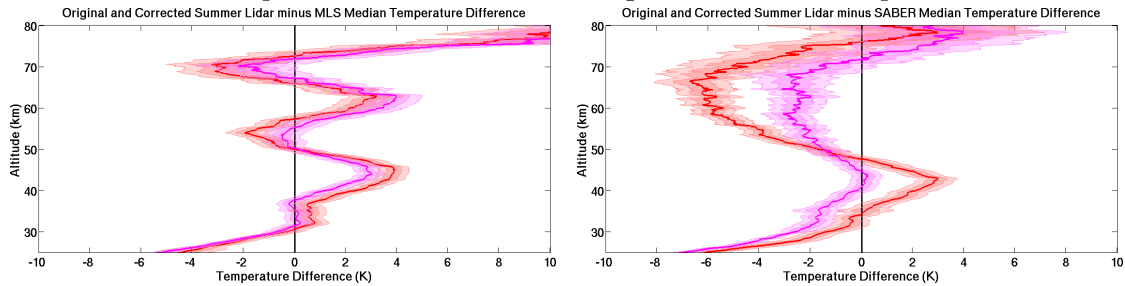
La figure A.7b montre la différence de température d'ensemble pour toutes les comparaisons de température 1100 lidar-SABER avant correction (en bleu) et après correction (en magenta). la correction de la hauteur de la stratopause a réduit le biais chaud de la stratosphère, de 4 K à moins de 1 K, et du biais froid de la mésosphère, de -4 K à -1 K. Le biais chaud au-dessus de 70 km a été légèrement augmenté. La figure A.7d représente la différence de température d'ensemble d'été (MJJA) composée de 306 comparaisons de température lidar-SABER avant correction (rouge) et après correction (magenta). Il y a une réduction significative de 3 K du biais chaud à 45 km et une réduction significative du biais du froid mésosphérique de -6 K à -3 K. La figure A.7f est la différence de température

d'ensemble d'hiver (NDJF) constituée de 397 comparaisons de température lidar-SABER avant correction (bleu) et après correction (magenta). En appliquant la correction d'altitude, nous avons éliminé la forme en "S" dans la courbe de différence de température entre 30 et 60 km. Il reste un important biais chaud constant de 1 K après correction. Au-dessus de 70 km, il n'y a pas de changement significatif sur le plan statistique.



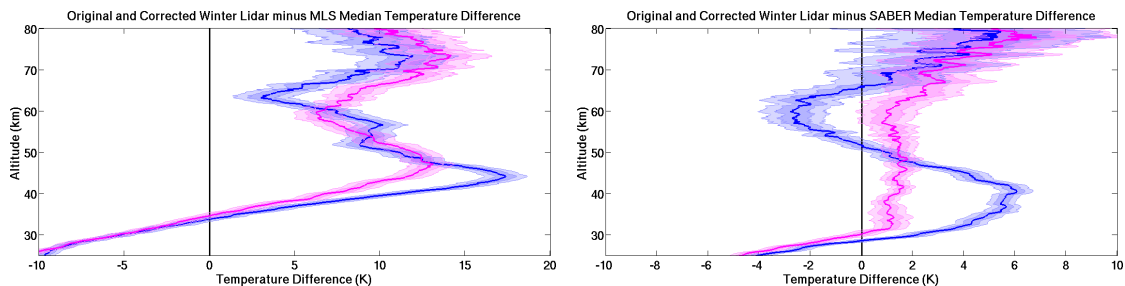
(A) Différence de température médiane pour les profils de température de 1741 lidar moins MLS de 2004 à 2018. Le rouge est l'ensemble original et le magenta l'ensemble après correction.

(B) Différence de température médiane pour 1100 lidars moins les profils de température SABER de 2002 à 2018. Le bleu correspond à l'ensemble d'origine et le magenta à l'ensemble après correction.



(C) Différence de température médiane estivale (MJJA) pour 554 lidar moins les profils de température MLS de 2004 à 2018. Le rouge est l'ensemble original et le magenta est l'ensemble après correction.

(D) Différence de température médiane estivale (MJJA) pour 306 lidar moins les profils de température SABER de 2002 à 2018. Le rouge est l'ensemble original et le magenta est l'ensemble après correction.



(E) Différence de température médiane hivernale (NDJF) de 653 lidar moins les profils de température MLS de 2004 à 2018. Le bleu correspond à l'ensemble d'origine et le magenta à l'ensemble après correction.

(F) Différence de température médiane hivernale (NDJF) pour 397 lidar moins les profils de température SABER de 2002 à 2018. Le bleu correspond à l'ensemble d'origine et le magenta à l'ensemble après correction.

FIGURE A.7: Ensemble pour lidar moins MLS différences de température (à gauche) et lidar moins SABER (à droite). Les ensembles de tous les profils sont situés dans la rangée supérieure, les profils d'été (MJJA) dans la rangée centrale et d'hiver (NDJF) dans la rangée inférieure.

Nous avons également apporté des données lidar à la validation de la nouvelle base de données de température GOMOS. La figure A.8 montre un exemple de profil de température lidar et de quelques profils de température GOMOS.

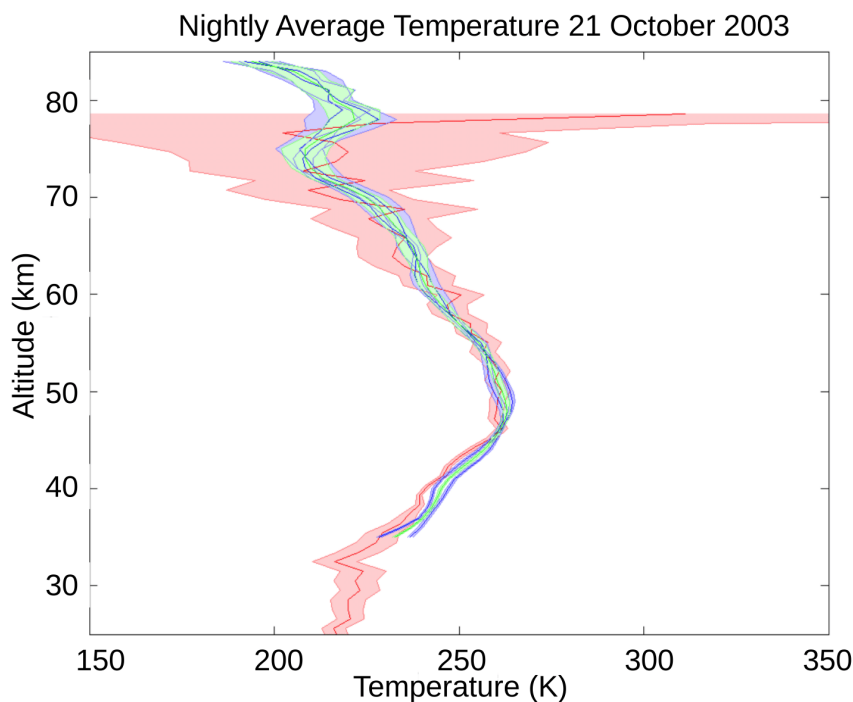


FIGURE A.8: Exemple de comparaison entre un profil lidar de Rayleigh à OHP le 21 octobre 2003 (en rouge) et deux profils GOMOS colocalisés sélectionnés à l'aide des critères de co-localisation (en bleu et vert). Lorsque deux ou plusieurs profils GOMOS sont sélectionnés, le profil médian est utilisé pour la comparaison statistique. Pour le profil lidar (rouge), chaque profil individuel GOMOS (bleu) et le profil médian GOMOS (vert), l'écart type de son incertitude est représenté par la zone ombrée.

En suivant la même procédure utilisée pour comparer les données lidar à MLS et SABER, nous avons comparé les profils de température lidar OHP à GOMOS. La différence médiane statistique entre la température du lidar et la température du gant est inférieure à 46 km, négative entre 46 et 73 km et inférieure à -5

K entre 55 et 60 km et encore positif au-dessus de 73 km avec +7 K à 85 km. La dispersion des différences reste comprise entre ± 5 K et ± 10 K dans toute la gamme d'altitudes. La différence positive dans la partie supérieure du profil peut être au moins partiellement due à un biais chaud dans la température de OHP supérieure à 75 km, comme indiqué par (R. Wing, A. Hauchecorne, P. Keckhut, Godin-Beekmann, S. Khaykin, and McCullough, 2018a) en utilisant une comparaison avec SABER-TIMED. L'alternance des différences positives et négatives avec l'altitude peut indiquer une contribution des marées thermiques atmosphériques, car les mesures de température ne sont pas obtenues simultanément. Les mesures GOMOS au-dessus de OHP sont effectuées pendant la journée vers 11h00, heure solaire, tandis que les opérations lidar sont effectuées pendant la première partie de la nuit pendant plusieurs heures, avec une séquence moyenne estimée vers 21h00. temps solaire en moyenne.

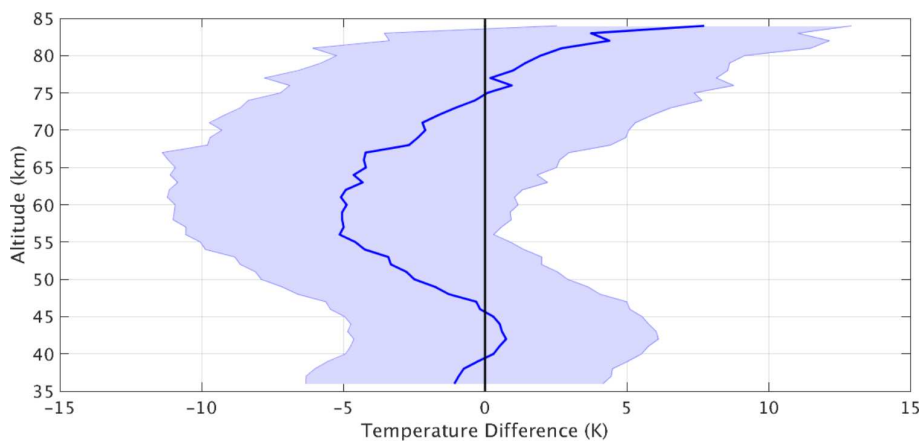


FIGURE A.9: Différence de température médiane statistique entre les profils de température lidar OHP et GOMOS (température lidar moins GOMOS). La zone ombrée représente la dispersion des différences (un écart type).

Bibliography

- Alpers, M. et al. (2004). “Temperature lidar measurements from 1 to 105 km altitude using resonance, Rayleigh, and Rotational Raman scattering”. In: *Atmospheric Chemistry and Physics* 4.3, pp. 793–800. DOI: [10.5194/acp-4-793-2004](https://doi.org/10.5194/acp-4-793-2004). URL: <https://www.atmos-chem-phys.net/4/793/2004/>.
- Apruzese, John P., Darrell F. Strobel, and Mark R. Schoeberl (1984). “Parameterization of IR cooling in a Middle Atmosphere Dynamics Model: 2. Non-LTE radiative transfer and the globally averaged temperature of the mesosphere and lower thermosphere”. In: *Journal of Geophysical Research: Atmospheres* 89.D3, pp. 4917–4926. ISSN: 2156-2202. DOI: [10.1029/JD089iD03p04917](https://doi.org/10.1029/JD089iD03p04917). URL: <http://dx.doi.org/10.1029/JD089iD03p04917>.
- Argall, P.S. (2007). “Upper altitude limit for Rayleigh lidar”. In: *Annales Geophysicae* 25, pp. 19–25. DOI: [10.5194/angeo-25-19-2007](https://doi.org/10.5194/angeo-25-19-2007).
- Aßmann, Richard (1902). *Über die Existenz eines wärmeren Luftstromes in der Höhe von 10 bis 15 km.*
- Baldwin, Mark P. and Timothy J. Dunkerton (2001). “Stratospheric Harbingers of Anomalous Weather Regimes”. In: *Science* 294.5542, pp. 581–584. ISSN: 0036-8075. DOI: [10.1126/science.1063315](https://doi.org/10.1126/science.1063315). eprint: <http://science.sciencemag.org/content/294/5542/581.full.pdf>. URL: <http://science.sciencemag.org/content/294/5542/581>.
- Beagley, Stephen R. et al. (2000). “The Extended Canadian Middle Atmosphere Model”. In: *Geophysical Research Letters* 27.16, pp. 2529–2532. DOI: [10.1029/1999GL011233](https://doi.org/10.1029/1999GL011233). eprint: <https://agupubs.onlinelibrary.wiley.com/doi/pdf/10.1029/1999GL011233>. URL: <https://agupubs.onlinelibrary.wiley.com/doi/abs/10.1029/1999GL011233>.
- Beig, G. et al. (2003). “Review of mesospheric temperature trends”. In: *Reviews of Geophysics* 41.4. DOI: [10.1029/2002RG000121](https://doi.org/10.1029/2002RG000121). eprint: <https://agupubs.onlinelibrary.wiley.com/doi/pdf/10.1029/2002RG000121>. URL: <https://agupubs.onlinelibrary.wiley.com/doi/abs/10.1029/2002RG000121>.
- Bertaux, Jean-Loup et al. (2010). “Global ozone monitoring by occultation of stars: an overview of GOMOS measurements on ENVISAT”. In: *Atmospheric*

- Chemistry and Physics* 10.24, pp. 12091–12148. DOI: [10.5194/acp-10-12091-2010](https://doi.org/10.5194/acp-10-12091-2010). URL: <https://hal.archives-ouvertes.fr/hal-00474411>.
- Bevington, P. R. and D. K. Robinson (1992). *Data Reduction and Error Analysis for the Physical Sciences*. 2nd ed. Dordrecht: McGraw-Hill.
- Bourassa, A. E. et al. (2014). “Trends in stratospheric ozone derived from merged SAGE II and Odin-OSIRIS satellite observations”. In: *Atmospheric Chemistry and Physics* 14.13, pp. 6983–6994. DOI: [10.5194/acp-14-6983-2014](https://doi.org/10.5194/acp-14-6983-2014). URL: <https://www.atmos-chem-phys.net/14/6983/2014/>.
- Boyd, R. L. F. (1954). “Rocket Research in the Upper Atmosphere”. In: *Science Progress* 42.167, pp. 435–448. ISSN: 00368504, 20477163. URL: <http://www.jstor.org/stable/43423332>.
- Brewer, A. W. (1949). “Evidence for a world circulation provided by the measurements of helium and water vapour distribution in the stratosphere”. In: *Quarterly Journal of the Royal Meteorological Society* 75.326, pp. 351–363. DOI: [10.1002/qj.49707532603](https://doi.org/10.1002/qj.49707532603). eprint: <https://rmets.onlinelibrary.wiley.com/doi/pdf/10.1002/qj.49707532603>. URL: <https://rmets.onlinelibrary.wiley.com/doi/abs/10.1002/qj.49707532603>.
- Chapman, S. (1930). “On Ozone and Atomic Oxygen in the Upper Atmosphere”. In: *The Philosophical Magazine and Journal of Science*.
- Charlton-Perez, Andrew J., Laura Ferranti, and Robert W. Lee (2018). “The influence of the stratospheric state on North Atlantic weather regimes”. In: *Quarterly Journal of the Royal Meteorological Society* 144.713, pp. 1140–1151. DOI: [10.1002/qj.3280](https://doi.org/10.1002/qj.3280). eprint: <https://rmets.onlinelibrary.wiley.com/doi/pdf/10.1002/qj.3280>. URL: <https://rmets.onlinelibrary.wiley.com/doi/abs/10.1002/qj.3280>.
- Chu, Xinzhaoh et al. (2002). “Fe Boltzmann Temperature Lidar: Design, Error Analysis, and Initial Results at the North and South Poles”. In: 41, pp. 4400–10.
- Clancy, R. Todd, David W. Rusch, and Michael T. Callan (1994). “Temperature minima in the average thermal structure of the middle mesosphere (70–80 km) from analysis of 40- to 92-km SME global temperature profiles”. In: *Journal of Geophysical Research: Atmospheres* 99.D9, pp. 19001–19020. DOI: [10.1029/94JD01681](https://doi.org/10.1029/94JD01681). eprint: <https://agupubs.onlinelibrary.wiley.com/doi/pdf/10.1029/94JD01681>. URL: <https://agupubs.onlinelibrary.wiley.com/doi/abs/10.1029/94JD01681>.
- Council, National Research (2007). *Earth Science and Applications from Space: National Imperatives for the Next Decade and Beyond*. Washington, DC: The

- National Academies Press. ISBN: 978-0-309-14090-4. DOI: [10.17226/11820](https://doi.org/10.17226/11820). URL: <https://www.nap.edu/catalog/11820/earth-science-and-applications-from-space-national-imperatives-for-the>.
- Cutler, Laura J. et al. (2001). “Rayleigh lidar observations of mesospheric inversion layers at Poker Flat, Alaska (65 °N, 147°W)”. In: *Geophysical Research Letters* 28.8, pp. 1467–1470. DOI: [10.1029/2000GL012535](https://doi.org/10.1029/2000GL012535). eprint: <https://agupubs.onlinelibrary.wiley.com/doi/pdf/10.1029/2000GL012535>. URL: <https://agupubs.onlinelibrary.wiley.com/doi/abs/10.1029/2000GL012535>.
- Dawkins, E. C. M. et al. (2018). “Validation of SABER v2.0 Operational Temperature Data With Ground-Based Lidars in the Mesosphere-Lower Thermosphere Region (75–105km)”. In: *Journal of Geophysical Research: Atmospheres*. DOI: [10.1029/2018JD028742](https://doi.org/10.1029/2018JD028742).
- Dobson, Harrison, and Lawrence (1929). “Measurements of the amount of ozone in the Earth’s atmosphere and its relation to other geophysical conditions. – Part III”. In: *Proceedings of the Royal Society of London A: Mathematical, Physical and Engineering Sciences* 122.790, pp. 456–486. ISSN: 0950-1207. DOI: [10.1098/rspa.1929.0034](https://doi.org/10.1098/rspa.1929.0034). eprint: <http://rspa.royalsocietypublishing.org/content/122/790/456.full.pdf>. URL: <http://rspa.royalsocietypublishing.org/content/122/790/456>.
- Donovan, D. P., J. A. Whiteway, and A. I. Carswell (1993). “Correction for non-linear photon-counting effects in lidar systems”. In: *Appl. Opt.* 32.33, pp. 6742–6753. DOI: [10.1364/AO.32.006742](https://doi.org/10.1364/AO.32.006742). URL: <http://ao.osa.org/abstract.cfm?URI=ao-32-33-6742>.
- Dou, Xiankang et al. (2009). “Seasonal oscillations of middle atmosphere temperature observed by Rayleigh lidars and their comparisons with TIMED/SABER observations”. In: *Journal of Geophysical Research: Atmospheres* 114.D20. D20103, n/a–n/a. ISSN: 2156-2202. DOI: [10.1029/2008JD011654](https://doi.org/10.1029/2008JD011654). URL: <http://dx.doi.org/10.1029/2008JD011654>.
- Duck, Thomas J. et al. (2001). “Rayleigh lidar observations of a mesospheric inversion layer during night and day”. In: *Geophysical Research Letters* 28.18, pp. 3597–3600. DOI: [10.1029/2001GL013409](https://doi.org/10.1029/2001GL013409). eprint: <https://agupubs.onlinelibrary.wiley.com/doi/pdf/10.1029/2001GL013409>. URL: <https://agupubs.onlinelibrary.wiley.com/doi/abs/10.1029/2001GL013409>.
- Fechine, J. et al. (2008). “Lower-mesospheric inversion layers over brazilian equatorial region using TIMED/SABER temperature profiles”. In: *Advances in Space Research* 41.9, pp. 1447–1453. ISSN: 0273-1177. DOI: [10.1016/j.asr.2007](https://doi.org/10.1016/j.asr.2007).

- 04.070. URL: <http://www.sciencedirect.com/science/article/pii/S0273117707004115>.
- Fishbein, E. F. et al. (1996). "Validation of UARS Microwave Limb Sounder temperature and pressure measurements". In: *Journal of Geophysical Research: Atmospheres* 101.D6, pp. 9983–10016. DOI: [10.1029/95JD03791](https://doi.org/10.1029/95JD03791). eprint: <https://agupubs.onlinelibrary.wiley.com/doi/pdf/10.1029/95JD03791>. URL: <https://agupubs.onlinelibrary.wiley.com/doi/abs/10.1029/95JD03791>.
- Forster, Piers M. de F. and K. P. Shine (2002). "Assessing the climate impact of trends in stratospheric water vapor". In: *Geophysical Research Letters* 29.6. DOI: [10.1029/2001GL013909](https://doi.org/10.1029/2001GL013909). eprint: <https://agupubs.onlinelibrary.wiley.com/doi/pdf/10.1029/2001GL013909>. URL: <https://agupubs.onlinelibrary.wiley.com/doi/abs/10.1029/2001GL013909>.
- French, W. J. R. and F. J. Mulligan (2010). "Stability of temperatures from TIMED/SABER v1.07 (2002–2009) and Aura/MLS v2.2 (2004–2009) compared with OH(6-2) temperatures observed at Davis Station, Antarctica". In: *Atmospheric Chemistry and Physics* 10.23, pp. 11439–11446. DOI: [10.5194/acp-10-11439-2010](https://doi.org/10.5194/acp-10-11439-2010). URL: <https://www.atmos-chem-phys.net/10/11439/2010/>.
- Funatsu, Beatriz M., Chantal Claud, Philippe Keckhut, and Alain Hauchecorne (2008). "Cross-validation of Advanced Microwave Sounding Unit and lidar for long-term upper-stratospheric temperature monitoring". In: *Journal of Geophysical Research: Atmospheres* 113.D23. DOI: [10.1029/2008JD010743](https://doi.org/10.1029/2008JD010743). eprint: <https://agupubs.onlinelibrary.wiley.com/doi/pdf/10.1029/2008JD010743>. URL: <https://agupubs.onlinelibrary.wiley.com/doi/abs/10.1029/2008JD010743>.
- Funatsu, Beatriz M., Chantal Claud, Philippe Keckhut, Alain Hauchecorne, and Thierry Leblanc (2016). "Regional and seasonal stratospheric temperature trends in the last decade (2002–2014) from AMSU observations". In: *Journal of Geophysical Research: Atmospheres* 121.14, pp. 8172–8185. DOI: [10.1002/2015JD024305](https://doi.org/10.1002/2015JD024305). eprint: <https://agupubs.onlinelibrary.wiley.com/doi/pdf/10.1002/2015JD024305>. URL: <https://agupubs.onlinelibrary.wiley.com/doi/abs/10.1002/2015JD024305>.
- Gan, Quan, Shao Dong Zhang, and Fan Yi (2012). "TIMED/SABER observations of lower mesospheric inversion layers at low and middle latitudes". In: *Journal of Geophysical Research: Atmospheres* 117.D7. DOI: [10.1029/2012JD017455](https://doi.org/10.1029/2012JD017455). eprint: <https://agupubs.onlinelibrary.wiley.com/doi/pdf/10.1029/>

- 2012JD017455. URL: <https://agupubs.onlinelibrary.wiley.com/doi/abs/10.1029/2012JD017455>.
- García-Comas, M. et al. (2014a). “MIPAS temperature from the stratosphere to the lower thermosphere: Comparison of vM21 with ACE-FTS, MLS, OSIRIS, SABER, SOFIE and lidar measurements”. In: *Atmospheric Measurement Techniques* 7.11, pp. 3633–3651. DOI: [10.5194/amt-7-3633-2014](https://doi.org/10.5194/amt-7-3633-2014). URL: <https://www.atmos-meas-tech.net/7/3633/2014/>.
- (2014b). “MIPAS temperature from the stratosphere to the lower thermosphere: Comparison of vM21 with ACE-FTS, MLS, OSIRIS, SABER, SOFIE and lidar measurements”. In: *Atmospheric Measurement Techniques* 7.11, pp. 3633–3651. DOI: [10.5194/amt-7-3633-2014](https://doi.org/10.5194/amt-7-3633-2014). URL: <https://www.atmos-meas-tech.net/7/3633/2014/>.
- Gille, John C. et al. (1996). “Accuracy and precision of cryogenic limb array etalon spectrometer (CLAES) temperature retrievals”. In: *Journal of Geophysical Research: Atmospheres* 101.D6, pp. 9583–9601. DOI: [10.1029/96JD00052](https://doi.org/10.1029/96JD00052). eprint: <https://agupubs.onlinelibrary.wiley.com/doi/pdf/10.1029/96JD00052>. URL: <https://agupubs.onlinelibrary.wiley.com/doi/abs/10.1029/96JD00052>.
- Goddard, R. H. (1919). “A Method of Reaching Extreme Altitudes”. In: *Smithsonian Miscellaneous Collections* 71.2.
- Godin-Beekmann, S., J. Porteneuve, and A. Garnier (2003). “Systematic DIAL lidar monitoring of the stratospheric ozone vertical distribution at Observatoire de Haute-Provence (43.92°N, 5.71°E)”. In: *Journal of Environmental Monitoring* 5, pp. 57–67. DOI: [10.1039/B205880D](https://doi.org/10.1039/B205880D).
- Google, Map data: (2017). *Observatoire de Haute Provence (CNRS) Kernel Description*. URL: [https://www.google.fr/maps/place/Observatoire+de+Haute+Provence+\(CNRS\)/@43.9236737,5.7183398](https://www.google.fr/maps/place/Observatoire+de+Haute+Provence+(CNRS)/@43.9236737,5.7183398) (visited on 11/30/2017).
- Gross, Michael R. et al. (1997). “Temperature measurements made with a combined Rayleigh–Mie and Raman lidar”. In: *Appl. Opt.* 36.24, pp. 5987–5995. DOI: [10.1364/AO.36.005987](https://doi.org/10.1364/AO.36.005987). URL: <http://ao.osa.org/abstract.cfm?URI=ao-36-24-5987>.
- H. Glassmeier, K and B T. Tsurutani (2014). “Carl Friedrich Gauss - General Theory of Terrestrial Magnetism - a revised translation of the German text”. In: *History of Geo- and Space Sciences* 5. DOI: [10.5194/hgss-5-11-2014](https://doi.org/10.5194/hgss-5-11-2014).
- Hagan, M. E. et al. (1999). “GSWM-98: Results for migrating solar tides”. In: *Journal of Geophysical Research: Space Physics* 104.A4, pp. 6813–6827. DOI: [10.1029/1998JA000000](https://doi.org/10.1029/1998JA000000).

- 1029/1998JA900125. eprint: <https://agupubs.onlinelibrary.wiley.com/doi/pdf/10.1029/1998JA900125>. URL: <https://agupubs.onlinelibrary.wiley.com/doi/abs/10.1029/1998JA900125>.
- Haigh, Joanna D. (1996). “The Impact of Solar Variability on Climate”. In: *Science* 272.5264, pp. 981–984. ISSN: 0036-8075. DOI: 10.1126/science.272.5264.981. eprint: <http://science.sciencemag.org/content/272/5264/981.full.pdf>. URL: <http://science.sciencemag.org/content/272/5264/981>.
- Hardiman, S. C. et al. (2010). “The Climatology of the Middle Atmosphere in a Vertically Extended Version of the Met Office’s Climate Model. Part I: Mean State”. In: *Journal of the Atmospheric Sciences* 67.5, pp. 1509–1525. DOI: 10.1175/2009JAS3337.1. eprint: <https://doi.org/10.1175/2009JAS3337.1>. URL: <https://doi.org/10.1175/2009JAS3337.1>.
- Hauchecorne, A., L. Blanot, et al. (2018). “A new MesosphEO dataset of temperature profiles from 35 to 85 km using Rayleigh scattering at limb from GOMOS/ENVISAT daytime observations”. In: *Atmospheric Measurement Techniques Discussions* 2018, pp. 1–19. DOI: 10.5194/amt-2018-241. URL: <https://www.atmos-meas-tech-discuss.net/amt-2018-241/>.
- Hauchecorne, A., M. L. Chanin, and R. Wilson (1987). “Mesospheric temperature inversion and gravity wave breaking”. In: *Geophysical Research Letters* 14.9, pp. 933–936. DOI: 10.1029/GL014i009p00933. eprint: <https://agupubs.onlinelibrary.wiley.com/doi/pdf/10.1029/GL014i009p00933>. URL: <https://agupubs.onlinelibrary.wiley.com/doi/abs/10.1029/GL014i009p00933>.
- Hauchecorne, Alain and Marie-Lise Chanin (1980a). “Density and temperature profiles obtained by lidar between 35 and 70 km”. In: *Geophysical Research Letters* 7.8, pp. 565–568. DOI: 10.1029/GL007i008p00565. eprint: <https://agupubs.onlinelibrary.wiley.com/doi/pdf/10.1029/GL007i008p00565>. URL: <https://agupubs.onlinelibrary.wiley.com/doi/abs/10.1029/GL007i008p00565>.
- (1980b). “Density and temperature profiles obtained by lidar between 35 and 70 km”. In: *Geophysical Research Letters* 7.8, pp. 565–568. ISSN: 1944-8007. DOI: 10.1029/GL007i008p00565. URL: <http://dx.doi.org/10.1029/GL007i008p00565>.
- Hauchecorne, Alain, Marie-Lise Chanin, and P. Keckhut (1991). “Climatology and trends of the middle atmospheric temperature (33–87 km) as seen by Rayleigh lidar over the south of France”. In: *Journal of Geophysical Research: Atmospheres*

- 96.D8, pp. 15297–15309. DOI: [10.1029/91JD01213](https://doi.org/10.1029/91JD01213). eprint: <https://agupubs.onlinelibrary.wiley.com/doi/pdf/10.1029/91JD01213>. URL: <https://agupubs.onlinelibrary.wiley.com/doi/abs/10.1029/91JD01213>.
- Hauchecorne, Alain and Alexandre Maillard (1990). “A 2-d dynamical model of mesospheric temperature inversions in winter”. In: *Geophysical Research Letters* 17.12, pp. 2197–2200. DOI: [10.1029/GL017i012p02197](https://doi.org/10.1029/GL017i012p02197). eprint: <https://agupubs.onlinelibrary.wiley.com/doi/pdf/10.1029/GL017i012p02197>. URL: <https://agupubs.onlinelibrary.wiley.com/doi/abs/10.1029/GL017i012p02197>.
- Haywood, Jim M., Andy Jones, and Gareth S. Jones (2013). “The impact of volcanic eruptions in the period 2000–2013 on global mean temperature trends evaluated in the HadGEM2-ES climate model”. In: *Atmospheric Science Letters* 15.2, pp. 92–96. DOI: [10.1002/asl2.471](https://doi.org/10.1002/asl2.471). URL: <https://rmets.onlinelibrary.wiley.com/doi/abs/10.1002/asl2.471>.
- Hervig, Mark E. et al. (1996). “Validation of aerosol measurements from the Halogen Occultation Experiment”. In: *Journal of Geophysical Research: Atmospheres* 101.D6, pp. 10267–10275. DOI: [10.1029/95JD02464](https://doi.org/10.1029/95JD02464). eprint: <https://agupubs.onlinelibrary.wiley.com/doi/pdf/10.1029/95JD02464>. URL: <https://agupubs.onlinelibrary.wiley.com/doi/abs/10.1029/95JD02464>.
- Holton, James R. et al. (1995). “Stratosphere-troposphere exchange”. In: *Reviews of Geophysics* 33.4, pp. 403–439. DOI: [10.1029/95RG02097](https://doi.org/10.1029/95RG02097). eprint: <https://agupubs.onlinelibrary.wiley.com/doi/pdf/10.1029/95RG02097>. URL: <https://agupubs.onlinelibrary.wiley.com/doi/abs/10.1029/95RG02097>.
- Hoppel, K. W. et al. (2008). “Assimilation of stratospheric and mesospheric temperatures from MLS and SABER into a global NWP model”. In: *Atmospheric Chemistry & Physics* 8, pp. 6103–6116.
- IPCC (2013). “IPCC 2013: Climate Change 2013: The Physical Science Basis. Contribution of Working Group I to the Fifth Assessment Report of the Intergovernmental Panel on Climate Change”. In: DOI: [doi:10.1017/CB09781107415324](https://doi.org/10.1017/CB09781107415324).
- Johnson, K. W. and M. E. Gelman, eds. (1985). *Trends in upper stratospheric temperatures as observed by rocketsondes (1965-1983)*. Vol. 18.
- Keating, G.M. and C. Chen (1991). “Middle atmosphere change through solar forcing”. In: *Advances in Space Research* 11.3, pp. 9–20. ISSN: 0273-1177. DOI: [https://doi.org/10.1016/0273-1177\(91\)90397-3](https://doi.org/10.1016/0273-1177(91)90397-3). URL: <http://www.sciencedirect.com/science/article/pii/0273117791903973>.

- Keckhut, P., A. Hauchecorne, and M.L. Chanin (1993). “A critical review of the database acquired for the long-term surveillance of the middle atmosphere by the French Rayleigh lidars”. In: *Journal of Atmospheric and Oceanic Technology* 10.6. DOI: [10.1175/1520-0426\(1993\)010<0850:ACR0TD>2.0.CO;2](https://doi.org/10.1175/1520-0426(1993)010<0850:ACR0TD>2.0.CO;2).
- (1995). “Midlatitude long-term variability of the middle atmosphere: Trends and cyclic and episodic changes”. In: *Journal of Geophysical Research: Atmospheres* 100.D9, pp. 18887–18897. DOI: [10.1029/95JD01387](https://doi.org/10.1029/95JD01387). eprint: <https://agupubs.onlinelibrary.wiley.com/doi/pdf/10.1029/95JD01387>. URL: <https://agupubs.onlinelibrary.wiley.com/doi/abs/10.1029/95JD01387>.
- Keckhut, P., W.J. Randel, et al. (2011). “An evaluation of uncertainties in monitoring middle atmosphere temperatures with the ground-based lidar network in support of space observations”. In: *Journal of Atmospheric and Solar-Terrestrial Physics* 73.5, pp. 627–642. ISSN: 1364-6826. DOI: <https://doi.org/10.1016/j.jastp.2011.01.003>. URL: <http://www.sciencedirect.com/science/article/pii/S1364682611000046>.
- Keckhut, Philippe, Beatriz M. Funatsu, et al. (2015). “Tidal effects on stratospheric temperature series derived from successive advanced microwave sounding units”. In: *Quarterly Journal of the Royal Meteorological Society* 141.687, pp. 477–483. DOI: [10.1002/qj.2368](https://doi.org/10.1002/qj.2368). URL: <https://hal.archives-ouvertes.fr/hal-00989750>.
- Keckhut, Philippe, M. E. Gelman, et al. (1996). “Semidiurnal and diurnal temperature tides (30–55 km): Climatology and effect on UARS-LIDAR data comparisons”. In: *Journal of Geophysical Research: Atmospheres* 101.D6, pp. 10299–10310. DOI: [10.1029/96JD00344](https://doi.org/10.1029/96JD00344). eprint: <https://agupubs.onlinelibrary.wiley.com/doi/pdf/10.1029/96JD00344>. URL: <https://agupubs.onlinelibrary.wiley.com/doi/abs/10.1029/96JD00344>.
- Keckhut, Philippe et al. (2004a). “Review of ozone and temperature lidar validations performed within the framework of the Network for the Detection of Stratospheric Change”. In: *J. Environ. Monit.* 6 (9), pp. 721–733. DOI: [10.1039/B404256E](https://doi.org/10.1039/B404256E). URL: <http://dx.doi.org/10.1039/B404256E>.
- (2004b). “Review of ozone and temperature lidar validations performed within the framework of the Network for the Detection of Stratospheric Change”. In: *Journal of Environmental Monitoring* 6.9, pp. 721–733. DOI: [10.1039/b404256e](https://doi.org/10.1039/b404256e). URL: <http://pubs.rsc.org/en/Content/ArticleLanding/2004/EM/b404256e#!divAbstract>.

- Khanna, J., R. J. Sica, and C. T. McElroy (2011). “Atmospheric temperature retrievals from lidar measurements using techniques of non-linear mathematical inversion”. In: *AGU Fall Meeting Abstracts*.
- Khanna, Jaya et al. (2012). “New technique for retrieval of atmospheric temperature profiles from Rayleigh-scatter lidar measurements using nonlinear inversion”. In: *Appl. Opt.* 51.33, pp. 7945–7952. DOI: [10.1364/AO.51.007945](https://doi.org/10.1364/AO.51.007945). URL: <http://ao.osa.org/abstract.cfm?URI=ao-51-33-7945>.
- Khaykin, S. M., S. Godin-Beekmann, A. Hauchecorne, et al. (2018). “Stratospheric Smoke With Unprecedentedly High Backscatter Observed by Lidars Above Southern France”. In: *Geophysical Research Letters* 45.3, pp. 1639–1646. DOI: [10.1002/2017GL076763](https://doi.org/10.1002/2017GL076763). eprint: <https://agupubs.onlinelibrary.wiley.com/doi/pdf/10.1002/2017GL076763>. URL: <https://agupubs.onlinelibrary.wiley.com/doi/abs/10.1002/2017GL076763>.
- Khaykin, S. M., S. Godin-Beekmann, P. Keckhut, et al. (2017). “Variability and evolution of the midlatitude stratospheric aerosol budget from 22 years of ground-based lidar and satellite observations”. In: *Atmospheric Chemistry and Physics* 17.3, pp. 1829–1845. DOI: [10.5194/acp-17-1829-2017](https://doi.org/10.5194/acp-17-1829-2017). URL: <https://www.atmos-chem-phys.net/17/1829/2017/>.
- Kumar, V. Siva, P. B. Rao, and M. Krishnaiah (2003). “Lidar measurements of stratosphere-mesosphere thermal structure at a low latitude: Comparison with satellite data and models”. In: *Journal of Geophysical Research: Atmospheres* 108.D11. DOI: [10.1029/2002JD003029](https://doi.org/10.1029/2002JD003029). eprint: <https://agupubs.onlinelibrary.wiley.com/doi/pdf/10.1029/2002JD003029>. URL: <https://agupubs.onlinelibrary.wiley.com/doi/abs/10.1029/2002JD003029>.
- Kyrölä, E. et al. (2010). “Retrieval of atmospheric parameters from GOMOS data”. In: *Atmospheric Chemistry and Physics* 10.23, pp. 11881–11903. DOI: [10.5194/acp-10-11881-2010](https://doi.org/10.5194/acp-10-11881-2010). URL: <https://www.atmos-chem-phys.net/10/11881/2010/>.
- Lastovicka, Jan (2017). “A review of recent progress in trends in the upper atmosphere”. In: *Journal of Atmospheric and Solar-Terrestrial Physics* 163. Long-term changes and trends in the upper atmosphere, pp. 2–13. ISSN: 1364-6826. DOI: <https://doi.org/10.1016/j.jastp.2017.03.009>. URL: <http://www.sciencedirect.com/science/article/pii/S1364682617300044>.
- Leblanc, Thierry and Alain Hauchecorne (1997). “Recent observations of mesospheric temperature inversions”. In: *Journal of Geophysical Research: Atmospheres* 102.D16, pp. 19471–19482. DOI: [10.1029/97JD01445](https://doi.org/10.1029/97JD01445). eprint: <https://doi.org/10.1029/97JD01445>.

- [//agupubs.onlinelibrary.wiley.com/doi/pdf/10.1029/97JD01445](https://agupubs.onlinelibrary.wiley.com/doi/pdf/10.1029/97JD01445). URL: <https://agupubs.onlinelibrary.wiley.com/doi/abs/10.1029/97JD01445>.
- Leblanc, Thierry, I. Stuart McDermid, Philippe Keckhut, et al. (1998). “Temperature climatology of the middle atmosphere from long-term lidar measurements at middle and low latitudes”. In: *Journal of Geophysical Research: Atmospheres* 103.D14, pp. 17191–17204. ISSN: 2156-2202. DOI: [10.1029/98JD01347](https://doi.org/10.1029/98JD01347). URL: <http://dx.doi.org/10.1029/98JD01347>.
- Leblanc, Thierry, Robert J. Sica, et al. (2016). “Proposed standardized definitions for vertical resolution and uncertainty in the NDACC lidar ozone and temperature algorithms – Part 1: Vertical resolution”. In: *Atmospheric Measurement Techniques* 9.8, pp. 4029–4049. DOI: [10.5194/amt-9-4029-2016](https://doi.org/10.5194/amt-9-4029-2016). URL: <https://hal-insu.archives-ouvertes.fr/insu-01306586>.
- Leblanc, Thierry et al. (1998a). “Evaluation of optimization of lidar temperature analysis algorithms using simulated data”. In: *Journal of Geophysical Research: Atmospheres* 103.D6, pp. 6177–6187. DOI: [10.1029/97JD03494](https://doi.org/10.1029/97JD03494). eprint: <https://agupubs.onlinelibrary.wiley.com/doi/pdf/10.1029/97JD03494>. URL: <https://agupubs.onlinelibrary.wiley.com/doi/abs/10.1029/97JD03494>.
- (1998b). “Evaluation of optimization of lidar temperature analysis algorithms using simulated data”. In: *Journal of Geophysical Research: Atmospheres* 103.D6, pp. 6177–6187. DOI: [10.1029/97JD03494](https://doi.org/10.1029/97JD03494). eprint: <https://agupubs.onlinelibrary.wiley.com/doi/pdf/10.1029/97JD03494>. URL: <https://agupubs.onlinelibrary.wiley.com/doi/abs/10.1029/97JD03494>.
- Leblanc, T. et al. (2016). “Proposed standardized definitions for vertical resolution and uncertainty in the NDACC lidar ozone and temperature algorithms - Part 3: Temperature uncertainty budget”. In: *Atmospheric Measurement Techniques* 9, pp. 4079–4101. DOI: [10.5194/amt-9-4079-2016](https://doi.org/10.5194/amt-9-4079-2016).
- Li, Tao et al. (2011). “Middle atmosphere temperature trend and solar cycle revealed by long-term Rayleigh lidar observations”. In: *Journal of Geophysical Research: Atmospheres* 116.D4. DOI: [10.1029/2010JD015275](https://doi.org/10.1029/2010JD015275). eprint: <https://agupubs.onlinelibrary.wiley.com/doi/pdf/10.1029/2010JD015275>. URL: <https://agupubs.onlinelibrary.wiley.com/doi/abs/10.1029/2010JD015275>.
- Licel (2018). *Licel Data Sheet Kernel Description*. URL: <https://http://licel.com/transdat.htm#DNL> (visited on 08/08/2018).

- Livesey, N. J. et al. (2006). “Retrieval algorithms for the EOS Microwave limb sounder (MLS)”. In: *IEEE Transactions on Geoscience and Remote Sensing* 44.5, pp. 1144–1155. ISSN: 0196-2892. DOI: [10.1109/TGRS.2006.872327](https://doi.org/10.1109/TGRS.2006.872327).
- Livesey, N.J. et al. *Version 3.3 and 3.4 Level 2 data quality and description document*. URL: http://mls.jpl.nasa.gov/data/v3_data_quality_document.pdf.
- Lubken, Franz-Josef, Uwe Berger, and Gerd Baumgarten (2018). “On the Anthropogenic Impact on Long-Term Evolution of Noctilucent Clouds”. In: *Geophysical Research Letters* 45.13, pp. 6681–6689. DOI: [10.1029/2018GL077719](https://doi.org/10.1029/2018GL077719). eprint: <https://agupubs.onlinelibrary.wiley.com/doi/pdf/10.1029/2018GL077719>. URL: <https://agupubs.onlinelibrary.wiley.com/doi/abs/10.1029/2018GL077719>.
- Mann, H. B. and D. R. Whitney (1947). “On a Test of Whether one of Two Random Variables is Stochastically Larger than the Other”. In: *Ann. Math. Statist.* 18.1, pp. 50–60. DOI: [10.1214/aoms/1177730491](https://doi.org/10.1214/aoms/1177730491). URL: <https://doi.org/10.1214/aoms/1177730491>.
- Matsuno, Taroh (1971). “A Dynamical Model of the Stratospheric Sudden Warming”. In: *Journal of the Atmospheric Sciences* 28.8, pp. 1479–1494.
- McGee, Thomas J. et al. (1995). “Lidar measurements of stratospheric ozone during the STOIC campaign”. In: *Journal of Geophysical Research: Atmospheres* 100.D5, pp. 9255–9262. DOI: [10.1029/94JD02390](https://doi.org/10.1029/94JD02390). eprint: <https://agupubs.onlinelibrary.wiley.com/doi/pdf/10.1029/94JD02390>. URL: <https://agupubs.onlinelibrary.wiley.com/doi/abs/10.1029/94JD02390>.
- McIntyre, M. E. and T. N. Palmer (1983). “Breaking planetary waves in the stratosphere”. In: *Nature* 305. DOI: [10.1038/305593a0](https://doi.org/10.1038/305593a0). URL: <http://dx.doi.org/10.1038/305593a0>.
- Meek, C. E. et al. (2013). “Eureka, 80° N, SKiYMET meteor radar temperatures compared with Aura MLS values”. In: *Annales Geophysicae* 31.7, pp. 1267–1277. DOI: [10.5194/angeo-31-1267-2013](https://doi.org/10.5194/angeo-31-1267-2013). URL: <https://www.ann-geophys.net/31/1267/2013/>.
- Meriwether, J. W. et al. (1998). “Observed coupling of the mesosphere inversion layer to the thermal tidal structure”. In: *Geophysical Research Letters* 25.9, pp. 1479–1482. DOI: [10.1029/98GL00756](https://doi.org/10.1029/98GL00756). eprint: <https://agupubs.onlinelibrary.wiley.com/doi/pdf/10.1029/98GL00756>. URL: <https://agupubs.onlinelibrary.wiley.com/doi/abs/10.1029/98GL00756>.

- Mertens, Christopher J. et al. (2001). "Retrieval of mesospheric and lower thermospheric kinetic temperature from measurements of CO₂ 15 μ m Earth Limb Emission under non-LTE conditions". In: *Geophysical Research Letters* 28.7, pp. 1391–1394. ISSN: 1944-8007. DOI: [10.1029/2000GL012189](https://doi.org/10.1029/2000GL012189). URL: <http://dx.doi.org/10.1029/2000GL012189>.
- NDACC Lidar. <http://ndacc-lidar.org/>.
- NOAA NASA, USAF (1962). *Comparison US standard atmosphere 1962 - U.S. Standard Atmosphere - Wikipedia*. https://en.wikipedia.org/wiki/U.S._Standard_Atmosphere. (Accessed on 10/08/2018).
- Pascal, Blaise (1664). *Traité de l'équilibre des liqueurs, et de la pesanteur de la masse de l'air. Chapitre I*. Charles Savreux ; Gvillaume Desprez.
- Pasko, V. P. (2006). *Theoretical Modelling of Sprites and Jets*. 3rd ed. Vol. 225. 2. Fullekrug, M., Mareev, E.A., Rycroft, M.J. (eds). Dordrecht: Springer. ISBN: 978-1-4020-4627-8.
- Pautet, P.-D. et al. (2014). "Advanced mesospheric temperature mapper for high-latitude airglow studies". In: *Appl. Opt.* 53.26, pp. 5934–5943. DOI: [10.1364/AO.53.005934](https://doi.org/10.1364/AO.53.005934). URL: <http://ao.osa.org/abstract.cfm?URI=ao-53-26-5934>.
- Pérot, K. et al. (2010). "First climatology of polar mesospheric clouds from GOMOS/ENVISAT stellar occultation instrument". In: *Atmospheric Chemistry and Physics* 10.6, pp. 2723–2735. DOI: [10.5194/acp-10-2723-2010](https://doi.org/10.5194/acp-10-2723-2010). URL: <https://www.atmos-chem-phys.net/10/2723/2010/>.
- Picone, J. M. et al. (2002). "NRLMSISE-00 empirical model of the atmosphere: Statistical comparisons and scientific issues". In: *Journal of Geophysical Research: Space Physics* 107.A12. DOI: [10.1029/2002JA009430](https://doi.org/10.1029/2002JA009430). eprint: <https://agupubs.onlinelibrary.wiley.com/doi/pdf/10.1029/2002JA009430>. URL: <https://agupubs.onlinelibrary.wiley.com/doi/abs/10.1029/2002JA009430>.
- Raju, U. Jaya Prakash et al. (2010). "Nocturnal temperature changes over tropics during CAWSES-III campaign: Comparison with numerical models and satellite data". In: *Journal of Atmospheric and Solar-Terrestrial Physics* 72.16, pp. 1171–1179. ISSN: 1364-6826. DOI: <https://doi.org/10.1016/j.jastp.2010.07.013>. URL: <http://www.sciencedirect.com/science/article/pii/S1364682610002099>.
- Ramaswamy, V. et al. (2001). "Stratospheric temperature trends: Observations and model simulations". In: *Reviews of Geophysics* 39.1, pp. 71–122. DOI: [10.1029/1999RG000065](https://doi.org/10.1029/1999RG000065). eprint: <https://agupubs.onlinelibrary.wiley.com/>

- doi/pdf/10.1029/1999RG000065. URL: <https://agupubs.onlinelibrary.wiley.com/doi/abs/10.1029/1999RG000065>.
- Randel, W. J. (2009). "An update of observed stratospheric temperature trend". In: *J. Geophys. Res.* 114, p. D02107. URL: <https://ci.nii.ac.jp/naid/10029016267/en/>.
- Ratnam, M Venkat et al. (2003). "Recent observations of mesospheric temperature inversions over a tropical station (13.5°N,79.2°E)". In: *Journal of Atmospheric and Solar-Terrestrial Physics* 65.3, pp. 323–334. ISSN: 1364-6826. DOI: [https://doi.org/10.1016/S1364-6826\(02\)00337-1](https://doi.org/10.1016/S1364-6826(02)00337-1). URL: <http://www.sciencedirect.com/science/article/pii/S1364682602003371>.
- Remsberg, E. E. et al. (2008). "Assessment of the quality of the Version 1.07 temperature-versus-pressure profiles of the middle atmosphere from TIMED/SABER". In: *Journal of Geophysical Research: Atmospheres* 113.D17. D17101, n/a–n/a. ISSN: 2156-2202. DOI: [10.1029/2008JD010013](https://doi.org/10.1029/2008JD010013). URL: <http://dx.doi.org/10.1029/2008JD010013>.
- Roble, R. G. and R. E. Dickinson (1989). "How will changes in carbon dioxide and methane modify the mean structure of the mesosphere and thermosphere?" In: *Geophysical Research Letters* 16.12, pp. 1441–1444. DOI: [10.1029/GL016i012p01441](https://doi.org/10.1029/GL016i012p01441). eprint: <https://agupubs.onlinelibrary.wiley.com/doi/pdf/10.1029/GL016i012p01441>. URL: <https://agupubs.onlinelibrary.wiley.com/doi/abs/10.1029/GL016i012p01441>.
- Salby, Murry et al. (2002). "Mesospheric inversions and their relationship to planetary wave structure". In: *Journal of Geophysical Research: Atmospheres* 107.D4. DOI: [10.1029/2001JD000756](https://doi.org/10.1029/2001JD000756). eprint: <https://agupubs.onlinelibrary.wiley.com/doi/pdf/10.1029/2001JD000756>. URL: <https://agupubs.onlinelibrary.wiley.com/doi/abs/10.1029/2001JD000756>.
- Schmidlin, F. J. (1976). "Temperature inversions near 75 km". In: *Geophysical Research Letters* 3.3, pp. 173–176. DOI: [10.1029/GL003i003p00173](https://doi.org/10.1029/GL003i003p00173). eprint: <https://agupubs.onlinelibrary.wiley.com/doi/pdf/10.1029/GL003i003p00173>. URL: <https://agupubs.onlinelibrary.wiley.com/doi/abs/10.1029/GL003i003p00173>.
- Schwartz, M. J. et al. (2008). "Validation of the Aura Microwave Limb Sounder temperature and geopotential height measurements". In: *Journal of Geophysical Research: Atmospheres (1984–2012)* 113.D15. ISSN: 2156-2202. DOI: [10.1029/2007JD008783](https://doi.org/10.1029/2007JD008783). URL: [http:https://doi.org/10.1029/2007JD008783](https://doi.org/10.1029/2007JD008783).

- Shaw, Tiffany A., Judith Perlwitz, and Ori Weiner (2014). “Troposphere-stratosphere coupling: Links to North Atlantic weather and climate, including their representation in CMIP5 models”. In: *Journal of Geophysical Research: Atmospheres* 119.10, pp. 5864–5880. DOI: [10.1002/2013JD021191](https://doi.org/10.1002/2013JD021191). eprint: <https://agupubs.onlinelibrary.wiley.com/doi/pdf/10.1002/2013JD021191>. URL: <https://agupubs.onlinelibrary.wiley.com/doi/abs/10.1002/2013JD021191>.
- Sheese, P. E. et al. (2012). “Assessment of the quality of OSIRIS mesospheric temperatures using satellite and ground-based measurements”. In: *Atmospheric Measurement Techniques* 5.12, pp. 2993–3006. DOI: [10.5194/amt-5-2993-2012](https://doi.org/10.5194/amt-5-2993-2012). URL: <https://www.atmos-meas-tech.net/5/2993/2012/>.
- Shepherd, Marianna G. et al. (2001). “Retrieval and validation of mesospheric temperatures from Wind Imaging Interferometer observations”. In: *Journal of Geophysical Research: Space Physics* 106.A11, pp. 24813–24829. DOI: [10.1029/2000JA000323](https://doi.org/10.1029/2000JA000323). eprint: <https://agupubs.onlinelibrary.wiley.com/doi/pdf/10.1029/2000JA000323>. URL: <https://agupubs.onlinelibrary.wiley.com/doi/abs/10.1029/2000JA000323>.
- Shepherd, Theodore G (2002). “Issues in Stratosphere-troposphere Coupling”. In: *Issues in Stratosphere-troposphere Coupling* 80.4B, pp. 769–792. DOI: [10.2151/jmsj.80.769](https://doi.org/10.2151/jmsj.80.769).
- Sica, R.J. and A. Haefele (2015). “Retrieval of temperature from a multiple-channel Rayleigh-scatter lidar using an optimal estimation method”. In: *Appl. Opt.* 54.8, pp. 1872–1889. DOI: [10.1364/AO.54.001872](https://doi.org/10.1364/AO.54.001872). URL: <http://ao.osa.org/abstract.cfm?URI=ao-54-8-1872>.
- Singh, Upendra N. et al. (1996a). “Stratospheric temperature measurements by two collocated NDSC lidars during UARS validation campaign”. In: *Journal of Geophysical Research: Atmospheres* 101.D6, pp. 10287–10297. ISSN: 2156-2202. DOI: [10.1029/96JD00516](https://doi.org/10.1029/96JD00516). URL: <http://dx.doi.org/10.1029/96JD00516>.
- (1996b). “Stratospheric temperature measurements by two collocated NDSC lidars during UARS validation campaign”. In: *Journal of Geophysical Research: Atmospheres* 101.D6, pp. 10287–10297. DOI: [10.1029/96JD00516](https://doi.org/10.1029/96JD00516). eprint: <https://agupubs.onlinelibrary.wiley.com/doi/pdf/10.1029/96JD00516>. URL: <https://agupubs.onlinelibrary.wiley.com/doi/abs/10.1029/96JD00516>.
- Siva Kumar, V., P. B. Rao, and M. Krishnaiah (2003). “Lidar measurements of stratosphere-mesosphere thermal structure at a low latitude: Comparison with

- satellite data and models". In: *Journal of Geophysical Research: Atmospheres* 108.D11. 4342, n/a–n/a. ISSN: 2156-2202. DOI: [10.1029/2002JD003029](https://doi.org/10.1029/2002JD003029). URL: <http://dx.doi.org/10.1029/2002JD003029>.
- Sivakumar, Venkataraman et al. (2011). "Rayleigh LIDAR and satellite (HALOE, SABER, CHAMP and COSMIC) measurements of stratosphere-mesosphere temperature over a southern sub-tropical site, Reunion (20.8° S; 55.5° E): climatology and comparison study". In: *Annales Geophysicae* 29.4, pp. 649–662. DOI: [10.5194/angeo-29-649-2011](https://doi.org/10.5194/angeo-29-649-2011). URL: <https://hal.archives-ouvertes.fr/hal-00586264>.
- Sivakumar, V. et al. (2011). "Rayleigh LIDAR and satellite (HALOE, SABER, CHAMP and COSMIC) measurements of stratosphere-mesosphere temperature over a southern sub-tropical site, Reunion (20.8° S; 55.5° E): climatology and comparison study". English. In: *Annales Geophysicae* 29.4, p. 649. URL: <https://www.lib.uwo.ca/cgi-bin/ezpauthn.cgi?url=http://search.proquest.com/docview/869915562?accountid=15115>.
- Steinbrecht, W. et al. (2003). "Global distribution of total ozone and lower stratospheric temperature variations". In: *Atmospheric Chemistry and Physics* 3.5, pp. 1421–1438. ISSN: 1680-7316. URL: <https://www.ingentaconnect.com/content/doi/16807316/2003/00000003/00000005/art00011>.
- Taori, A., N. Dashora, et al. (2011). "Simultaneous mesosphere-thermosphere-ionosphere parameter measurements over Gadanki (13.5°N, 79.2°E): First results". In: *Journal of Geophysical Research: Space Physics* 116.A7. A07308, n/a–n/a. ISSN: 2156-2202. DOI: [10.1029/2010JA016154](https://doi.org/10.1029/2010JA016154). URL: <http://dx.doi.org/10.1029/2010JA016154>.
- Taori, A., A. Jayaraman, et al. (2012). "A new method to derive middle atmospheric temperature profiles using a combination of Rayleigh lidar and O₂ airglow temperatures measurements". In: *Annales Geophysicae* 30, pp. 27–32. DOI: [10.5194/angeo-30-27-2012](https://doi.org/10.5194/angeo-30-27-2012).
- Taori, A., V. Kamalakar, et al. (2012). "Simultaneous Rayleigh lidar and airglow measurements of middle atmospheric waves over low latitudes in India". English. In: *Journal of Atmospheric and Solar-Terrestrial Physics* 78-79. Complete, pp. 62–69. DOI: [10.1016/j.jastp.2011.06.012](https://doi.org/10.1016/j.jastp.2011.06.012).
- Teisserenc de Bort, L. (1902). "Variations de la température de l'air libre dans la zone comprise entre 8 km et 13 km d'altitude". In: *Compt. Rend. Seances Acad. Sci. Paris* 134, pp. 987–989. URL: <https://ci.nii.ac.jp/naid/10020067541/en/>.

- Thomas, G.E. and J. Olivero (2001). “Noctilucent clouds as possible indicators of global change in the mesosphere”. In: *Advances in Space Research* 28.7, pp. 937–946. ISSN: 0273-1177. DOI: [https://doi.org/10.1016/S0273-1177\(01\)80021-1](https://doi.org/10.1016/S0273-1177(01)80021-1). URL: <http://www.sciencedirect.com/science/article/pii/S0273117701800211>.
- Triplett, Colin C. et al. (2017). “Role of Wind Filtering and Unbalanced Flow Generation in Middle Atmosphere Gravity Wave Activity at Chatanika Alaska”. In: *Atmosphere* 8.2. ISSN: 2073-4433. DOI: [10.3390/atmos8020027](https://doi.org/10.3390/atmos8020027). URL: <http://www.mdpi.com/2073-4433/8/2/27>.
- Tukey, John W. (1949). “Comparing Individual Means in the Analysis of Variance”. In: *Biometrics* 5.2, pp. 99–114.
- Tukiainen, S. et al. (2011). “Retrieval of ozone profiles from GOMOS limb scattered measurements”. In: *Atmospheric Measurement Techniques* 4.4, pp. 659–667. DOI: [10.5194/amt-4-659-2011](https://doi.org/10.5194/amt-4-659-2011). URL: <https://www.atmos-meas-tech.net/4/659/2011/>.
- Vernier, J. P. et al. (2009). “Tropical stratospheric aerosol layer from CALIPSO lidar observations”. In: *Journal of Geophysical Research: Atmospheres* 114.D4. DOI: [10.1029/2009JD011946](https://doi.org/10.1029/2009JD011946). eprint: <https://agupubs.onlinelibrary.wiley.com/doi/pdf/10.1029/2009JD011946>. URL: <https://agupubs.onlinelibrary.wiley.com/doi/abs/10.1029/2009JD011946>.
- Vincent, Robert A. (2015). “The dynamics of the mesosphere and lower thermosphere: a brief review”. In: *Progress in Earth and Planetary Science* 2.1, p. 4. ISSN: 2197-4284. DOI: [10.1186/s40645-015-0035-8](https://doi.org/10.1186/s40645-015-0035-8). URL: <https://doi.org/10.1186/s40645-015-0035-8>.
- Wallace, J. M. and P. V. Hobbs (1977). *Atmosphere science - an introductory survey*.
- Waters, J. W. et al. (2006). “The Earth observing system microwave limb sounder (EOS MLS) on the aura Satellite”. In: *IEEE Transactions on Geoscience and Remote Sensing* 44.5, pp. 1075–1092. ISSN: 0196-2892. DOI: [10.1109/TGRS.2006.873771](https://doi.org/10.1109/TGRS.2006.873771).
- Weinzierl, Bernadett et al. (2017). “The Saharan Aerosol Long-Range Transport and Aerosol–Cloud-Interaction Experiment: Overview and Selected Highlights”. In: *Bulletin of the American Meteorological Society* 98.7, pp. 1427–1451. DOI: [10.1175/BAMS-D-15-00142.1](https://doi.org/10.1175/BAMS-D-15-00142.1). eprint: <https://doi.org/10.1175/BAMS-D-15-00142.1>. URL: <https://doi.org/10.1175/BAMS-D-15-00142.1>.

- Wild, J. D. et al. (1995). “Comparison of stratospheric temperatures from several lidars, using National Meteorological Center and microwave limb sounder data as transfer references”. In: *Journal of Geophysical Research: Atmospheres* 100.D6, pp. 11105–11111. DOI: [10.1029/95JD00631](https://doi.org/10.1029/95JD00631). eprint: <https://agupubs.onlinelibrary.wiley.com/doi/pdf/10.1029/95JD00631>. URL: <https://agupubs.onlinelibrary.wiley.com/doi/abs/10.1029/95JD00631>.
- Williams, E. R. (2001). “Sprites, elves, and glow discharge tubes”. In: *Physics Today* 54.11, pp. 41–47.
- Wing, R., A. Hauchecorne, P. Keckhut, S. Godin-Beekmann, S. Khaykin, and E. M. McCullough (2018a). “Lidar temperature series in the middle atmosphere as a reference data set – Part 2: Assessment of temperature observations from MLS/Aura and SABER/TIMED satellites”. In: *Atmospheric Measurement Techniques* 11.12, pp. 6703–6717. DOI: [10.5194/amt-11-6703-2018](https://doi.org/10.5194/amt-11-6703-2018). URL: <https://www.atmos-meas-tech.net/11/6703/2018/>.
- (2018b). “Lidar temperature series in the middle atmosphere as a reference data set. Part B: Assessment of temperature observations from MLS/Aura and SABER/TIMED satellites”. In: *Atmospheric Measurement Techniques Discussions* 2018, pp. 1–23. DOI: [10.5194/amt-2018-139](https://doi.org/10.5194/amt-2018-139). URL: <https://www.atmos-meas-tech-discuss.net/amt-2018-139/>.
- Wing, R., A. Hauchecorne, P. Keckhut, S. Godin-Beekmann, S. Khaykin, E. M. McCullough, et al. (2018). “Lidar temperature series in the middle atmosphere as a reference data set – Part 1: Improved retrievals and a 20-year cross-validation of two co-located French lidars”. In: *Atmospheric Measurement Techniques* 11.10, pp. 5531–5547. DOI: [10.5194/amt-11-5531-2018](https://doi.org/10.5194/amt-11-5531-2018). URL: <https://www.atmos-meas-tech.net/11/5531/2018/>.
- Wing, Robin et al. (2018a). “Improved lidar measurements as a reference data set for the assessment of temperatures in the middle atmosphere: A) Systematic approach to lidar temperature retrievals and a 20 year comparison of two co-located French lidars”. In: *Atmospheric Measurement Techniques, Submitted*.
- Wu, D.L. et al. (2003). “Mesospheric temperature from UARS MLS: retrieval and validation”. In: *Journal of Atmospheric and Solar-Terrestrial Physics* 65.2, pp. 245–267. ISSN: 1364-6826. DOI: [https://doi.org/10.1016/S1364-6826\(02\)00293-6](https://doi.org/10.1016/S1364-6826(02)00293-6). URL: <http://www.sciencedirect.com/science/article/pii/S1364682602002936>.

- Wuebbles, DJ, DW Fahey, and KA Hibbard (2016). “The Climate Science Special Report (CSSR) of the Fourth National Climate Assessment (NCA4)”. In: *AGU Fall Meeting Abstracts*.
- Xu, Jiyao et al. (2006). “Comparison between the temperature measurements by TIMED/SABER and lidar in the midlatitude”. In: *Journal of Geophysical Research: Space Physics* 111.A10. A10S09, n/a–n/a. ISSN: 2156-2202. DOI: [10.1029/2005JA011439](https://doi.org/10.1029/2005JA011439). URL: <http://dx.doi.org/10.1029/2005JA011439>.
- Yuan, T. et al. (2010). “A collaborative study on temperature diurnal tide in the midlatitude mesopause region (41N, 105W) with Na lidar and TIMED/SABER observations”. In: *Journal of Atmospheric and Solar-Terrestrial Physics* 72, pp. 541–549. DOI: [10.1016/j.jastp.2010.02.007](https://doi.org/10.1016/j.jastp.2010.02.007).
- Yue, Chuan et al. (2014). “Lidar observations of the middle atmospheric thermal structure over north China and comparisons with TIMED/SABER”. English. In: *Journal of Atmospheric and Solar-Terrestrial Physics* 120.Complete, pp. 80–87. DOI: [10.1016/j.jastp.2014.08.017](https://doi.org/10.1016/j.jastp.2014.08.017).